UNIVERSITY OF CALIFORNIA

Santa Barbara

Engineering Extracellular Strategies for Precise Control of Cellular Cues

A dissertation submitted in partial satisfaction of the requirements for the degree Doctor of Philosophy in Molecular, Cellular, and Developmental Biology

by

Erik Todd Hopkins

Committee in charge:

Professor Maxwell Z. Wilson, Chair

Professor Meghan Morrissey

Professor Ryan Stowers

March 2024

The dissertation of Erik Todd Hopkins is approved.

_____

Meghan Morrissey

_____

Ryan Stowers

_____

Maxwell Z. Wilson, Committee Chair

December 2023

Engineering Extracellular Strategies for Precise Control of Cellular Cues

by

Erik Todd Hopkins

To Grandpa.

Thanks for always believing in me and

showing support at every step along the way.

ACKNOWLEDGEMENTS

The Wilson Lab

I'm sure everyone has a soft spot for the people in their PhD lab, but I genuinely could not have imagined working with a group of scientists as talented, driven, and welcoming as you all. On top of being great people to be around, you pushed me to look at problems in unique ways, offered endless new ideas, and were the best support system I could have asked for.

Alanna Stull, Kristy Le, Jose Nunez, Eric Hao

Working with you all and watching you grow into the well-respected scientists you've already become has truly been the most rewarding experience of my graduate education. I hope you can appreciate the work in this dissertation as equally yours as it is mine.

Bret & Joan Hopkins, Jeff & Cheryl Sell

None of this would be possible without your constant support and belief in me for the past 25 years. Thank you for fostering a sense of curiosity, ambition, and hard work in me. I couldn't be prouder of where I am today, and that all stems from your unwavering love, guidance, and sacrifices.

Lauren Robel

Thank you for always being my biggest supporter and tolerating me through the ups and downs of graduate school. I really don't know how this would have been possible without you by my side.

Markus Merk

Markus, thank you. Thank you for being an amazing colleague and even better friend. Thank you for always showing an interest in my work and encouraging me to think critically about every aspect of my projects. And most importantly, thank you for always letting yourself be convinced to go surfing, regardless of how windy, cold, or rainy it may be.

Michael Costello

Michael, you were the first person I met during this UC Santa Barbara experience so it's only fitting you've grown into one of my closest friends and most supportive colleagues. You've helped me develop countless skills, but most importantly showed me what it means to take pride in my work and have a genuine sense of curiosity.

Robert Piscopio

Rob, thank you for always having my back and helping me address challenges in a level-headed fashion. Working with such a talented scientist, whom I also consider an extremely close friend, has been an incredibly rewarding experience.

Taivan Batjargal

Taivan, thank you for always having an open ear to discuss science and/or life. I could always count on your support and advice through the twists and turns of my projects, and for that I am truly thankful.

VITA OF ERIK TODD HOPKINS
December 2023

EDUCATION

Bachelor of Science in Biology, Kent State University, May 2018

Doctor of Philosophy in Molecular, Cellular, and Developmental Biology, University of California, Santa Barbara, December 2023 (expected)

RESEARCH EXPERIENCE

Undergraduate Researcher. *Kent State University*, 2016-2018

National Science Foundation Undergraduate Fellow. *University of North Carolina at Chapel Hill,* Summer 2017

Graduate Researcher, PhD Candidate. *University of California, Santa Barbara*, 2018-Present

SCIENTIFIC PUBLICATIONS

Hopkins E, Merk M, Nunez J, Hao L, Baxter N, Whitehead I, Le K, Wilson MZ. Bacterially-expressed Synthetic Wnt Supports Tissue-specific Embryonic Stem Cell Differentiations. (*In preparation*).

Hopkins E*, Bailey SJ*, Baxter N, Whitehead I, Read de Alaniz J, Wilson MZ. Dields-Alder Photoclick Patterning of Extracellular Matrix for Spatially-controlled Cell Behaviors, *Advanced Materials*, 2023. DOI: 10.1002/adma.202303453.

Hopkins E*, Valois E*, Stull A, Le K, Pitenis AA, Wilson MZ. An Optogenetic Platform to Dynamically Control the Stiffness of Collagen Hydrogels, *ACS Biomaterials Science and Engineering*, 2020. DOI: 10.1021/acsbiomaterials.oco1488.

Bailey SJ, **Hopkins E**, Rael KD, Hashmi A, Manuel Urueña J, Wilson MZ, Read de Alaniz J. Design, Synthesis, and Application of a Water-soluble Photocage for Aqueous Cyclopentadiene-based Diels-Alder Photoclick Chemistry in Hydrogels, *Angewandte Chemie,* 2023. DOI: 10.1002/anie.202301157.

Bailey SJ, Stricker F, **Hopkins E**, Wilson MZ, Read de Alaniz, J. Shining Light on Cyclopentadienone-Norbornadiene Diels-Alder Adducts to Enable Photoinduced Click Chemistry with Cyclopentadiene, *ACS Applied Materials and Interfaces*. 2021. DOI: 10.1021/acsami.1c08670.

AWARDS

NSF Materials Innovation Platform (MIP) Fellow, 2020-2021

UC Santa Barbara Chang Fellowship, 2019-2023

NSF Summer Undergraduate Research Experience (SURE), 2017

TEACHING EXPERIENCE

Intro Biology Laboratory, 2018-2020

Principles of Molecular and Cellular Biology for Brain Sciences, 2023

ABSTRACT

Engineering Extracellular Strategies for Precise Control of Cellular Cues

by

Erik Todd Hopkins

Cells are products of their environment; thus they are tasked with continuously sensing and interpreting the myriad of signals around them to make decisions that shape their fate. A central principle in research and therapeutic development is precisely controlling and administering such signals, while also maintaining this unique environment, to study cellular responses or achieve desired cell fates. Traditionally these cues have been studied in a unidimensional fashion, which fails to capture the inherent spatiotemporal complexity that carries additional layers of relevant cellular information. Current approaches for enabling dynamic control over cellular systems often rely on genetic perturbations or creating complex synthetic scaffolds to support cell growth, which ultimately limit their widespread application. Here we utilize a number of bio-orthogonal chemistries and rational protein design to shape the extracellular environment in ways that relay controllable and biologically-relevant signals while simultaneously preserving the natural complexity experienced by cells *in vivo*. This work highlights a cornerstone in molecular tool development by placing an emphasis on strategies that function without the need for prior cellular modifications by working entirely

in the extracellular environment. We hope that the ability to control dynamic processes in unmodified cell types, coupled with their approachable nature, will promote the widespread adaptation of these technologies and offer promising routes for advancing therapeutic development.

TABLE OF CONTENTS

CHAPTER 1: Introduction

Elements of the surrounding cellular environment provide a constant stream of information that instructs cells of their future decisions and fate. Thus, cells are tasked with continuously integrating and appropriately responding to these ever-changing signals to maintain homeostasis, undergo differentiation, or take actions like migration or division. We can consider cells products of their environments, or more specifically products of the biochemical and mechanical signals that make up their extracellular environment. Therefore, specific cellular fates can be achieved by manipulating extracellular cues.

In developing and fully developed organisms these signals take the form of soluble ligands that engage receptors on the cell surface or structural protein matrices that transmit mechanical information. Moreover, the dynamic and spatially-constrained nature of these signals carries additional layers of cell-relevant information. For example, gradients of the Wnt morphogen orchestrate body axis patterning across metazoan lineages[1] and instruct the differentiation of intestinal stem cells as they migrate out of intestinal crypts[2]. Likewise, dynamic stiffening of the extracellular matrix (ECM) promotes a malignant transformation of epithelial cells[3] while ECM remodeling is thought to regulate embryogenesis in a stiffness-based fashion[4].

Understanding how such signals shape cellular outcomes requires methods that enable precise control over the signal of interest. Historically, these signals have been studied in a unidimensional fashion, thus not fully recapitulating their natural complexity. Molecular engineering has spurred the development of a growing number of genetic, chemical, and material approaches to precisely administer various biochemical and mechanical signals to cells and tissues.

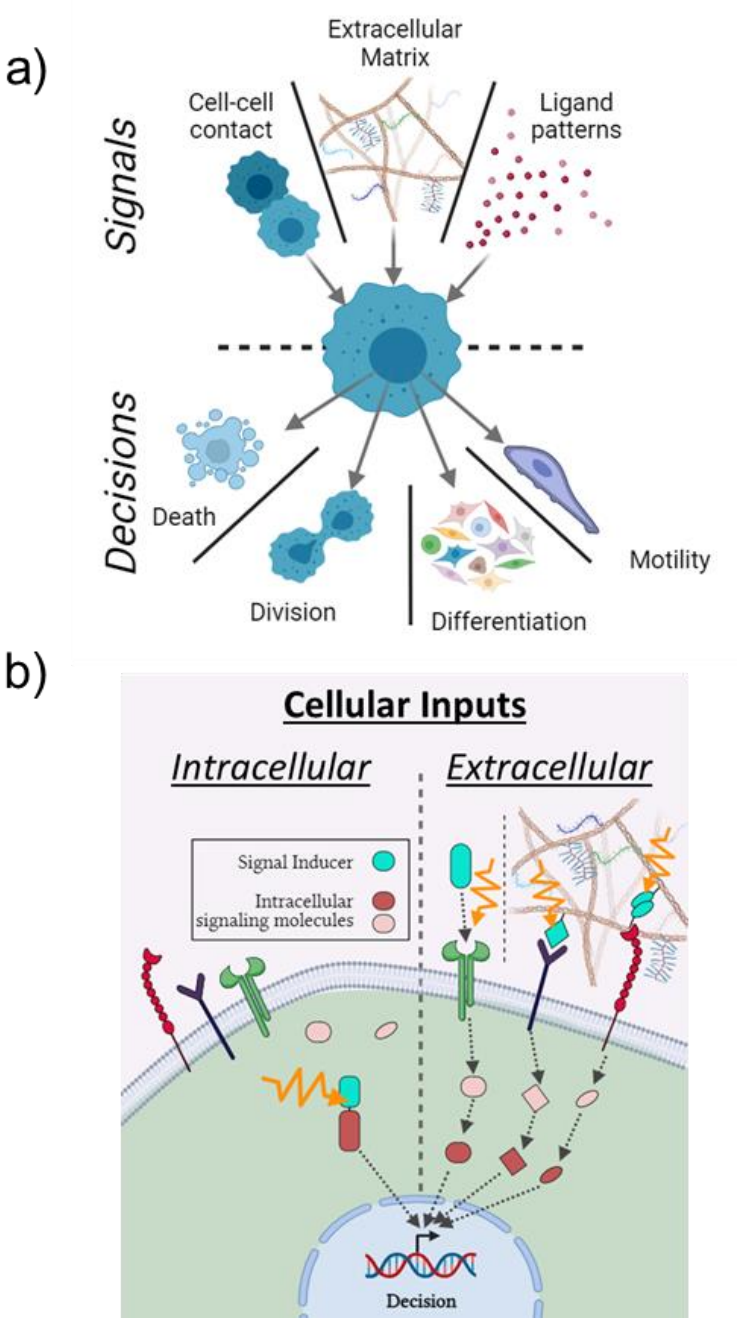

Figure 1.1 a) Cells integrate numerous biochemical and mechanical signals to inform future decisions. b) Schematic depicting intracellular vs. extracellular control of cellular inputs. Intracellular mechanisms of control often bypass receptors and intracellular signaling proteins. Inputs controlled from the extracellular region rely on host cell infrastructure to relay signals.

Genetic-based approaches often rely on modifying intracellular signaling molecules such that their activity can be toggled with an orthogonal input, essentially "tricking" the cell into perceiving the relevant cue. Meanwhile, mechanical approaches typically utilize reactive handles within synthetic hydrogel networks to create environments with desired biochemical and material properties or static modification of natural hydrogels with crosslinking agents. Indeed, these technologies have been essential to uncover the role of tightly regulated processes in gastrulation, differentiation, and disease progression, however genetic modification limits clinical potential and only permits control over cells expressing the modification while synthetic hydrogel networks fail to recapitulate the rich biochemical properties of naturally-derived ECM.

This thesis, through three distinct projects, explores the design and engineering of strategies that enable precise control over biochemical and mechanical cellular signals. Importantly, these novel strategies work entirely in the extracellular space and utilize components that exist naturally in the extracellular environment. Therefore, they can trivially be applied to primary and genetically-unmodified cell types to achieve spatiotemporal control over signal input. In Chapter 2, an optogenetic-inspired approach for constructing mechanically dynamic collagen hydrogels is established. This light-responsive ECM undergoes reversible changes in material properties without the need for complex modification of the collagen scaffold. Chapter 3 introduces an approach that uses an ultraviolet-responsive molecule to photo-pattern morphogens on ECM. The devised approach takes advantage of the biotin-streptavidin interaction to provide modularity to the photopatterning and the implications of this technology are demonstrated by creating surfaces that activate the ERK pathway. Chapter 4 address challenges in Wnt ligand bioengineering by introducing a novel

Wnt ligand that can be expressed from bacteria. The new ligand is shown to be effective in tissue-specific stem cell differentiations and its derivates are used to explore how the ligand's biophysical properties influence Wnt signaling and in the design of a light-responsive ligand.

In summary, this dissertation delves into the development of molecular tools and methods that offer precise control over cellular signals, emphasizing the importance of such control from an extracellular perspective. The subsequent chapters detail projects that contribute to this overarching theme, exploring innovative approaches to manipulate biochemical and mechanical signals, ultimately enhancing our ability to engineer cellular behaviors for research and therapeutic applications.

References

1. Niehrs, C. The role of Xenopus developmental biology in unraveling Wnt signalling and antero-posterior axis formation. *Dev Biol* **482**, 1–6 (2022).

2. Mah, A. T., Yan, K. S. & Kuo, C. J. Wnt pathway regulation of intestinal stem cells. *J Physiol* **594**, 4837 (2016).

3. Ondeck, M. G. *et al.* Dynamically stiffened matrix promotes malignant transformation of mammary epithelial cells via collective mechanical signaling. *Proc Natl Acad Sci U S A* **116**, 3502–3507 (2019).

4. Rozario, T. & DeSimone, D. W. The extracellular matrix in development and morphogenesis: a dynamic view. *Dev Biol* **341**, 126–140 (2010).

CHAPTER 2: Mechanically Dynamic Cell Culture Substrates

Note: Figures, methods, and text from this chapter have been previously published in Hopkins & Valois et al (2020).

2.1 - *Introduction*

Conventional hydrogels are passive scaffolds of synthetic or biological polymers largely utilized for their ability to interface with biological surfaces.[1] Their molecular architecture gives rise to macroscale properties, such as stiffness,[2] that determine their biological efficacy. Recently, there has been a growing appreciation for the importance of a surface's mechanical properties in steering the decision-making networks of an enormous range of cells and organisms.[3–6] Thus, the ability to tune the macroscale properties of hydrogels is crucial for their application in tissue engineering, cell culture, pharmaceuticals, diagnostics, and implants.[7]

The combined sensing of mechanical and chemical cues driving cell fate decisions during development and initiating cellular dysfunction in disease necessitates an extracellular environment that can precisely mimic the dynamic cellular boundary conditions that cells experience *in vivo*. Stimuli-responsive hydrogels made from naturally occurring ECM proteins, in which a user-defined input alters the chemical or mechanical functionality of the gel, can provide this ability *in vitro*. Previously, hydrogels have been engineered to stiffen, soften, or release embedded molecules as a result of chemically- or photo- induced restructuring of the polymer network.[8–10] While such materials have unlocked the ability to acutely perturb the mechanical environment of cells, they either lack reversibility or are designed with synthetic polymers that form an amorphous, non-fibrillar, network. Thus, they

fail to recapitulate the time-varying, chemically and structurally complex nature of the extracellular environment (ECM) (**Figure 2.1 a**).[11–13]

The incorporation of photo-switchable proteins, whose binding state can be toggled with light, into synthetic hydrogel networks has resulted in bidirectionally dynamic materials.[14,15] Such hydrogels can cycle between material states in a light-dependent fashion, transmitting mechanical inputs to embedded cells. In a seminal demonstration of hydrogel mechanical functionalization, Hörner et al. used a Michael-type addition to immobilize the phytochrome Cph1 within poly(ethylene glycol) (PEG) hydrogels. The resulting materials reversibly changed their material properties in response to different wavelengths of light (as determined by Cph1 responsiveness) and induced differential expression of mechanoresponsive genes in human mesenchymal stem cells.[14] While such materials allow the study of dynamic mechanical inputs to cells, PEG is biologically inert and requires the addition of cell-recognition motifs to support cell growth.[16] Although the chemical nature of PEG (and other synthetic gel-forming polymers) facilitates such modifications, a widespread movement toward more physiologically relevant culture platforms highlights the need for an easily-disseminatable method to control the mechanical properties of ECM mimetic substrates. Thus, to retain the biochemical and mechanical complexity of natural ECM, we sought to reversibly control the mechanical properties of a natural ECM-forming polymer.

Collagen Type I is a ubiquitous hydrogel-forming protein that plays a key role in shaping ECM mechanics and signaling in vertebrates.[17] Post-translational modifications and a fibrillar structure give rise to intrinsic signaling capabilities essential for proper cell function.[6,18–20] Despite its relevance, collagen's utility is limited by its finite functionalization

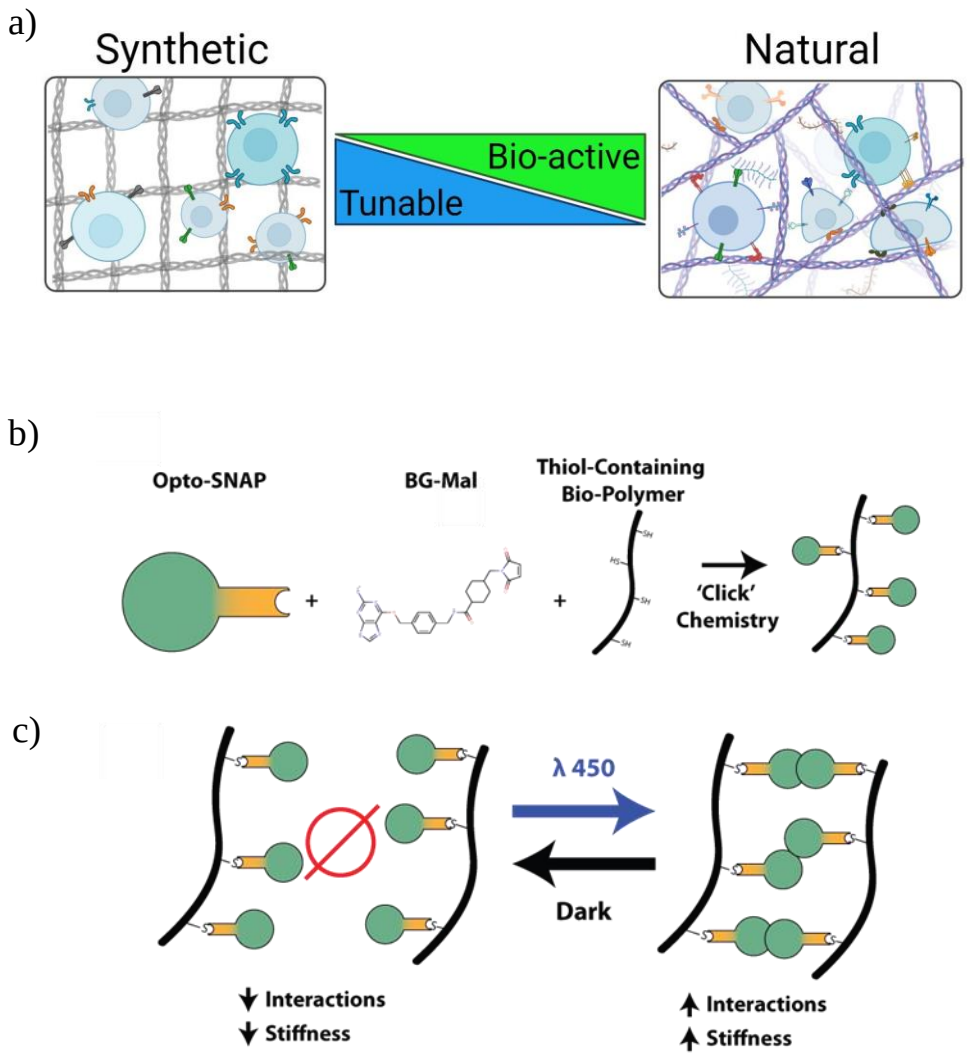

Figure 2.1. a) Graphical depiction of cells on synthetic (*left*) and natural (*right*) hydrogel network. Synthetic hydrogels have limited biochemical activity and rely on modifications to support cell growth. Naturally occurring hydrogels, like collagen, have a fibrilous structure containing several biochemically relevant domains that interface with cells. b) Three-piece functionalization platform consisting of a SNAP-tag fusion protein (Opto-SNAP), BG-Mal, and a cysteine-containing biopolymer (collagen). c) Activation of Optoprotein-SNAP-tag fusion proteins, when attached to polymers with BG-Mal, increases polymer-polymer interactions, thus stiffening the hydrogel.

attainable and commonly modified with crosslinking or mineralization agents to achieve hydrogels of desired stiffnesses,[3,22] however these mechanisms are unidirectional and tend to occupy cell recognition sites that diminish collagen's intrinsic bioactivity.[23]

Here we report a promising platform technology for creating reversible, stimuli-responsive ECM for any thiol containing biopolymer. The modular design consists of three constituent components. i) A translational fusion between a photo-switchable protein and SNAP-tag enzyme (Opto-SNAP),[24] ii) a thiol-containing biopolymer (Rat tail Collagen, Corning), and iii) a targeted heterofunctional SNAP-tag substrate (benzylguanine-maleimide) (**Figure 2.1 b**). We show that benzylguanine-maleimide (BG-Mal) covalently links Opto-SNAP proteins to a collagen hydrogel (OptoGel), offering an alternative to recombinant ECM modification. OptoGels mimic biologically relevant tissue dynamics that have been shown to influence cell fate decisions in development and disease through blue light stimulation.[14,25] The ease with which OptoGels are assembled and their ability to precisely mimic natural ECM may greatly facilitate cellular mechanical studies.

2.2 - *Results*

2.2.1 SNAP-tag Fusion Design

The core component of our OptoGels is a purified "optogenetic" protein that can occupy two self-association states, one with a substantially greater dissociation constant (K_d) than the other, depending on whether it has absorbed the energy from a photon of a particular wavelength of light.[26] To begin we chose to work with the Lov-domain containing protein EL222, a blue light– responsive protein from *Erythrobacter litoralis*.[27] EL222 undergoes a well-documented conformational rearrangement in the presence of blue light, whose switching

efficiency peaks at 450nm light, to expose a high affinity homodimerization interface.[28] We hypothesized that covalently linking EL222 to gelled collagen by creating a SNAP-tag - EL222 fusion protein (EL222-SNAP) would permit light-programmable stiffening caused by the formation of nascent crosslinks resulting from the light-induced decrease in EL222-EL222 K_d, as the EL222 homodimers would act analogously to crosslinks (**Figure 2.1 c**).

From the N- to C- terminus, EL222-SNAP consists of a 6x His tag to aid in purification, mCherry-FP to permit visualization of functionalized collagen hydrogels (OptoGel), a TEV cleavage site followed by EL222, a 6 amino acid GS linker, and the SNAP tag enzyme (**Figure 2.2 a, Supplementary Information Table T2.1**). The TEV cleavage site is intended to allow removal of the fluorescent reporter and aids in construct identification. This construct, EL222-SNAP, was expressed and purified through E. coli bacterial expression, metal affinity chromatography, and size exclusion chromatography. Correct expression was verified via western blotting with anti-His and anti-SNAP-tag antibodies directed against the N- and C-termini, respectively. Colocalization of signal corresponding to anti-His and anti-SNAP-tag at 75 kDa indicated the presence of a full-length construct. Matrix Assisted Laser Desorption Ionization Time of Flight Mass Spectrometry (MALDI-TOF MS) of purified EL222-SNAP produced a m/z peak at 74.4 (**Figure 2.2 e, *black line***). An overnight TEV digestion of EL222-SNAP produced two distinct peaks at 30 and 44.2 (**Figure 2.2 f, g, *black line***), corresponding to the N- and C- terminal products of EL222-SNAP and confirming the successful purification of our synthetic product. We noted the presence of minor degradation products from the full-length product in both western blots and MS (Fig. 2B,C), however these did not appear to influence EL222-SNAP function or subsequent experiments.

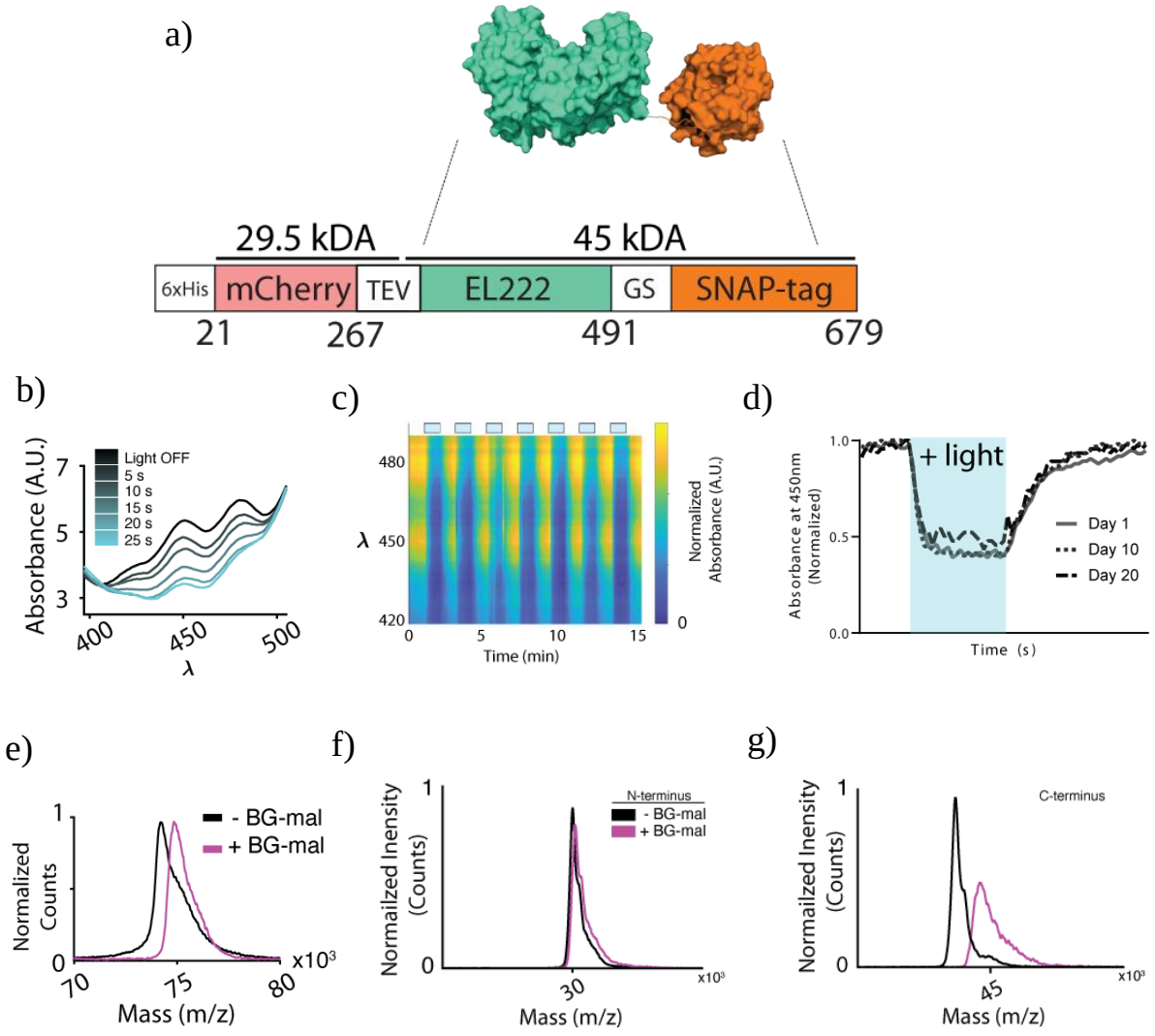

Figure 2.2. a) Schematic of EL222-SNAP protein. EL222-SNAP absorbance at 450nm during b) 25 seconds of blue light illumination, c) 7 duty cycles of illumination, and d) illumination at 1-, 10-, and 20-days post purification. e) EL222-SNAP increases ~650 Da when incubated with BG-Mal. After TEV digest, N-terminal product shows no mass shift f), while C-terminal fragment increases ~650 Da.

2.2.2 EL222-SNAP Functionality

Purified EL222-SNAP must be both light-responsive and efficiently conjugate BG-Mal in order to engineer reversible, light-tunable OptoGels. Thus, after purifying EL222-SNAP we sought to verify that it was fully functional. In the absence of blue light, EL222-SNAP exhibits an absorbance peak at 450 nm, consistent with published reports of EL222.[28] Upon illumination, this peak decreased (**Figure 2.2 b**), indicating that our recombinant EL222-SNAP could indeed photo-actuate, consistent with Cys-FMN adduct formation and decreased K_d.[28] After removing blue light the 450 nm absorbance peak returned, indicating reversibility. Additionally, we tested EL222-SNAP's capacity to be cyclically photo switched and found no fatigue after 7 sequential activations (**Figure 2.2 c**). Finally, measurements of photoswitchability of purified EL222-SNAP over 20 days revealed no degradation in its ability to respond to light activation (**Figure 2.2 c**). Taken together these results demonstrate that the light-responsive functionality of EL222 is retained in the SNAP-tag fusion.

In order for EL222-SNAP dimerization to alter the OptoGel's stiffness it must be mechanically coupled through covalent attachment of the SNAP-tag domain to BG-Mal. To confirm this interaction, we compared MALDI-TOF mass spectrometry of EL222-SNAP with, and without, BG-Mal incubation. As expected, incubation with BG-Mal increased the mass of EL222-SNAP by 650 Da, consistent with the mass of BG-Mal (**Figure 2.2 e**). TEV protease digestion of EL222-SNAP, which cleaves the His-mCherry from EL222-SNAP, confirmed BG-Mal binds at the C-terminal SNAP-tag (**Figure 2.2 f, g**). Together, these results indicate that our purified EL222-SNAP has the functional characteristics required to engineer reversibly photo-switchable biopolymers.

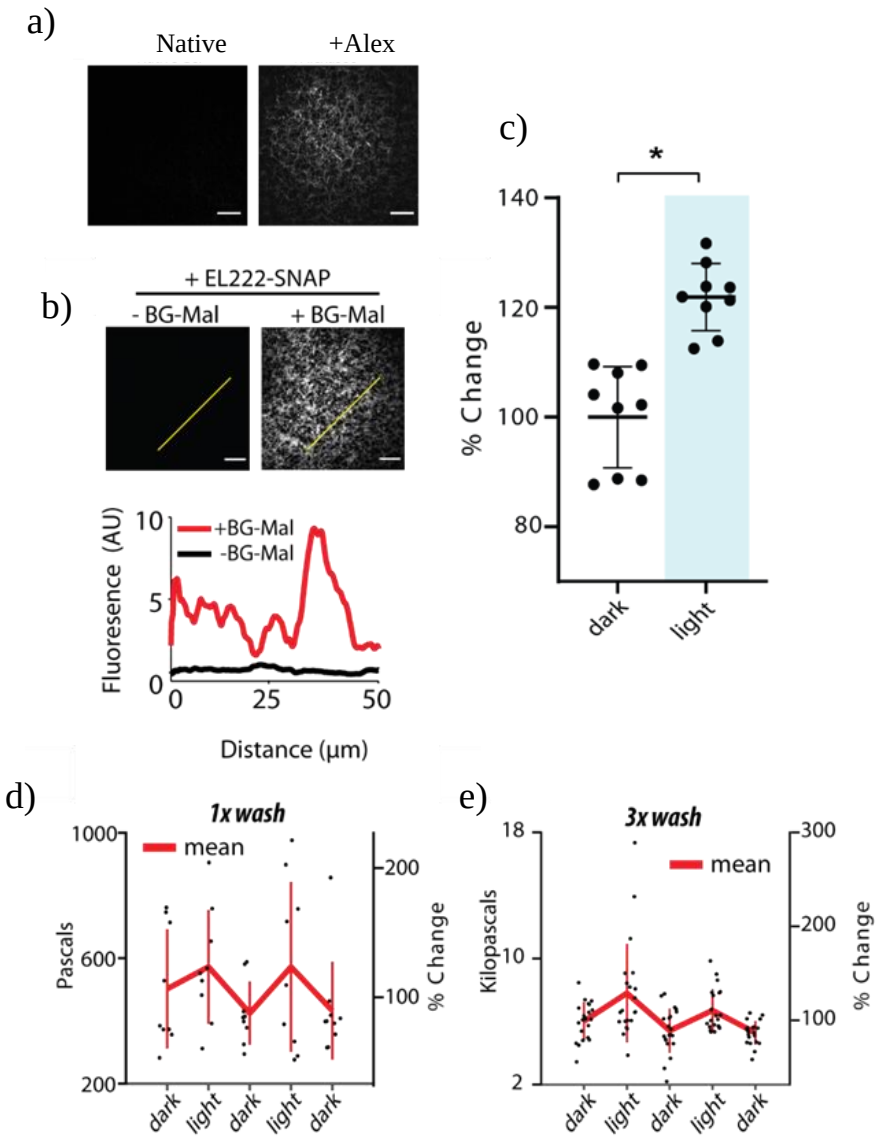

Figure 2.3. a) Naïve (untagged, *left*) and Alexa-555-maleimide tagged (*right*) collagen hydrogels. Fluorescence signal in the pattern of discernable fibrils confirms the presence of reactive thiols within collagen hydrogel. Scale bar = 10 µm. b) (*Top*) 1 mg/mL collagen hydrogel functionalized with EL222-SNAP with (*right*) and without (*left*) a prior BG-Mal incubation. mCherry signal, from EL222-SNAP, is shown. Scale bar = 10 µm. (*Bottom*) Fluorescence intensity across 50 µm trace (yellow line) of above images. c) Percent change of elastic modulus, as determined by IT-AFM, of EL222 OptoGels during activation. * represents $p < 0.05$. d) Elastic moduli of EL222 OptoGel during 2 sequential activations. e) Elastic moduli of EL222 OptoGel made with 3 EL222-SNAP incubations (versus 1) during 2 sequential activations. Absolute averages for 2.3d and 2.3e reported in Supplementary Table T2.2. Percent change is calculated from the mean.

2.2.3 Functionalization of Collagen Hydrogel with Opto-SNAP

After establishing the functionality of EL222-SNAP, we next sought to use this tool to functionalize off-the-shelf collagen hydrogels. Collagen is an ideal substrate to demonstrate this platform due to its ease of handling, ubiquitous use in cell culture and bioengineering,[11,29,30] and high mole ratio of cysteine residues (~17/molecule). This final attribute permits a high degree of functionalization via thiol-maleimide click chemistry between BG-Mal and collagen-residing cysteine residues.

The presence of solvent-accessible cysteine residues in collagen hydrogels was first assessed with Alexa555-maleimide. The strong fluorescent signal seen in Alexa555 modified hydrogels, even after multiple washes, indicated extensive availability of modification sites (**Figure 2.3 a**). By utilizing BG-Mal as a directionally specific linker for SNAP-tag and thiols, a variety of Opto-SNAP fusion proteins can be tethered to the collagen network with equivalent maleimide-thiol click chemistry. We tested different BG-Mal concentrations to determine the most effective approach for attaching Opto-SNAPs. 100μM was the only concentration resulting in a stiffness increase after completing functionalization and activation. Therefore we used 100 μM BG-Mal for all subsequent experiments (**Figure S2.1**). To avoid BG-Mal reacting with surface-exposed thiols on EL222, which could conjugate EL222-SNAP monomers and compromise their function, collagen hydrogels were incubated with BG-Mal prior to the addition of EL222-SNAP, resulting in specific, covalent coupling of EL222-SNAP to collagen (**Figure S2.2**). The resulting hydrogels showed mCherry fluorescence with clearly discernable collagen fibrils (**Figure 2.3 b, *top right***). Hydrogels incubated with EL222-SNAP but lacking BG-Mal, resulted in the absence of fluorescent fibrils (**Figure 2.3 b, *top left***) demonstrating that EL222-SNAP coupling to collagen is BG-Mal dependent.

To establish OptoGels as a useful tool for cell mechanics studies they must support cell growth in a similar manner to commonly used surfaces, such as collagen and glass. We confirmed that HeLa cells plated on EL222 OptoGels maintained a similar viability and metabolism to cells on collagen and glass substrates over a 7-day period, thus confirming that the EL222-SNAP functionalization is non-toxic (**Figure S2.3**).

2.2.4 Light-Dependent Mechanics of OptoGels

As discussed previously, EL222 undergoes a structural rearrangement when activated to expose a high-affinity dimerization site.[28] Notably, the relationship between crosslink density of collagen and resulting stiffness is well documented, and even exploited evolutionarily to yield tissues of varying mechanical properties.[2,31] Thus, we hypothesized that EL222-SNAP dimerization within OptoGels would act as reversible crosslinks, therefore stiffening the OptoGel in the presence of light. To discern the stiffness dynamic range achievable with EL222 OptoGels we subject them to blue light illumination while simultaneously measuring stiffness using IT-AFM. We found a statistically significant 22% increase in elastic modulus of EL222 OptoGels (196 Pa to 239 Pa) (n = 9) (**Figure 2.3 c**). To accurately mimic the mechanically dynamic environment experienced by cells *in vivo*, OptoGels must reversibly soften and stiffen in response to activating light. To test if OptoGels can be reversibly toggled, we subject them to two rounds of sequential activation (10 min OFF, 10 min ON). The elastic moduli of the OptoGel after illumination was roughly 20% higher than that of the preceding dark state, thus confirming that OptoGels can undergo dynamic stiffening (**Figure 2.3 d**). To test if additional washes with purified EL222-SNAP increased the dynamic range we tested the mechanical toggling in a gel that had been washed 2 additional

times in EL222-SNAP for a total of 3 washes. While we found that these 3X OptoGels were an order of magnitude stiffer in their baseline dark state, upon activation they again stiffened to roughly 20% greater than their baseline (**Figure 2.3 e, Supplementary Information Table 2.2**). Interestingly, dark-state stiffnesses decreased with each successive activation in both OptoGels, most likely as a result of gel fatigue.

A well-established relationship between substrate stiffness and pore size has been gleaned from experiments conducted on static hydrogels. Typically, pore size can be tuned by altering polymer concentration or polymerization.[32,33] Therefore, to interrogate the mechanism of stiffening in activated EL222 OptoGels, the pore size of an EL222 OptoGel was measured with confocal microscopy pre- and post-activation. In the basal state (i.e. no illumination), the average pore area was measured to be 1.6 μm^2 (**Figure S2.4**). Despite blue light activation, our visual quantification revealed no change in pore size, however this method is limited to measuring changes greater than the resolution limit of our optical system.

2.3 - *Discussion*

The mechanical and biochemical importance of the ECM is well established and continues to be an area of intense research. Until recently, the inability to dynamically control the mechanical properties of protein-based hydrogels has forced these two parameters to be studied either independently or in a static fashion, thus inadequately recapitulating the dynamics of the extracellular environment.[34] As the most abundant protein in the ECM, collagen is an obvious choice for creating *de novo* ECM mimetic materials. Collagen's hierarchical structure provides many unique opportunities for tuning macroscopic mechanical properties.[11,29] Parameters such as fiber dimensions, polymerization condition, and fibrillar

crosslink density can be manipulated prior to polymerization, yielding hydrogels with variable, but static mechanical properties.[2,31,32] Considering these physical attributes are essential for many cell-scaffold interactions and mechanotransduction.[13,18–20] the field is limited to varying the properties of static gels and extrapolating between conditions to predict how cells would respond to *in vivo*. While this approach has uncovered several relationships between substrate mechanics and cell fate decisions, it fails to capture real time changes that occur during development and disease.[3,4,6,35]

Our solution leverages the combined attributes from light responsive proteins and the SNAP-tag enzyme. The resulting fusion protein has several key advantages for engineering ECM mimetic hydrogels. First, opto-proteins photo-switch within milliseconds of stimuli application,[36] allowing the ability to reversibly toggle material changes within physiologically relevant timeframes. Second, BG-Mal click chemistry makes for facile modification of most proteins via peptidyl thiols. Other commercially available benzylguanine derivates are designed to target carboxyl- or amine- functional groups, thus offering the possibility to engineer heterofunctionalized proteins and non-protein-based ECM components, such as hyaluronic acid. In comparison to classical collagen crosslinking methods such as 1-ethyl-3-(3-dimthyllamino-propyl)carbodiimide (EDC), thiol-maleimide click chemistry avoids compromising nucleophilic amines necessary for robust cell-substrate interactions.[37] While the work presented here demonstrates the effects of homo-dimerization upon illumination, other classes of opto-proteins exist, including homo- and hetero-oligomerizers and dark-inducible protein complexes, offering a suite of options for engineering dynamic stimuli-responsive materials.[38–40]

By conjugating EL222 to Collagen Type 1 we were able to create a collagen hydrogel with programmable mechanical properties. While the first iteration of our OptoGels demonstrated a modest dynamic range (~22%) in comparison to other optoprotein-based dynamic substrates, who stiffen on the order of kilopascals,[14] such stiffness increases have been shown to increase integrin expression and drive invasion of mammary epithelial cells.[25] In future work we plan to increase the dynamic range of OptoGels by engineering Opto-SNAPs with increased oligomerization states (oligomeric vs. dimeric), however the aforementioned studies highlight potential immediate uses for OptoGels. Importantly, EL222 OptoGels underwent two rounds of reversible stiffening, highlighting their use in modeling complex mechanical dynamics. As previously mentioned, the relationship between mesh size and material stiffness has been well documented. Thus, we anticipated mesh network contraction during stimulation. Contrary to our prediction, increased stiffness appeared independent of mesh size. We interpreted this result to mean that EL222-SNAP was forming nascent crosslinks between adjacent collagen fibrils, leading to increased crosslink density within the gel. Previous studies have shown such processes manifest increased stiffness independent of changes in pore size.[37,41,42] Future work may involve a combination of multiple crosslinking methods to first tune OptoGels to a desired baseline stiffness,[3,41] followed by functionalization to achieve dynamic control.

In summary, we describe an approach to create reversibly stiffening thiol-containing, biopolymer hydrogels using SNAP-tag coupling. As a proof of concept, we implemented this platform by coupling EL222-SNAP with Type 1 Collagen. We show that EL222-SNAP covalently binds collagen hydrogels in a BG-Mal dependent fashion and that the resulting hydrogel undergoes reversible increases in stiffness in a light-dependent fashion. Importantly,

this technology combines collagen's intrinsic biological activity with the ability to tune mechanical properties, thus offering a user-regulated ECM-mimetic environment.

OptoGels provide an immediate opportunity to control acute mechanical cellular environments. Furthermore, by combining the existing OptoGel platform with advanced light delivery devices we hope to increase our control over the spatial and temporal dimensions. Additionally, by altering the 'Opto' module of Opto-SNAP to include light inducible release of signaling proteins, we plan to expand the capabilities of OptoGels to include control of chemical cellular environments. Thus, OptoGels may serve as a singular material capable of recapitulating the mechanical and biochemical components of native ECM.

2.4 - *Materials and Methods*

Opto-SNAP synthesis and purification: The EL222-SNAP expression plasmid was synthesized from the pBAD expression vector (Invitrogen), mCherry, peblindv2 (encoding residues 1-225 of EL222), and pSNAP-tag(T7) (NEB) using Gibson Assembly. Plasmids were transformed into *E. coli* TOP10 (Thermo Fisher Scientific) and transformed clones were selected by 100 µg/mL ampicillin. To express EL222-SNAP, an overnight culture was used to inoculate 1 liter of Terrific Broth (TB, IBI Scientific), supplemented with100 µg/mL ampicillin such that the OD_{600} was 0.01. The culture was grown at 37°C until the OD_{600} reached 0.4-0.6 at which point flasks were covered to keep the culture dark and 0.4% (w/v) arabinose was added to induce expression. *All steps after arabinose induction were carried out in the dark or under red light to prevent activation of EL222-SNAP*. After incubation at 25°C for 14-16 hour, bacteria were harvested by centrifugation, washed with 30mL PBS, and shock frozen in liquid nitrogen for future purification.

To purify the EL222-SNAP, frozen pellets underwent 2 freeze/thaw cycles, and were resuspended in lysis buffer (20mM imidazole, 20mM Tris, 150mM NaCl, pH 8.0) supplemented with 0.25 mg/mL lysozyme (Sigma, 6867-1G) and 1% (v/v) Protease Inhibitor Cocktail (Sigma, P8849-5ML). After a 30 minute incubation at room temperature with gentle shaking, the solution was sonicated at 30% power with an ON:OFF cycle of 15 seconds : 45 seconds for a total time of 5 minutes. Cell lysates were clarified via centrifugation at 10,000g for 15 min. Clarified lysate was loaded onto a HiTrap High Performance Ni-NTA column (GE Healthcare) and separated using a BioRad NGC chromatography system (Bio-Rad Laboratories, Hercules CA). After sample loading, the column was washed with 5 column volumes of binding buffer (20 mM imidazole, 20mM Tris and 150mM NaCl pH 8.0) to remove unbound proteins. Proteins of interest were eluted from the column using binding buffer supplemented with imidazole (250 mM imidazole, 20mM Tris and 150mM NaCl pH 8) and quickly dialyzed to remove imidazole (20mM Tris and 150mM NaCl, pH 8.0). EL222-SNAP eluted from the His-Trap was further separated from unwanted proteins using a Superdex 75 10/300 GL size exclusion column. 500 µL of His-Trap elutant in dialysis buffer was loaded and separated using a flow rate of 400 µL/min while collecting 750µL fractions. Protein concentration and purity were determined with ultraviolet absorption (λ = 280 nm, Extinction Coefficient 75540 $M^{-1}cm^{-1}$ prior to aliquoting and freezing at -80°C for future use.

Light responsiveness and TEV digestion of EL222-SNAP: Purified EL222-SNAP was diluted to 0.5 mg/mL and subject to 1-minute blue light OFF-ON cycles (7x). Absorbance spectra from 200 nm to 900 nm was measured at 5 second increments with an IMPLEN NP80

spectrophotometer. Blue light was delivered by a single 450nm LED powered with a 9V battery placed over the sample.

For TEV digestion, EL222-SNAP was diluted to 1 mg/mL and incubated with 1 µL TEV (2 mg/mL)(Sigma) in a 250 µL reaction. The sample was protected from light and digested overnight at room temperature. Cleaved samples were used for further characterization via Mass Spectrometry, incubation with BG-Maleimide (NEB, S9153S), or loaded onto a HiTrap High Performance Ni-NTA column (GE Healthcare) for separation. For samples loaded into the affinity column, both the wash (Buffer A) and elutant (Buffer B) were saved, dialyzed into Buffer C, and examined with western blot analysis using anti-His (SC Biotech, SC-53073) and anti-SNAP (NEB, P9310S) antibodies.

Additional samples, both TEV-treated and -untreated, were incubated with 100 µM BG-Maleimide (NEB, S9153S) overnight at room temperature, and dialyzed into buffer C to remove excess BG-Maleimide. Dialyzed samples were used for characterization with MALDI-TOF Mass Spectrometry.

Optogel preparation: To promote adhesion of collagen to glass surfaces for subsequent mechanical and cellular tests, surfaces were treated with silanol followed by glutaraldehyde. Briefly, 15mm glass cover slips (#1.5) were cleaned in a bath of ethanol for 24 hours and then dried in the oven at 155°C for 1 hour. Clean surfaces were in incubated in excess 2% 3-Aminopropyl)triethoxysilane (Sigma-Aldrich) in ethanol for 1 hours at room temperature will orbital shaking at 30rpm. Surfaces were then rinsed with excess ethanol and heated at 37°C overnight. Silanted surfaces were subsequently treated with 2% glutaraldehyde (Electron Microscopy Sciences, # 16216-10) in PBS for 2hours at room temp. Surfaces were then rinsed

with excess PBS (2X) and deionized water (2X) to remove excess glutaraldehyde and salt and dried using a sterile air stream before being used to support hydrogels.

Collagen hydrogels were synthesized from rat-tail collagen (Corning, 354249) per the manufacturer's suggestion. Briefly, 1 mg/mL hydrogels (70 µL) were prepped from a high-concentration collagen stock (9.4 mg/mL), 1M NaOH, 10x PBS and water. Hydrogel solution was incubated at 37°C for 45 minutes to induce gelation. After gelation, hydrogels to be imaged with Alexa555-maleimide (Thermo) were incubated in 100 nM dye solution for 2 hours at room temperature. Hydrogels were washed 3 times with PBS to remove unbound dye and stored at 4°C until imaging.

Hydrogels to be functionalized to OptoGels were incubated in 100 µM BG-maleimide for 1 hour at room temperature. Unbound BG-Mal was removed with 3x PBS washes. Hydrogels were further incubated in 4.5 mg/mL EL222-SNAP overnight at room temperature and washed the following day. *All opto protein incubations and proceeding steps were done in the dark to prevent aberrant opto-protein activation*. Hydrogels were stored submerged in the dark in PBS at 4°C until experiments.

Cell culture and viability: HeLa cells were stored at 37°C and 5% CO in T25 flasks in Dulbecco's Modified Eagle Medium (DMEM) containing 10% fetal bovine serum and 1% antibiotic (25units/mL penicillin, 25µg/mL streptomycin)(Invitrogen). For alamarBlue and Live/Dead assays, 96-well glass bottom dishes (Cellvis, Mountain View, CA) were salinated as previously described and 50µL collagen hydrogels were cast in the bottom of the wells and functionalized with EL222-SNAP. Cells were plated at a density of 10,000 cells/well in and monitored over 7 days. Metabolic activity was visualized using media supplemented with 10%

alamarBlue solution following manufacturers protocol. 100uL samples of media were taken after a 1 hour incubation at 37°C and fluorescence signal (Ex/Em 560nm/590nm) was read with a plate reader (Biotek). After incubation in alamarBlue-supplemented media, cells were washed with PBS, DMEM, and replenished with fresh media.

Live versus dead cells were quantified using a LIVE/DEAD Viability/Cytotoxicity Kit (Thermo). Cells were washed once with PBS and incubated in 2µM Calcein-AM and 4 µM ethidium homodimer-1 for 45 minutes at 37°C prior to imaging. Images were captured on a Nikon Super Resolution Spinning Disk Confocal microscope and live/dead cells were identified by custom FIJI macros or by hand, depending on cell density.

Pore size determination: EL222 OptoGels were visualized with a spinning disk super resolution confocal microscope (Nikon) with a 60X water-immersion lens and 1.5X multiplier. Gels were activated with 1 second pulses of 100% 447 nm laser every 5 seconds for 10 minutes. mCherry on EL222-SNAP was utilized to visualize the microarchitecture of OptoGels. The hydrogel was visualized as 5 µM Z-stacks with slices every 0.3 µM (18 slices in total). Slices were taken with the following settings: 100% 561 nm laser, 100 ms exposure, sum of 8 images. Images used for pore size determination were constructed from 3 adjacent slices combined as average intensity projections. 4 different 40 µM x 40 µM areas, before and after activation, were analyzed in FIJI using elliptical ROIs to identify pores. Images were randomized, to prevent biased between pre- and post- activation and subject to analysis by three individuals.

IT-AFM: Images and force measurements were conducted on a MFP-3D Bio (Asylum Research, Santa Barbara, CA). SICON-TL-SiO_2-A silicon tips with a 5µm radius probe

(APPNano, Mountain View, CA) were used in all experiments. Gels were cast onto 10mm mica discs (TedPella, Inc) glued to standard microscope slides. All experiments were conducted within 24 hours of casting. Samples are loaded into the AFM scanning stage and subsequently submerged in PBS. Submerged samples were allowed to equilibrate in the instrument for 30min. Prior to force measurements, the cantilever spring constant was experimentally determined by the thermal tune method usually ranging between 0.5 to 1 N/m. Deflection sensitivity was calculated using a glass slide as an indefinitely stiff calibrant material. Force spectroscopy measurements were conducted over the maximum piezo travel length at 2 µm/s load/unload rate with a maximal loading force of 20 nN. Stiffness and values were calculated by Asylum Research's Elastic Analysis Tool by fitting the lower 10% of the loading curve, a probe radius of 5000 nm and a Poisson ratio of 0.5 to the Hertz Model.

MALDI-TOF Mass Spectrometry: EL222-SNAP identity was assessed using MALDI-TOF MS. Purified protein diluted to 1 mg/mL was mixed 1:10 with MALDI-matrix, a saturated solution of Sinapinic acid in 50% Acetonitrile 1% trifluoroacetic acid. The protein solution was then applied to a 96 spot MALDI target plate (Bruker) and air dried for 30 min. Mass spec analysis was conducted using a Microflex LRF MALDI-TOF (Bruker). Sample targets were irradiated using a Nitrogen laser at 337 nm and a pulse length of 3ns with a repetition rate of 20 Hz. Detection occurred in linear mode between 20-80kDa at sampling rate of 1 Gs/s. Protein Calibration Standard 1 (Bruker #206355) was used as an internal calibration.

Sample Illumination: Photoswitching and AFM samples from experiments detailed in main text figures 2 and 3 and supplementary figures 1, 2, 5, and 6 were illuminated at a distance of

4 cm from the sample using a home-built blue LED resulting in a surface power density of approximately 10 mW/cm^2 at 450nm. Light power was measured using a ThorLabs S121C photodiode power sensor with a 500mW max rating.

Statistical Analysis: All scatter plots are presented as mean + Standard Deviation. Student t-tests were performed on all data sets using the MatLab function *ttest2* with significance of $P<0.05$ denoted by *.

2.5 – *Acknowledgements and References*

The authors acknowledge support from the California Nanosystems Institute (CNSI), supported by the University of California, Santa Barbara and the University of California, Office of the President. E.V. and A.A.P. were supported by the MRSEC Program of the National Science Foundation under Award No. DMR 1720256.

1. Peppas, N. A., Hilt, J. Z., Khademhosseini, A. & Langer, R. Hydrogels in Biology and Medicine: From Molecular Principles to Bionanotechnology. *Adv. Mater.* **18**, 1345–1360 (2006).
2. Lin, S., Gu, L., Editor, A. & Zadpoor, A. A. Influence of Crosslink Density and Stiffness on Mechanical Properties of Type I Collagen Gel. *Materials (Basel).* **8**, 551–560 (2015).
3. Caprio, N. Di & Bellas, E. Collagen Stiffness and Architecture Regulate Fibrotic Gene Expression in Engineered Adipose Tissue. *Advacned Biosyst.* **4**, (2020).
4. Ri Seo, B., Chen, X., Ling, L., Hye Song, Y., Shimpi, A. A., Choi, S., Gonzalez, J., Sapudom, J., Wang, K., Andresen Eguiluz, R. C., Gourdon, D., Shenoy, V. B. &

Fischbach, C. Collagen microarchitecture mechanically controls myofibroblast differentiation. *Proc. Natl. Acad. Sci.* (2020). doi:10.1073/pnas.1919394117/-/DCSupplemental

5. Siryaporn, A., Kuchma, S. L., O'toole, G. A. & Gitai, Z. Surface attachment induces Pseudomonas aeruginosa virulence. *Proc. Natl. Acad. Sci.* **111**, 16860–16865 (2014).
6. Kawahara, K., Yoshida, T., Maruno, T., Oki, H., Ohkubo, T., Koide, T. & Kobayashi, Y. Spatiotemporal regulation of PEDF signaling by type I collagen remodeling. *Proc. Natl. Acad. Sci.* (2020). doi:10.1073/PNAS.2004034117
7. Laftah, W. A., Hashim, S. & Ibrahim, A. N. Polymer Hydrogels: A Review. *Polym. Plast. Technol. Eng.* **50**, 1475–1486 (2011).
8. Stowers, R. S., Allen, S. C. & Suggs, L. J. Dynamic phototuning of 3D hydrogel stiffness. *PNAS* **112**, 1953–1958 (2015).
9. Wang, R., Yang, Z., Luo, J., Hsing, I.-M. & Sun, F. B 12-dependent photoresponsive protein hydrogels for controlled stem cell/protein release. *PNAS* **114**, 5912–5917 (2017).
10. Yang, Z., Yang, Y., Wang, M., Wang, T., Francis Fok, H. K., Jiang, B., Xiao, W., Kou, S., Guo, Y., Yan, Y., Deng, X., Zhang, W. & Sun, F. Dynamically Tunable, Macroscopic Molecular Networks Enabled by Cellular Synthesis of 4-Arm Star-like Proteins. *Matter* **2**, 233–249 (2020).
11. Caliari, S. R. & Burdick, J. A. A practical guide to hydrogels for cell culture. *Nature Methods* **13**, 405–414 (2016).
12. Hu, W., Li, Q., Li, B., Ma, K., Zhang, C. & Fu, X. Optogenetics sheds new light on tissue engineering and regenerative medicine. *Biomaterials* **227**, 119546 (2020).

13. Prince, E. & Kumacheva, E. Design and applications of man-made biomimetic fibrillar hydrogels. *Nat. Rev. Mater.* **4**, 99–115 (2019).

14. Hörner, M., Raute, K., Hummel, B., Madl, J., Creusen, G., Thomas, O. S., Christen, E. H., Hotz, N., Gübeli, R. J., Engesser, R., Rebmann, B., Lauer, J., Rolauffs, B., Timmer, J., Schamel, W. W. A., Pruszak, J., Römer, W., Zurbriggen, M. D., Friedrich, C., Walther, A., Minguet, S., Sawarker, R. & Weber, W. Phytochrome-Based Extracellular Matrix with Reversibly Tunable Mechanical Properties. *Adv. Mater.* 1806727 (2019). doi:10.1002/adma.201806727

15. Liu, L., Shadish, J. A., Arakawa, C. K., Shi, K., Davis, J. & DeForest C. A. Cyclic Stiffness Modulation of Cell-Laden Protein-Polymer Hydrogels in Response to User-Specified Stimuli Including Light Dynamic Biomaterials. *Dyn. Biomater.* **2**, 1800240 (2018).

16. Kyburz, K. A. & Anseth, K. S. Synthetic Mimics of the Extracellular Matrix: How Simple is Complex Enough? HHS Public Access Author manuscript. *Ann Biomed Eng* **43**, 489–500 (2015).

17. Yamauchi, M. & Sricholpech, M. Lysine post-translational modifications of collagen. *Essays Biochem.* **52**, 113–133 (2012).

18. Baker, B. M., Trappmann, B., Wang, W. Y., Sakar, M. S., Kim, I. L., Shenoy, V. B., Burkick, J. A. & Chen, C. S. Cell-mediated fibre recruitment drives extracellular matrix mechanosensing in engineered fibrillar microenvironments. *Nat. Mater.* **14**, 1262–1270 (2015).

19. Hynes, R. O. The extracellular matrix: Not just pretty fibrils. *Science* **326**, 1216–1219 (2009).

20. Lou, J., Stowers, R., Nam, S., Xia, Y. & Chaudhuri, O. Stress relaxing hyaluronic acid-collagen hydrogels promote cell spreading, fiber remodeling, and focal adhesion formation in 3D cell culture. *Biomaterials* **154**, 213–222 (2018).

21. Ruggiero, F. & Koch, M. Making recombinant extracellular matrix proteins. *Methods* **45**, 75–85 (2008).

22. Roether Id, J., Bertels, S., Oelschlaeger, C., Bastmeyer, M. & Willenbacher, N. Microstructure, local viscoelasticity and cell culture suitability of 3D hybrid HA/collagen scaffolds. *PLoS One* (2018). doi:10.1371/journal.pone.0207397

23. Grover, C. N., Farndale, R. W., Best, S. M. & Cameron, R. E. The interplay between physical and chemical properties of protein films affects their bioactivity. *J. Biomed. Mater. Res. Part A* **100 A**, n/a-n/a (2012).

24. Jullerat, Gronmeyer, Keppler, Gendreizig, Pick, Vogel, J. Directed Evolution of O 6-Alkylguanine-DNA Alkyltransferase for Efficient Labeling of Fusion Proteins with Small Molecules In Vivo. *Chem. Biol.* **10**, 313–317 (2003).

25. Levental, K. R. Yu, H. Kass, L. Lakins, J. N. Egeblad, M. Erler, J. T. Fong, S. F. T. Csiszar, K. Giaccia, A. Weninger, W. Yamauchi, M. Gasser, D. L. & Weaver, V. M. Matrix Crosslinking Forces Tumor Progression by Enhancing Integrin Signaling. *Cell* **139**, 891–906 (2009).

26. Takakado, A., Nakasone, Y. & Terazima, M. Photoinduced dimerization of a photosensory DNA-binding protein EL222 and its LOV domain †. *Phys. Chem. Chem. Phys* **19**, 24855 (2017).

27. Zoltowski, B. D., Motta-Mena, L. B. & Gardner, K. H. Blue Light-Induced Dimerization of a Bacterial LOV−HTH DNA-Binding Protein. *Biochemistry* **52**, 12

(2013).

28. Nash, A. I., McNulty, R., Shilito, M. E., Swartz, T. E., Bogomolni, R. A., Luecke, H. & Gardner, K. H.. Structural basis of photosensitivity in a bacterial light-oxygen-voltage/helix-turn-helix (LOV-HTH) DNA-binding protein. *Proc. Natl. Acad. Sci.* **108**, 9499–9454 (2011).

29. Meyer, M. Processing of collagen based biomaterials and the resulting materials properties. *Biomed. Eng. Online* **18**, (2019).

30. Marques, C. F., Diogo, G. S., Pina, S., Oliveira, J. M., Silva, T. H. & Reis, R. L. Collagen-based bioinks for hard tissue engineering applications: a comprehensive review. *Journal of Materials Science: Materials in Medicine* **30**, 1–12 (2019).

31. Depalle, B., Qin, Z., Shefelbine, S. J. & Buehler, M. J. Influence of cross-link structure, density and mechanical properties in the mesoscale deformation mechanisms of collagen fibrils. *J. Mech. Behav. Biomed. Mater.* **52**, 1–13 (2015).

32. Yang, Y.-L., Leone, L. M. & Kaufman, L. J. Elastic Moduli of Collagen Gels Can Be Predicted from Two-Dimensional Confocal Microscopy. *Biophysj* **97**, 2051–2060

33. Taufalele, P. V, VanderBurgh, J. A., Muñoz, A., Zanotelli, M. R. & Reinhart-KingID, C. A. Fiber alignment drives changes in architectural and mechanical features in collagen matrices. *PLoS One* (2019). doi:10.1371/journal.pone.0216537

34. Geckil, H., Xu, F., Zhang, X., Moon, S. & Demirci, U. Engineering hydrogels as extracellular matrix mimics. *Nanomedicine* **5**, 469–484 (2010).

35. Zhou, Q., Lyu, S., Bertrand, A. A., Hu, A. C., Chan, C. H., Ren, X., Dewey, M. J., Tiffany, A. S., Harley, B. A. C. & Lee, J. C. Stiffness of Nanoparticulate Mineralized Collagen Scaffolds Triggers Osteogenesis via Mechanotransduction and Canonical

Wnt Signaling. *bioRxiv* (2020). doi:10.1101/2020.03.09.982231

36. Iuliano, J. N., Gil, A. A., Laptenok, S. P., Hall, C. R., Tolentino Collado, J., Lukacs, A., Hag Ahmed, S. A., Abyad, J., Daryee, T., Greetham, G. M., Sazanovich, I. V., Illarionov, B., Bachr, A., Fischer, M., Towrie, M., French, J. B., Meech, S. R. & Tonge, P. J. Variation in LOV Photoreceptor Activation Dynamics Probed by Time-Resolved Infrared Spectroscopy. *Biochemistry* **57**, 620–630 (2018).

37. Roeder, B. A., Kokini, K., Sturgis, J. E., Robinson, J. P. & Voytik-Harbin, S. L. Tensile Mechanical Properties of Three-Dimensional Type I Collagen Extracellular Matrices With Varied Microstructure. *J. Biomech. Eng.* **124**, (2002).

38. Lungu, O. I., Hallett, R. A., Jung Choi, E., Aiken, M. J., Hahn, K. M. & Kuhlman, B. Designing Photoswitchable Peptides Using the AsLOV2 Domain. *Chem. Biol.* **19**, 507–517 (2012).

39. Zhou, X. X., Chung, H. K., Lam, A. J. & Lin, M. Z. Optical control of protein activity by fluorescent protein domains. *Science (80-.).* **338**, 810–814 (2012).

40. Taslimi, A., Vrana, J. D., Chen, D., Borinskaya, S., Mayer, B. J., Kennedy, M. J. & Tucker, C. L. An optimized optogenetic clustering tool for probing protein interaction and function. *Nat. Commun.* (2014). doi:10.1038/ncomms5925

41. Davidenko, N., Schuster, C. F., Bax, D. V., Raynal, N., Farndale, R. W., Best, S. M. & Cameron, R. E. Control of crosslinking for tailoring collagen-based scaffolds stability and mechanics. *Acta Biomater.* **25**, 131–142 (2015).

42. Greenfield, M. A., Hoffman, J. R., Olvera De La Cruz, M. & Stupp, S. I. Tunable Mechanics of Peptide Nanofiber Gels. *Langmuir* **26**, 3641–3647 (2010).

2.6 – *Supplementary Information*

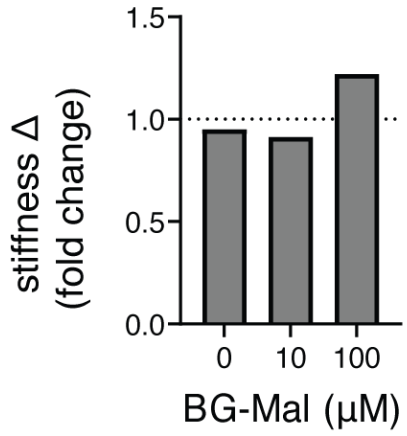

Figure S2.1. Stiffness increases, represented as fold-change from the OFF state, for OptoGels made with increasing concentrations of BG-Mal.

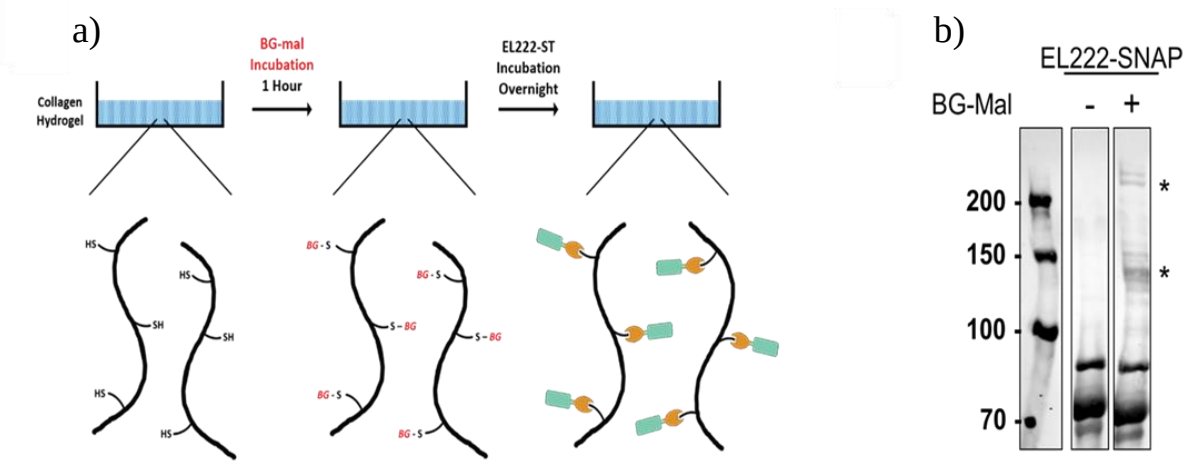

Figure S2.2. a) Schematic showing incubations and subsequent functionalizations involved in OptoGel production. b) EL222-SNAP was incubated with or without BG-Mal for 1 hour at room temperature and examined with western blot analysis and anti-SNAP staining. Incubation with BG-Mal resulted in the formation of EL222-SNAP complexes, as denoted by *. Thus, we chose to functionalize collagen with two separate incubations to avoid the formation of EL222-SNAP complexes within the collagen hydrogel.

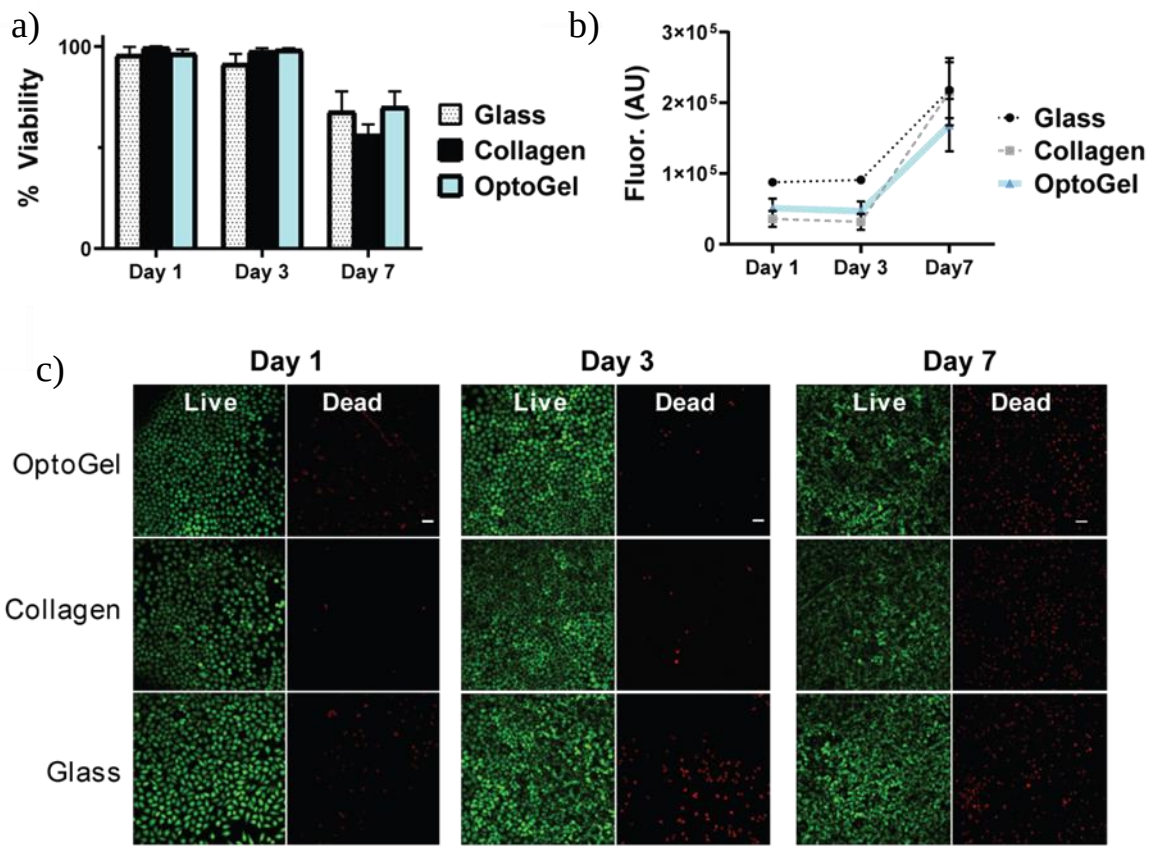

Figure S2.3. a) Percent viability (live/dead) of HeLa cells plated on EL222 OptoGels or collagen or glass controls. OptoGels supported a similar viability to both controls over a 7-day period. b) Metabolic activity, as determined by alamarBlue, of HeLa cells plated on EL222 OptoGels, collagen, or glass. Cells growing on OptoGels demonstrated similar metabolic activity over a 7-day period. c) Representative images of Live/Dead staining used to determine percent viability.

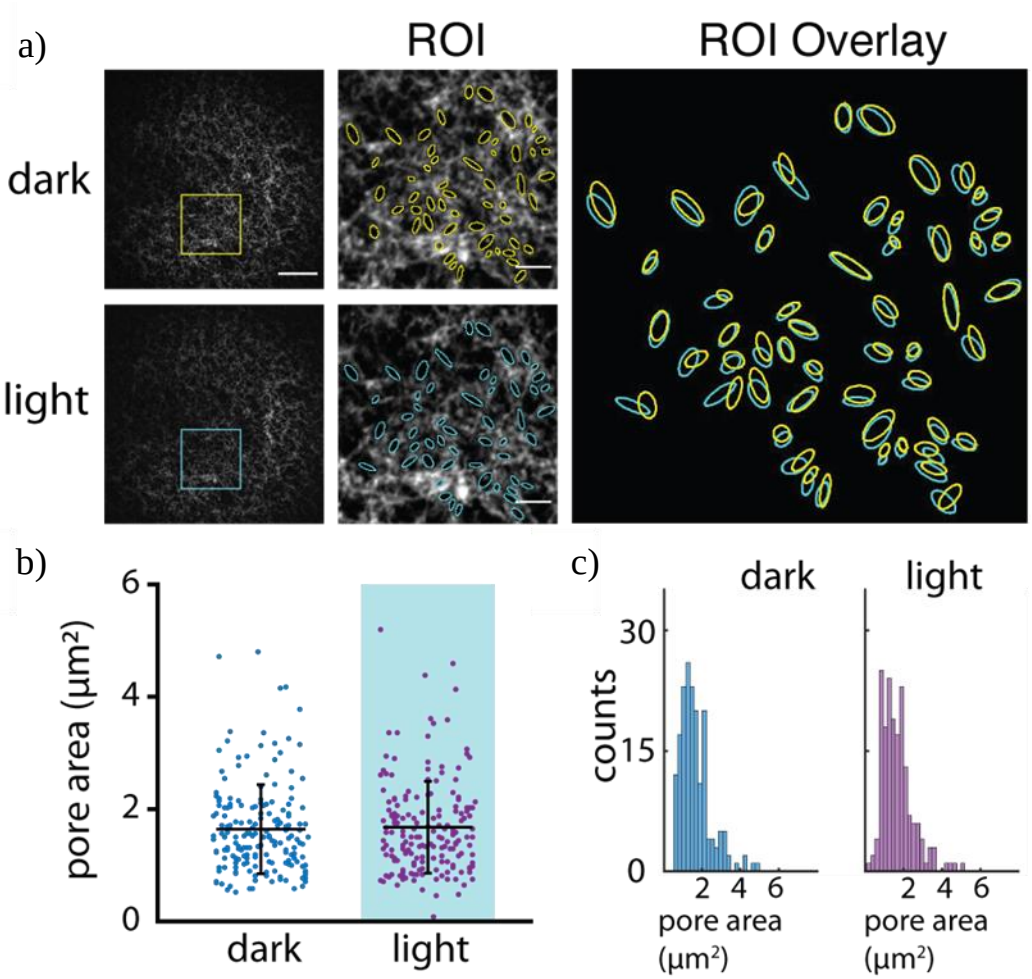

Figure S2.4. a) *Top-left*: Representative image of EL222 OptoGel prior to activation. Scale bar = 20 µm. *Top-right:* zoom of yellow box indicated. Pores used for area calculation are indicated by yellow ovals. Scale bar = 5 µm. *Bottom-Left:* EL222 OptoGel after 10 minutes of simulation. *Bottom-right:* zoom of cyan box indicated. Pores used for area calculation are indicated by cyan ovals. *Right:* Overlay of pre- (*yellow*) and post- (*cyan*) stimulation ROIs used to identify pores. b) Comparison of pore sizes before (*blue*) and after (*purple)* stimulation. c) Distribution of pore sizes before and after stimulation.

Supplementary Table T2.2. Average elastic moduli of EL222 OptoGels in Figures 2.3d (*top row*) and 2.3e (*bottom row*) in pascals.

HHHHHHGMASMTGGQQMGRDMVSKGEEDNMAIIKEFMRFKVHMEGSVNGHEFEIEGEGEGRPY
EGTQTAKLKVTKGGPLPFAWDILSPQFMYGSKAYVKHPADIPDYLKLSFPEGFKWERVMNFEDGG
VVTVTQDSSLQDGEFIYKVKLRGTNFPSDGPVMQKKTMGWEASSERMYPEDGALKGEIKQRLKL
KDGGHYDAEVKTTYKAKKPVQLPGAYNVNIKLDITSHNEDYTIVEQYERAEGRHSTGGMDELYL
YENLYFQGSSMLDMGQDRPIDGSGAPGADDTRVEVQPPAQWVLDLIEASPIASVVSDPRLADNPLI
AINQAFTDLTGYSEEECVGRNCRFLAGSGTEPWLTDKIRQGVREHKPVLVEILNYKKDGTPFRNAV
LVAPIYDDDDELLYFLGSQVEVDDDQPNMGMARRERAAEMLKTLSPRQLEVTTLVASGLRNKEV
AARLGLSEKTVKMHRGLVMEKLNLKTSADLVRIAVEAGIGSGSGSMDKDCEMKRTTLDSPLGKLE
LSGCEQGLHEIKLLGKGTSAADAVEVPAPAAVLGGPEPLMQATAWLNAYFHQPEAIEEFPVPALH
HPVFQQESFTRQVLWKLLKVVKFGEVISYQQLAALAGNPAATAAVKTALSGNPVPILIPCHRVVSS
SGAVGGYEGGLAVKEWLLAHEGHRLGKPGLG

Supplementary Table T2.1. Amino acid sequence of purified EL222-SNAP. Red, blue, and green text represent mCherry, EL222, and SNAP-tag, respectively. Black text, in sequential order, denotes His-tag/T7, TEV cleavage sequence, and GS linker.

	OFF	**ON**	**OFF**	**ON**	**OFF**
1X EL222-SNAP incubation (3C)	502.0	572.22	424.33	572.11	432.3
3X EL222-SNAP incubation (3D)	6025.8	7794.4	5421.4	6706.2	5286.9

CHAPTER 3: Diels-Alder Photoclick Patterning of Extracellular Matrix for Spatially Controlled Cell Behaviors

Note: Figures, methods, and text from this chapter have been previously published in Bailey & Hopkins et al (2023).

3.1 – *Introduction*

Engineered extracellular matrix (ECM) offers an exciting route for both studying and controlling natural cell behaviors through the spatial patterning of local chemical and mechanical environmental cues that instruct cell decisions. In developing organisms, juxtacrine and paracrine signals are read out as informational fields that instruct the spatiotemporal cell fate choices, such as differentiation and migration, which are essential for laying out the body plan[1]. For example, spatial patterning of growth factors instruct cell migration in developing organisms and have been broadly associated with driving metastatic cancer cell migration[2–4]. However, limitations in the ability to arbitrarily pattern spatial cues have made it difficult to both engineer and dissect the role of cellular behaviors in tissue-level coordination.

Various photopatterning technologies have been developed that allow spatially-controlled immobilization of biomolecules within hydrogel matrices[5,6], enabling the preparation of anisotropic microenvironments to control a number of cellular processes including: cell spreading[7–9], proliferation[10], differentiation[11], and morphogenesis[12]. While promising, to date patterning of biochemical cues within hydrogels has largely been demonstrated in synthetic hydrophilic polymer networks (i.e., poly(ethylene glycol)) due to the superior chemical tunability of these systems. However, these inert matrices fail to recapitulate native cellular environments without considerable modification. Alternatively,

naturally-derived protein-based matrices (i.e., collagen, laminin, fibronectin, Matrigel) are commonly used in routine cell culture due to their inherent bioactivity and ease-of-use[13]. Implementing straightforward photopatterning strategies within ECM proteins would, therefore, combine the tunability of synthetic polymers with the natural chemical cues of ECM.

Current photo-controlled bioconjugation technologies often rely on radical-based chemistry (i.e., thiol–ene)[5]; however, radicals are deleterious to the proteins present in the ECM and careful consideration of the radical photoinitiator is needed to avoid cytotoxicity in the presence of cells [14–16]. Recent work has highlighted the need for non-radical propagating photopatterning strategies that can be applied to protein-based hydrogels[10,12]. As an alternative to thiol–ene chemistry, photocage-based strategies offer a radical-free alternative to patterning protein-based hydrogels[5,10,11]; however, these strategies typically involve the photocaging of thiols[7,17] or amines[12,18] which can limit the orthogonality of subsequent photoclick reactions due to the biological prevalence of these functional groups. The ability to photocage non-biologically relevant functional groups, like alkoxyamines,[10,11] endows additional bioorthogonality to photoclick reactions, but requires specific modifications of both the matrix and patterning agent which can be labor-intensive, limiting the adoption of photopatterning by a wide audience. Thus, we sought to overcome these challenges by developing a next-generation photopatterning strategy that avoids radicals, is low cost, provides a non-biologically relevant click handle, and can be accomplished with commercially available reagents.

Our collaborators recently reported the use of cyclopentadienone–norbornadiene (CPD–NBD) as photocaged cyclopentadiene (Cp) which enables rapid, photo-triggered Diels–Alder click chemistry–photoclick–with dienophiles[19]. Previous work demonstrated the utility

of photoclick chemistry for patterning biomolecules in synthetic hydrogels[20]. The photo-uncaging of Cp in this reaction proceeds without the production of free radicals, and Cp has shown promise as a bio-orthogonal click handle[21]. Additionally, the use of maleimide as the dienophile partner enables our strategy to interface with a number of commercially available maleimide-bearing labeling agents and biologically relevant peptides.

Through the use of a thiol-targeted derivative of CPD-NBD we present a novel functionalization platform to photo-pattern ECM proteins (**Figure 3.1 a-c**). We demonstrate the tunability and compatibility of our platform with a wide variety of natural ECM substrates and growth factors, highlighting a mix-and-match approach to spatially define cellular responses. This work underscores the promise of streamlined preparation of patterned surfaces from commercially available materials. By focusing on EGF's role in controlling cell migration, we demonstrate that this platform can be used to spatially engineer cell behaviors on naturally occurring ECM proteins.

3.2 – *Results*

3.2.1 Functionalization of ECM Proteins with CPD-NBD

We previously demonstrated cysteine residues in natural ECM are sufficiently reactive to immobilize high densities of small molecules and proteins[22]. Thus, we designed a maleimide-functionalized CPD-NBD derivative that covalently links to naturally occurring cysteines (Figure 1) within ECM proteins. We reasoned that a photocaged diene handle on a thiol-targeting molecule, that could later be de-protected with light, would enable arbitrary spatial patterning of cell-stimulating ligands. Notably, the dienophiles intended for functionalization can also react with free thiols (cysteine residues) within the ECM protein

networks and result in off-target immobilization. By saturating these sites with CPD-NBD we minimize regions where off-target binding may occur and leave only photo-deprotected Cp for dienophile binding in subsequent patterning steps.

Thus, we synthesized a maleimide-bearing CPD–NBD derivative, 7, in five steps from inexpensive precursors (**Figure 3.1 d**). The maleimide unit enables efficient bioconjugation to cysteines via Micheal additions, whereas reducing the substituent sizes on CPD–NBD adduct 7 from the originally reported pentyl and phenyl groups to methyl groups[19] improves the solubility in phosphate buffered saline with dimethyl sulfoxide (DMSO) as a co-solvent. Improving aqueous solubility allowed us to directly add CPD-NBD to polymer solutions of Collagen Type 1, fibronectin, laminin and Matrigel without matrix precipitation. Full details of CPD–NBD synthesis and ECM protein preparation protocols can be found in the Supporting Information.

3.2.2 Tunable Fluorescent Dye Patterning

We first sought to validate the use of our protein-conjugated CPD–NBD moieties to pattern maleimide bearing species within ECM proteins. Fluorescent dyes are commonly employed as labeling agents in several biological applications and can be purchased with a large range of excitation wavelengths (350–900 nm) and functionalities, including maleimide reactive handles. Thus, we chose to test the tunability of patterning in both concentration of de-protected groups and spatial resolution of CPD–NBD uncaging with a maleimide-bearing Alexa Fluor 555 dye (Alexa-mal). We selected four common cell culture matrices to demonstrate the ability of CPD–NBD to immobilize Alexa-mal in UV-irradiated areas: fibronectin, laminin, collagen, and Matrigel. These proteins represent a sizable fraction of ECM proteins used in tissue culture and tissue engineering[23]. Following masked irradiation of

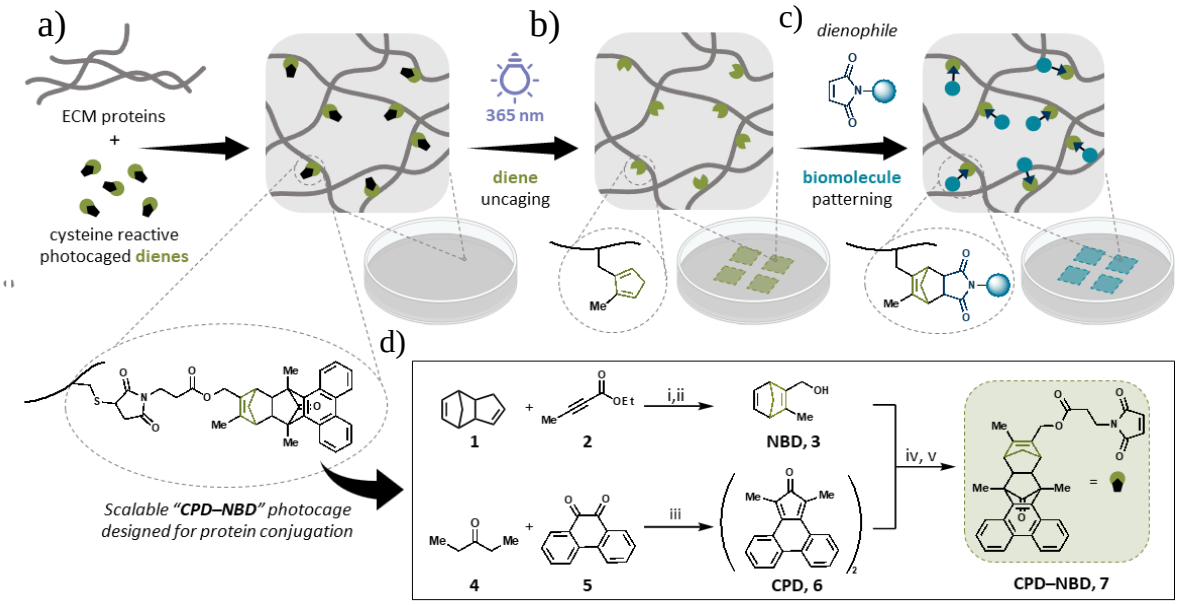

Figure 3.1. Graphic depiction of CPD–NBD patterning platform involving a) ECM protein functionalization with cysteine-reactive CPD–NBD units. This step simultaneously serves to saturate free thiols (cysteines) within the ECM matrix to prevent off-target immobilization in subsequent dienophile incubations. b) UV patterning to uncage reactive diene units (green) and c) subsequent Diels–Alder-based patterning of maleimide functionalized biomolecules. d) Synthesis of cysteine reactive CPD–NBD adduct (**7**) for protein functionalization. Conditions: i) hydroquinone, 200 °C, pressure vessel, 4 h, 56%, ii) DIBAL, THF, 0 °C, 30 min, 71%, iii) 1. K_2CO_3, MeOH, rt, 16 h, 2. MsCl, DMAP, 0 °C – rt, 16 h, 64%, iv) toluene, 100 °C, 24 h, 53% v) **9**, EDC, DMAP, DCM, rt, 1 h, 66%.

CPD–NBD functionalized surfaces (20 μM), gels were incubated in Alexa-mal solutions before thorough rinsing and imaging. High resolution patterns were readily achieved in all four substrates within 5 minutes irradiation time (LED, 365 nm, 6 mW/cm^2), and maximal patterning intensities were obtained around 10 minutes irradiation (**Figure S3.1 a,b**).

To further explore the concentration tunability and spatial resolution of our platform we used digital micromirror devices (DMDs) to create micron-scale patterns on CPD–NBD functionalized surfaces. Illuminating surfaces with a 10-intensity-level graded pattern (10 min illumination, 10X objective) demonstrated that Alexa-mal immobilization (**Figure 3.2 a,b**) has a broad dynamic range that linearly scales with illumination intensity. We noted that laminin displayed the greatest range of Alexa-mal immobilization across illumination intensities, followed by Matrigel and collagen. In contrast to the well-resolved patterns in all matrices following masked flood illumination (**Figure S3.1 a,b**), some variation in resolution was observed across images in DMD-generated patterns. This is likely an artifact of the DMD focal plane being affected by variations in surface thickness. We noted that collagen and fibronectin showed much greater spatial heterogeneity of patterning than laminin and Matrigel, likely reflecting deposition heterogeneity induced by processing the proteins in the presence of DMSO to solubilize CPD-NBD. We anticipate our recently reported water soluble CPD-NBD derivative will circumvent these challenges[20]. Nonetheless, we used the DMDs to highlight the spatial precision of CPD-NBD photo-uncaging by patterning complex shapes (cartoon shark and UCSB logo) on Matrigel surfaces (**Figure 3.2c**). The resulting Alexa-mal immobilization closely matches the corresponding UV pattern and demonstrates our ability to arbitrarily pattern on the micron scale. Furthermore, we highlighted a 250 μm region of each pattern containing intricate detail and plotted the fluorescence profile across the image (**Figure 3.2d**).

Fine details, on the order of 10-20 microns, are clearly resolved thus demonstrating the high granularity that can be achieved and suggesting that CPD-NBD photopatterning can be applied on the single-cell level.

The efficiency of protein functionalization was assessed by comparing Alexa-mal immobilization in CPD-NBD functionalized surfaces to that of surfaces treated with Alexa-mal only (no CPD-NBD functionalization). Both molecules (Alexa-mal and CPD-NBD) bind the ECM protein network at cysteine residues therefore we reasoned the Alexa-mal signal in non-CPD-NBD-functionalized surfaces represents the upper limit of immobilization possible with the patterning platform. Alexa-mal intensity in irradiated areas closely matches that of non-CPD-NBD functionalized surfaces for 3 of the 4 materials (collagen, fibronectin, Matrigel), confirming complete photo-uncaging of CPD-NBD and efficient Cp-maleimide cycloaddition when linked to a protein network (**Figure S3.1 c**). We suspect that Laminin, did not reach its full deprotection at the tested illumination duration because of its greater number of cysteines (>6% of the residues as opposed to other ECM proteins with 1-3%). Overall, all ECM protein networks were significantly functionalized in a light-responsive manner, demonstrating the broad applicability of this platform.

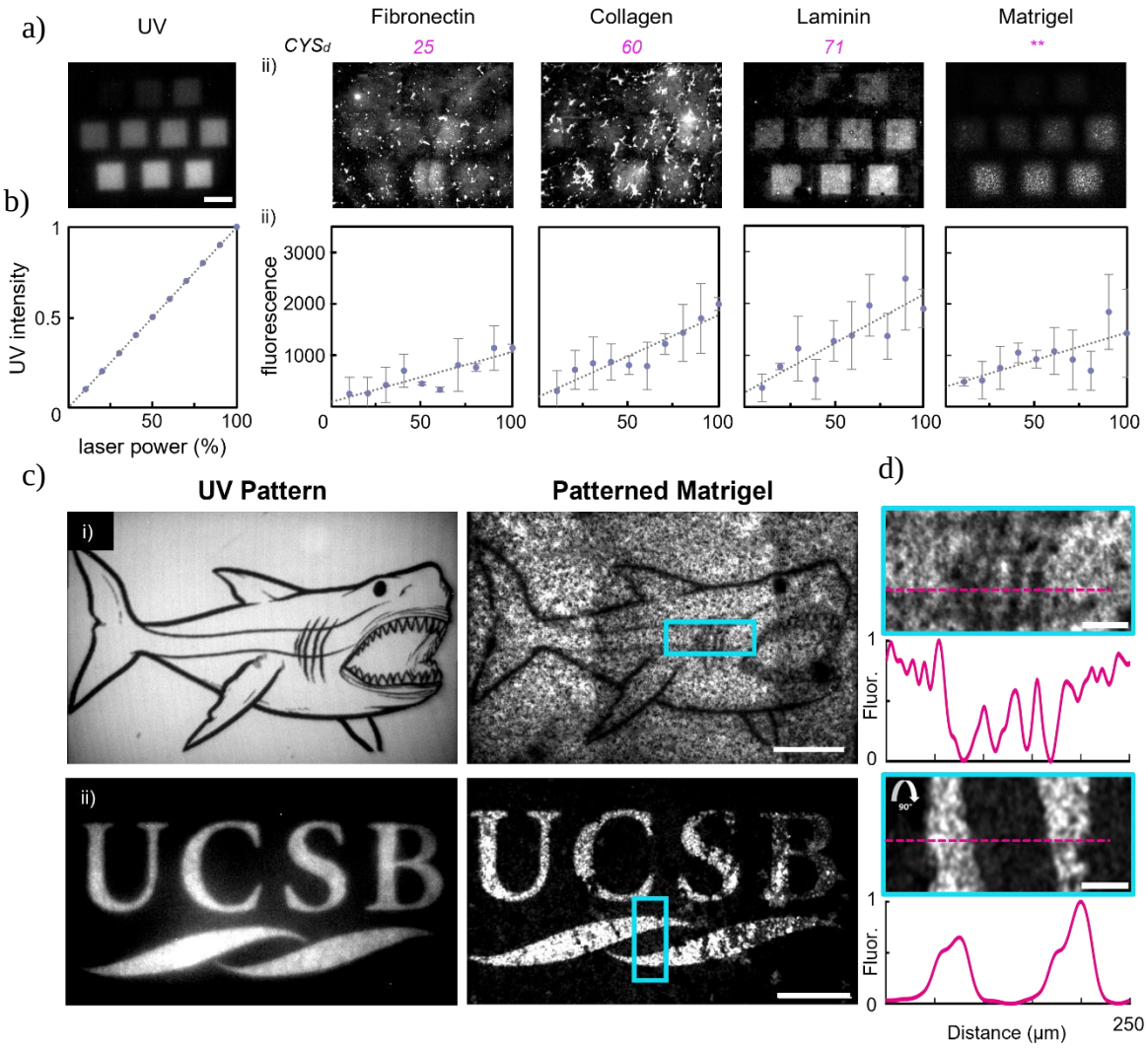

Figure 3.2. a) *i*) DMD-generated UV pattern with increasing intensities and *ii*) representative images of immobilized Alexa-mal following irradiation in each respective material. Data presented as mean +/- standard deviation. n=4. CYS_d represents the estimated density of cysteines within the material as a product of polymer concentration and cysteine content of a respective monomer. **Matrigel is reported as a heterogenous protein solution with a variable composition, thus we did not calculate CYS_d for Matrigel. See CYS_d Determination table in SI Section 4 for further values. Scale bar = 200 μm. b) *i*) Plot of irradiation intensity corresponding to each square of the DMD-generated UV pattern and *ii*) resulting fluorescent intensities represented as difference compared to background (non-irradiated regions). c) Matrigel surfaces patterned with a cartoon shark (*i*) and the UCSB logo (*ii*). Left images represent the DMD-generated UV pattern and right images show resulting Alexa-mal immobilization on Matrigel. Scale bars = 250 μm. d) Magnified region from corresponding Matrigel pattern (cyan outline) and 250 μm fluorescence profile (pink). Plots represent min/max normalized fluorescence intensity across profile line. Scale bars = 50 μm.

3.2.3 Designing a "Mix-and-Match" Patterning Platform with Biotinylated Species

The high-affinity and high-specificity interaction between biotin and streptavidin is routinely used for molecular engineering[24]. We envisioned that CPD-NBD photopatterning could interchangeably immobilize biotinylated species by using a maleimide-streptavidin linker as the Cp-reactive dienophile (**Figure 3.3 a**). Numerous biotinylated growth factors are available commercially or can be directly functionalized with *N*-hydroxysuccinimidyl (NHS)-activated biotin to create a "mix-and-match" platform. To incorporate pattering of biotinylated species we adopted a two-step incubation after irradiation. First ECM networks are incubated in maleimide-streptavidin and washed. Second, they are conjugated with biotinylated effector molecules. To verify this protocol, we patterned a 500 μm diamond onto CPD-NBD functionalized fibronectin and carried out the two-step incubation with biotin-fluorescein, resulting in immobilized biotin-fluorescein within the pattern (**Figure 3.3 b**). We next applied the 10-intensity-level graded pattern to functionalized Matrigel and incubated with biotinylated-BMP4. BMP4 immunofluorescence confirmed morphogen immobilization in an illumination-intensity-dependent fashion with resolution similar to that of Alexa-mal patterning (**Figure 3.3 c**). These experiments confirm the "mix-and-match" modularity of our functionalization platform, demonstrating the ease with which various substrates and ligands can be used for patterning.

3.2.4 Programming Cell Responses with Functionalized Substrates

In our final experiments we chose to assess whether CPD-NBD localized ligands could be used to direct cell behaviors in a spatially confined manner. Thus, we focused on the role of EGF in controlling signaling and cellular motility as a test case. We first determined a

concentration of CPD-NBD that would not interfere with cell viability by monitoring metabolism on non-irradiated ECM proteins treated with up to 100 μM CPD-NBD. Metabolic activity and morphology were unaffected on surfaces prepared with up to 10 μM CPD-NBD for three common cell lines (HEK, HeLa, 3T3), whereas surfaces functionalized with 100 μM CPD-NBD slightly decreased metabolic activity for all cell lines and interfered with cell adhesion and spreading (**Figure S3.2**). Therefore, we chose to functionalize ECM proteins with 10-50 μM CPD-NBD for cell studies. We were also curious how sensitive cell types, such as human embryonic stem cells (hESCs), would respond to CPD-NBD-functionalized surfaces. Laminin functionalized with 10 μM CPD-NBD supported the growth and mesodermal differentiation of embryonic stem cells (**Figure S3.3**), thus confirming that CPD-NBD is compatible with a variety of cell types.

To determine if CPD-NBD photopatterning can be used to direct cell decisions we incorporated biotin-EGF into our mix-and-match approach to yield EGF-functionalized fibronectin. EGF signals through the MAPK/ERK pathway to promote growth, proliferation, and survival[25]; thus we reasoned that controlling ERK activity through patterned EGF could result in the ability to dictate a number of important cell behaviors. We grew HEK cells on EGF-patterned surfaces and immunostained for phosphorylated ERK (pERK) the following day after briefly (1 hour) serum-starving the cells[26]. Cells in irradiated regions of both photomask- and DMD-patterned surfaces had increased levels of pERK compared to their non-irradiated surroundings (**Figure 3.3 d, e**). This confirmed that our CPD-NBD photopatterning platform successfully enables user-defined cellular signal transduction.

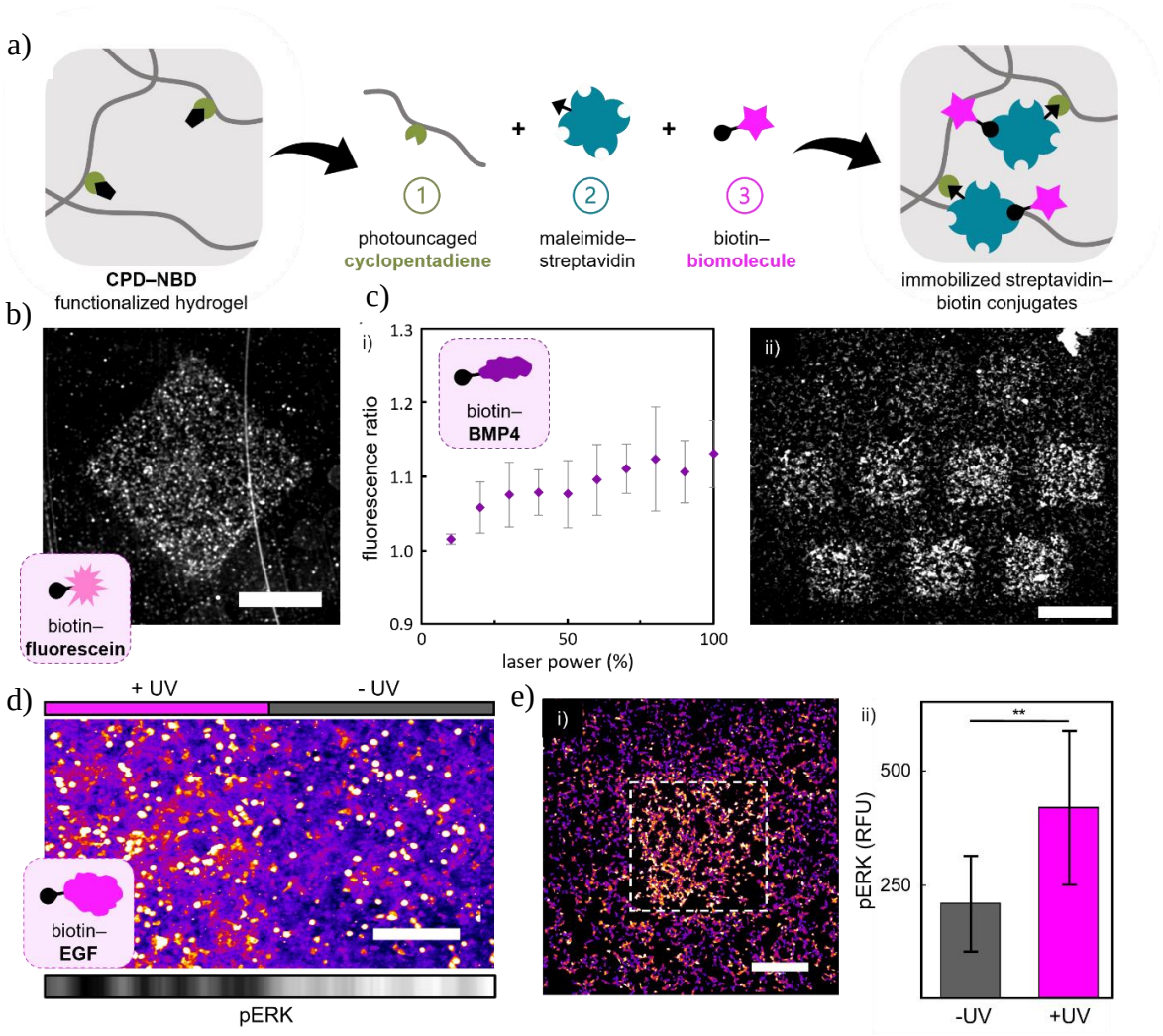

Figure 3.3. a) Schematic depiction of "mix-and-match" strategy by patterning maleimide–streptavidin and immobilizing biotinylated biomolecules. b) Image of immobilized biotin-fluorescein on fibronectin gel after masked irradiation (LED, 365 nm, 6 mW/cm^2). Scale bar = 250 µm. c) *i*) Immunofluorescence signal of BMP4 staining represented as ratio of pattern to background. *ii*) Immunofluorescent stain of biotin-BMP4 immobilized on Matrigel. Data presented as mean +/- standard deviation. n=2. d) Increased pERK staining on area with immobilized EGF (left) after masked irradiation. Heatmap at bottom represents relative pERK intensity. Scale bar = 250 µm. e) *i*) phospho-ERK (pERK) stain on DMD-patterned surface (dotted square corresponds to projected pattern). *ii*) Quantification of whole-cell pERK inside (+UV) and outside (-UV) of irradiated region. Data presented as mean +/- standard deviation. **p < 0.001. n = >300 cells.

To understand the extent of ERK control enabled through this approach we measured the dynamics of ERK activity in single cells on EGF-functionalized. We utilized the ERK Kinase Translocation Reporter (ERK-KTR)[27] and a custom computational analysis pipeline to quantify the effects of EGF-functionalized surfaces on dynamics (**Figure 3.4 a, Figure S3.4**). HeLa cells expressing the ERK-KTR were seeded on functionalized fibronectin. Following serum-depletion, we observed demonstrable increases in ERK activity over the course of six hours in EGF-functionalized wells while cells on non-irradiated surfaces showed only basal ERK activity (**Figure 3.4 b, c**). Remarkably, activated ERK was sustained through the entire duration of the experiment (6 hours) suggesting that our EGF functionalized ECM is resistant to receptor-level negative feedback that reduces pathway activity after activation with soluble ligands[28,29].

Without an available maleimide to undergo the click reaction, the uncaged Cp on the protein surfaces can slowly dimerize[30]; potentially increasing the material stiffness and driving ERK signaling[31]. Given the rapid reaction kinetics of the maleimide-Cp cycloaddition we anticipated negligible Cp dimerization would occur in our patterned surfaces[32]. Nonetheless we wanted to assess the potential impact of matrix stiffening on cell phenotypes by analyzing ERK activity on a CPD-NBD surface that had been irradiated to uncage Cp, but left untreated with maleimide-streptavidin/biotin-EGF to promote Cp dimerization. Minimal increases in ERK activity were noticed on the Cp surface compared to the non-treated and non-irradiated surfaces presented in Figure 4c and d. We reasoned that this represents the upper limit of matrix stiffening possible with our photopatterning platform and that the immediate addition of maleimide-streptavidin following Cp uncaging would out-compete the significantly slower Cp-Cp dimerization reaction[32]. Thus, we can confidently conclude that patterned EGF is

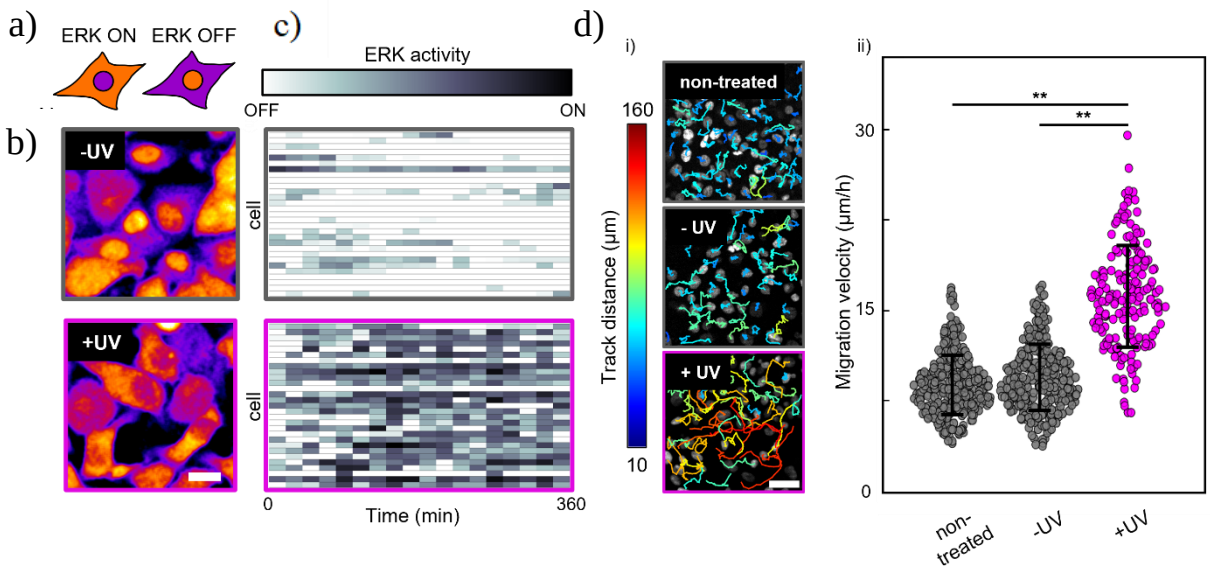

Figure 3.4. a) Schematic depiction of fluorescence readout for live-cell ERK activity reporter (ERK-KTR). b) HeLa cells on CPD-NBD-functionalized fibronectin. Non-irradiated surface is shown on the top and irradiated surfaces with immobilized EGF are on bottom. Scale bar = 25 µm. c) Relative ERK activity over 6 hours on surfaces. Single cells are represented across rows, with darker shades corresponding to increased ERK activity (low ratio of nuclear to cytoplasmic fluorescence). d) Representative cell tracks on EGF-functionalized fibronectin *i*) and velocity *ii*) over 6 hours. Scale bar = 50 µm. Data presented as standard error of the mean. **p<0.001. n=240 +/- 60 cells.

primarily responsible for the significant increase in ERK activity observed on fully functionalized surfaces.

Finally, we sought to test whether our functionalized ECM proteins could be used to control cell migration. Thus, we measured the migration of HeLa cells on EGF-functionalized fibronectin in comparison to unirradiated and Cp-dimerization controls. Remarkably, we found that cells on EGF-functionalized fibronectin migrated at roughly twice the velocity as those on non-functionalized fibronectin (**Figure 3.4 d**) and only a minimal increase in migration was observed on Cp-dimerization control surfaces (**Figure S3.5)**. Overall, these experiments demonstrate that our CPD-NBD photopatterning platform can be used to program cell phenotypes in space.

3.3 – *Discussion*

Microlithographically-engineered hydrogels, that allow for precise, user-defined patterning of biological cues, have the potential to advance our understanding of how cell behaviors orchestrate tissue-level decisions and provide a next-generation materials functionalization platform for tissue engineering. Current approaches to create morphogen-patterned microenvironments either utilize synthetic scaffolds, which deprive cells of natural signaling cues, or rely on cytotoxic radical-based chemistries, that can alter ECM structure. We present a novel material that utilizes a photocaged diene to arbitrarily immobilize proteins and small molecules through Diels-Alder chemistry, in radical-sensitive systems like natural ECM. By using a thiol-reactive CPD-NBD derivative that readily reacts with naturally occurring cysteine residues on ECM, our platform seamlessly integrates into standard surface functionalization protocols. Because of the large number of naturally occurring thiol groups

on ECM and the sensitivity of the CPD-NBD molecule our platform allows for highly tunable patterning as a function of irradiation intensity and time in all common ECM proteins. To interface with a large number of commercially available biotinylated protein ligands we incorporate a maleimide-streptavidin linker, thereby enabling the "mix-and-match" of any biotinylated species with any thiolated ECM network.

As a demonstration of CPD–NBD's capability for programming cell behaviors in a spatially-defined region of ECM, we created EGF-functionalized surfaces to instruct ERK signaling and motility of multiple mammalian cell types. ERK signaling dynamics are critically involved in development, regeneration, and disease; thus, methods that spatially engineer ERK activity offer exciting routes for studying the role of morphogens in guiding tissue organization. In addition, such substrates promise to enhance the reproducibility and precision of spatially engineered cell decisions. Future applications of this technology to intricately patterned stem cell fate choices promise to allow engineered systems to match the complexity of those observed in organismal development. Indeed, our demonstration of hESC viability on CPD-NBD functionalized laminin (**Figure S3.3**) indicates the compatibility of lithographic morphogen immobilization with developmental models to probe how localized "signaling centers" instruct cellular fates in a developing embryo.

Microlithographic patterning in 2D and 3D

While advances in microlithographic technologies have enabled scientists and engineers to pattern light with wavelength precision these powerful techniques have not been widely adopted in patterning tissues. Light-responsive bio-orthogonal molecules offer the opportunity to interface spatial patterning devices with biological systems. Here we report the

use of micromirror arrays to pattern light in 2D. In the future, we envision incorporating methods to spatially patterning light in 3D, such as by 2-photon and holographic approaches, into this platform. These mature light-delivery technologies will enable the application of microlithographic patterning to instruct the complex 3D architecture of human tissues, such as the patterning of vasculature, which has remained an unrealized goal of tissue engineering for decades. Thus, we imagine that the radical-free nature of CPD-NBD, along with a recently reported water-soluble CPD-NBD derivative[20], could provide an exciting approach for 3D patterned biomaterials.

Ligand-functionalized surfaces for achieving prolonged, high-intensity signaling

The binding affinity of natural ligands to their receptors is so high (Kd 1 – 10 nM) that, effectively, once the ligand-receptor complex is formed it does not unbind[33]. Thus, in order to initiate a new round of signaling, cells internalize and degrade receptor-ligand complexes. This process results in a characteristic timescale of signaling, which can fully determine a cell's fate, such as dictating the difference between growth and differentiation[34]. Interestingly, by tethering the ligand to a substrate it has been suggested that this internalization can be inhibited, thereby prolonging the signaling regime delivered by the activated receptor-ligand complex[35].

We noted that our functionalized surfaces promoted sustained signaling as well, likely due to the cell's inability to internalize the ECM-bound ligand. In solution EGF is rapidly internalized (<15 minutes)[28] along with its receptor, EGFR, with ERK activity decreasing steadily over the following 2 hours[29]. Remarkably cells grown on our EGF-functionalized fibronectin achieved sustained ERK activity throughout the entire duration of the experiment (6 hours). Such prolonged signaling may have several advantages. It could enable access to

cell fates that can only be achieved through continuous, long-term activation of a signaling pathway which are typically achieved with small molecule inhibitors in differentiation protocols and have been shown to induce transformation of some cells into cancer[36]. In addition, by efficiently delivering sustained signals our functionalized materials could be used to develop growth-promoting surfaces for implantation and tissue engineering.

Conclusion

We present the *de novo* synthesis and application of a novel photopatterning platform to spatially immobilize morphogens in ECM protein networks. The photosensitive CPD-NBD molecule readily binds ECM proteins without the need for any additional modifications to natural ECM. This property was used to establish surface functionalization protocols and interfaces with commercially available ligands that influence cell fates. We demonstrate the highly tunable nature of CPD-NBD photopatterning in four common ECM protein scaffolds and immobilize EGF as a use-case. We demonstrate the ability to engineer patterns of ERK activity, cell migrations, and prolonged signaling. This work illustrates the importance of expanding photopatterning technologies to protein-based matrices and provides a foundation for the patterning of growth factors to control stem cell fates. We anticipate that the ease with which CPD–NBD is integrated into cell culture protocols will promote its uptake and its continued development will be used to unlock new ways to study developmental morphogen gradients and patterns.

3.4 – *Materials & Methods*

CPD-NBD synthesis and characterization: CPD-NBD synthesis and characterization was done by Sophia Bailey of the Read de Alaniz group. Details are available in the publication associated with this chapter and Section 5.6 of Sophia's dissertation.

ECM surface preparation and patterning: To promote ECM gel attachment, 96-well glass bottom plates (Cellvis, P96-1.5H-N) were first functionalized with (3-aminopropyl)triethoxysilane (APTS) and glutaraldehyde. Under sterile conditions, each well was treated with 70 μL of APTS (2 vol%) in ethanol for 2 hours at room temperature then rinsed with ethanol followed by deionized water. Each well is then treated with 70 μL of glutaraldehyde (2 vol%) in deionized water for 2 hours at room temperature. The wells are then thoroughly rinsed with deionized water and allowed to dry before hydrogels are deposited in wells.

A 1 mM stock solution of CPD–NBD (**Compound 7**) was prepared in anhydrous dimethyl sulfoxide and was stored at 4 °C. This stock solution can be stored for months without any observable degradation. At the time of gel preparation, working solutions of CPD–NBD (1-100 μM) were prepared by diluting the stock (1 mM) CPD–NBD into the working solutions of respective polymers.

Matrix polymers* were diluted per manufacturers recommendations with the addition of CPD–NBD to desired concentrations (0– 100 μM). Immediately after mixing polymer solutions, 50 μL aliquots were transferred into the bottom of a functionalized 96-well plate. The plate was immediately centrifuged (1000 rpm) to promote even distribution of the thin protein gel on the bottom of the well plate. The distributed solutions were protected from light

and incubated at room temperature for 3 hours. Excess polymer and CPD–NBD were rinsed from the wells with PBS and surfaces were patterned as indicated.

*Matrix polymers used:

- Collagen Type I, Corning, PN 354249
- Matrigel Basement Membrane Matrix, Corning, PN 354234
- Laminin-521, Stem Cell Technologies, PN 200-0117
- Fibronectin Bovine Protein, Gibco, PN 33010018

CYS_d Determination:

Polymer	***Uniprot ID***	***% Cysteine***	***Plating density, µg/mL***	***CYS_d***
Fibronectin	PO7589	2.5	10	25
Collagen	PO2454	1.2	50	60
Laminin	PO7924	7.1	10	71
Matrigel**	-	-	100	-

*** The approximate composition of Matrigel is 60% laminin and 30% collagen VI. The remaining 10% is composed of enactin and trace amounts of other ECM proteins, growth factors, and peptides that likely significantly alter the concentration of reactive cysteines within the gel. Because of the heterogeneity in Matrigel's reported composition, and large batch-to-batch variations, we did not calculate a CYS_d for Matrigel.*

Hydrogels were patterned by irradiating in a bottom-up fashion through the 1.5H glass bottom well plate with a collimated LED (Thorlabs, M365L2-C1, 365 nm, 6 mW/cm^2), or digital micromirror device (DMD, Dual Mightex Polygon 400) equipped with the Nikon W2 SoRa spinning-disk confocal microscope (365 nm). DMD patterns were done through a 10X

objective (CFI PLAN APO LAMBDA 10X) for 10 minutes. After irradiation, PBS was removed from each well then maleimide containing solutions were deposited on the top of each gel and gently agitated to ensure complete well coverage. Surfaces were incubated with 0.1–10 μM AlexaFluor-maleimide (Invitrogen™, A20346) or 1 μM maleimide-streptavidin (CellMosaic®, CM52401) for 1.5–3 hours at room temperature. Surfaces treated with maleimide-streptavidin were thoroughly rinsed (> 10 well volumes) with PBS before incubating with the appropriate biotin-bearing proteins at indicated concentrations for an additional 1.5 hours at room temperature. Surfaces were thoroughly rinsed before imaging or seeding cells.

Tissue culture and viability: HeLa, HEK, and 3T3 cells were cultured at 37°C with 5% CO_2 in Dulbecco's Modified Eagle Medium (DMEM) containing 10% fetal bovine serum and 1% antibiotic (25units/mL penicillin, 25μ g/mL streptomycin, Invitrogen). Serum-depleted media was made by adding fetal bovine serum to 0.5%. Cells were seeded on functionalized surfaces at 20,000-40,000 cells/well and allowed to adhere overnight before being placed in serum-depleted media for indicated times.

Cell viability assessed with AlamarBlue Cell Viability Reagent (Invitrogen, DAL1025). Briefly, cells growing on functionalized matrices were incubated in media supplemented with 10% AlamarBlue solution. After an hour, 100 μL samples of media were taken and fluorescence signal (Ex/Em 560 nm/590 nm) was quantified with a plate reader (Biotek) (**Figure S3.2**).

Stem cell culture and differentiation: Experiments in hESC lines were done using the H9 hESC line purchased from the William K. Bowes Center for Stem Cell Biology and Engineering at University of California, Santa Barbara. hESCs were propagated on Matrigel-coated (Corning) tissue culture dishes in mTeSR Plus medium (Stem Cell Technologies). For experiments, hESCs were seeded on to laminin-coated (Stem Cell Technologies) wells of a 96-well plate at 40,000-50,000 cells per well in the presence of ROCK inhibitor Y-27632. The following day ROCK inhibitor was removed, and differentiation was induced with BMP-4 (Stem Cell Technologies, 78211) (50 ng/mL) for 48 hours.

ERK-KTR analysis and distance tracking: Live-cell ERK-KTR videos were analyzed with hand-drawn ROIs at each timepoint. Nuclei were identified with fluorescent tags and the surrounding area was assumed to be the cytoplasm. Distance tracking was done using the TrackMate plugin in FIJI. See **Figure S3.4**.

Immunofluorescence: Cells were fixed with 4% PFA for 25 minutes followed by permeabilization with ice cold methanol for 10 minutes. Samples were blocked with a 1% BSA solution and incubated overnight in the appropriate primary antibody (1:200). The following day samples were rinsed and incubated with Alexa-conjugated secondary antibodies (1:1000).

Statistical analysis, image collection, and processing: All imaging was done with a Nikon W2 SoRa spinning-disk confocal microscope. When necessary, an incubation chamber was used to maintain 37 °C and 5% CO_2. Migration distance was tracked using the FIJI plugin TrackMate[8] and further analyzed and plotted using custom MATLAB (R2022a) scripts. ERK-KTR and pattern intensity were analyzed with hand-picked ROIs and processed in FIJI and

MATLAB with custom scripts. Comparisons were done with a two-sample t-test ('ttest2' MATLAB function) and p-values < 0.001 were deemed significant.

Patterned molecules:

Molecule	**Vendor**	**Product #**
Alexa fluor 555 C_2 Maleimide (Alexa-mal)	Invitrogen	A20346
Maleimide Activated Streptavidin	CellMosaic	CM52401
Biotin-4-4Fluorescein	Invitrogen	B10570
BMP4 (human) recombinant, Biotinylated	Aviscera Bioscience	00014-01-50B
Epidermal Growth Factor, Biotin-XX Conjugate (biotin EGF)	Invitrogen	E3477

3.5 – *Acknowledgements & References*

I would like to thank Sophia Bailey and Professor Javier Read de Alaniz for their collaborative efforts in developing the CPD-NBD photopatterning platform. Their expertise, innovative thinking, and enthusiasm were a driving force in the progression of this project. Working with Sophia was truly a highlight of my graduate training and it is impossible to overstate what I learned from her as a scientist and a friend during this process – Sophia, I wish you all the best in your scientific endeavors. Furthermore, I would like to thank the BioPACIFIC Materials Innovation Platform (MIP) of the National Science Foundation (award No. DMR-1933487) for financial support.

1. Morales, J. S., Raspopovic, J. & Marcon, L. From embryos to embryoids: How external signals and self-organization drive embryonic development. *Stem Cell Rep.* **16**, 1039–1050 (2021).

2. Wang, S.-J., Saadi, W., Lin, F., Minh-Canh Nguyen, C. & Li Jeon, N. Differential effects of EGF gradient profiles on MDA-MB-231 breast cancer cell chemotaxis. *Exp. Cell Res.* **300**, 180–189 (2004).

3. Bénazéraf, B. *et al.* A random cell motility gradient downstream of FGF controls elongation of an amniote embryo. *Nature* **466**, 248–252 (2010).

4. Ohnishi, Y., Yasui, H., Kakudo, K. & Nozaki, M. Regulation of cell migration via the EGFR signaling pathway in oral squamous cell carcinoma cells. *Oncol. Lett.* **13**, 930–936 (2017).

5. Grim, J. C., Marozas, I. A. & Anseth, K. S. Thiol-ene and photo-cleavage chemistry for controlled presentation of biomolecules in hydrogels. *J. Controlled Release* **219**, 95–106 (2015).

6. Munoz-Robles, B. G., Kopyeva, I. & DeForest, C. A. Surface Patterning of Hydrogel Biomaterials to Probe and Direct Cell–Matrix Interactions. *Adv. Mater. Interfaces* **7**, 2001198 (2020).

7. Luo, Y. & Shoichet, M. S. A photolabile hydrogel for guided three-dimensional cell growth and migration. *Nat. Mater.* **3**, 249–253 (2004).

8. DeForest, C. A., Polizzotti, B. D. & Anseth, K. S. Sequential click reactions for synthesizing and patterning three-dimensional cell microenvironments. *Nat. Mater.* **8**, 659–664 (2009).

9. Wade, R. J., Bassin, E. J., Gramlich, W. M. & Burdick, J. A. Nanofibrous Hydrogels with Spatially Patterned Biochemical Signals to Control Cell Behavior. *Adv. Mater.* **27**, 1356–1362 (2015).

10. Batalov, I., Stevens, K. R. & DeForest, C. A. Photopatterned biomolecule immobilization to guide three-dimensional cell fate in natural protein-based hydrogels. *Proc. Natl. Acad. Sci.* **118**, (2021).

11. DeForest, C. A. & Tirrell, D. A. A photoreversible protein-patterning approach for guiding stem cell fate in three-dimensional gels. *Nat. Mater.* **14**, 523–531 (2015).

12. Broguiere, N. *et al.* Morphogenesis Guided by 3D Patterning of Growth Factors in Biological Matrices. *Adv. Mater.* **32**, 1908299 (2020).

13. Caliari, S. R. & Burdick, J. A. A practical guide to hydrogels for cell culture. *Nat. Methods* **13**, 405–414 (2016).

14. Dean, R. T., Fu, S., Stocker, R. & Davies, M. J. Biochemistry and pathology of radical-mediated protein oxidation. *Biochem. J.* **324**, 1–18 (1997).

15. Williams, C. G., Malik, A. N., Kim, T. K., Manson, P. N. & Elisseeff, J. H. Variable cytocompatibility of six cell lines with photoinitiators used for polymerizing hydrogels and cell encapsulation. *Biomaterials* **26**, 1211–1218 (2005).

16. Bryant, S. J., Nuttelman, C. R. & Anseth, K. S. Cytocompatibility of UV and visible light photoinitiating systems on cultured NIH/3T3 fibroblasts in vitro. *J. Biomater. Sci. Polym. Ed.* **11**, 439–457 (2000).

17. Wylie, R. G. *et al.* Spatially controlled simultaneous patterning of multiple growth factors in three-dimensional hydrogels. *Nat. Mater.* **10**, 799–806 (2011).

18. Mosiewicz, K. A. *et al.* In situ cell manipulation through enzymatic hydrogel photopatterning. *Nat. Mater.* **12**, 1072–1078 (2013).

19. Bailey, S. J., Stricker, F., Hopkins, E., Wilson, M. Z. & Read de Alaniz, J. Shining Light on Cyclopentadienone–Norbornadiene Diels–Alder Adducts to Enable Photoinduced Click Chemistry with Cyclopentadiene. *ACS Appl. Mater. Interfaces* **13**, 35422–35430 (2021).

20. Bailey, S. J. *et al.* Design, Synthesis, and Application of a Water-soluble Photocage for Aqueous Cyclopentadiene-based Diels–Alder Photoclick Chemistry in Hydrogels. *Angew. Chem. Int. Ed.* (2023) doi:10.1002/anie.202301157.

21. Ting, C.-Y. *et al.* Cyclopentadiene as a Multifunctional Reagent for Normal- and Inverse-Electron Demand Diels–Alder Bioconjugation. *Bioconjug. Chem.* **33**, 1609–1619 (2022).

22. Hopkins, E. *et al.* An Optogenetic Platform to Dynamically Control the Stiffness of Collagen Hydrogels. *ACS Biomater. Sci. Eng.* **7**, 408–414 (2021).

23. Karamanos, N. K. *et al.* A guide to the composition and functions of the extracellular matrix. *FEBS J.* **288**, 6850–6912 (2021).

24. Le, Q., Nguyen, V. & Park, S. Recent advances in the engineering and application of streptavidin-like molecules. *Appl. Microbiol. Biotechnol.* **103**, 7355–7365 (2019).

25. The epidermal growth factor. - Boonstra - 1995 - Cell Biology International - Wiley Online Library. https://onlinelibrary.wiley.com/doi/abs/10.1006/cbir.1995.1086.

26. Ley, R., Balmanno, K., Hadfield, K., Weston, C. & Cook, S. J. Activation of the ERK1/2 Signaling Pathway Promotes Phosphorylation and Proteasome-dependent Degradation of the BH3-only Protein, Bim *. *J. Biol. Chem.* **278**, 18811–18816 (2003).

27. de la Cova, C., Townley, R., Regot, S. & Greenwald, I. A Real-Time Biosensor for ERK Activity Reveals Signaling Dynamics during C. elegans Cell Fate Specification. *Dev. Cell* **42**, 542-553.e4 (2017).

28. Henriksen, L., Grandal, M. V., Knudsen, S. L. J., van Deurs, B. & Grøvdal, L. M. Internalization Mechanisms of the Epidermal Growth Factor Receptor after Activation with Different Ligands. *PLoS ONE* **8**, e58148 (2013).

29. Goh, L. K., Huang, F., Kim, W., Gygi, S. & Sorkin, A. Multiple mechanisms collectively regulate clathrin-mediated endocytosis of the epidermal growth factor receptor. *J. Cell Biol.* **189**, 871–883 (2010).

30. Tran, T. M. & de Alaniz, J. R. Controlled Synthesis of a Homopolymer Network Using a Well-Defined Single-Component Diels–Alder Cyclopentadiene Monomer. *J. Am. Chem. Soc.* **145**, 3462–3469 (2023).

31. Labouesse, C. *et al.* StemBond hydrogels control the mechanical microenvironment for pluripotent stem cells. *Nat. Commun.* **12**, 6132 (2021).

32. Levandowski, B. J. & Raines, R. T. Click Chemistry with Cyclopentadiene. *Chem. Rev.* **121**, 6777–6801 (2021).

33. Sanders, J. M., Wampole, M. E., Thakur, M. L. & Wickstrom, E. Molecular Determinants of Epidermal Growth Factor Binding: A Molecular Dynamics Study. *PLoS ONE* **8**, e54136 (2013).

34. Ryu, H. *et al.* Frequency modulation of ERK activation dynamics rewires cell fate. *Mol. Syst. Biol.* **11**, 838 (2015).

35. Schwab, E. H. *et al.* Nanoscale Control of Surface Immobilized BMP-2: Toward a Quantitative Assessment of BMP-Mediated Signaling Events. *Nano Lett.* **15**, 1526–1534 (2015).

36. Lyra-Leite, D. M. *et al.* A review of protocols for human iPSC culture, cardiac differentiation, subtype-specification, maturation, and direct reprogramming. *STAR Protoc.* **3**, 101560 (2022).

3.6 – *Supplementary Information*

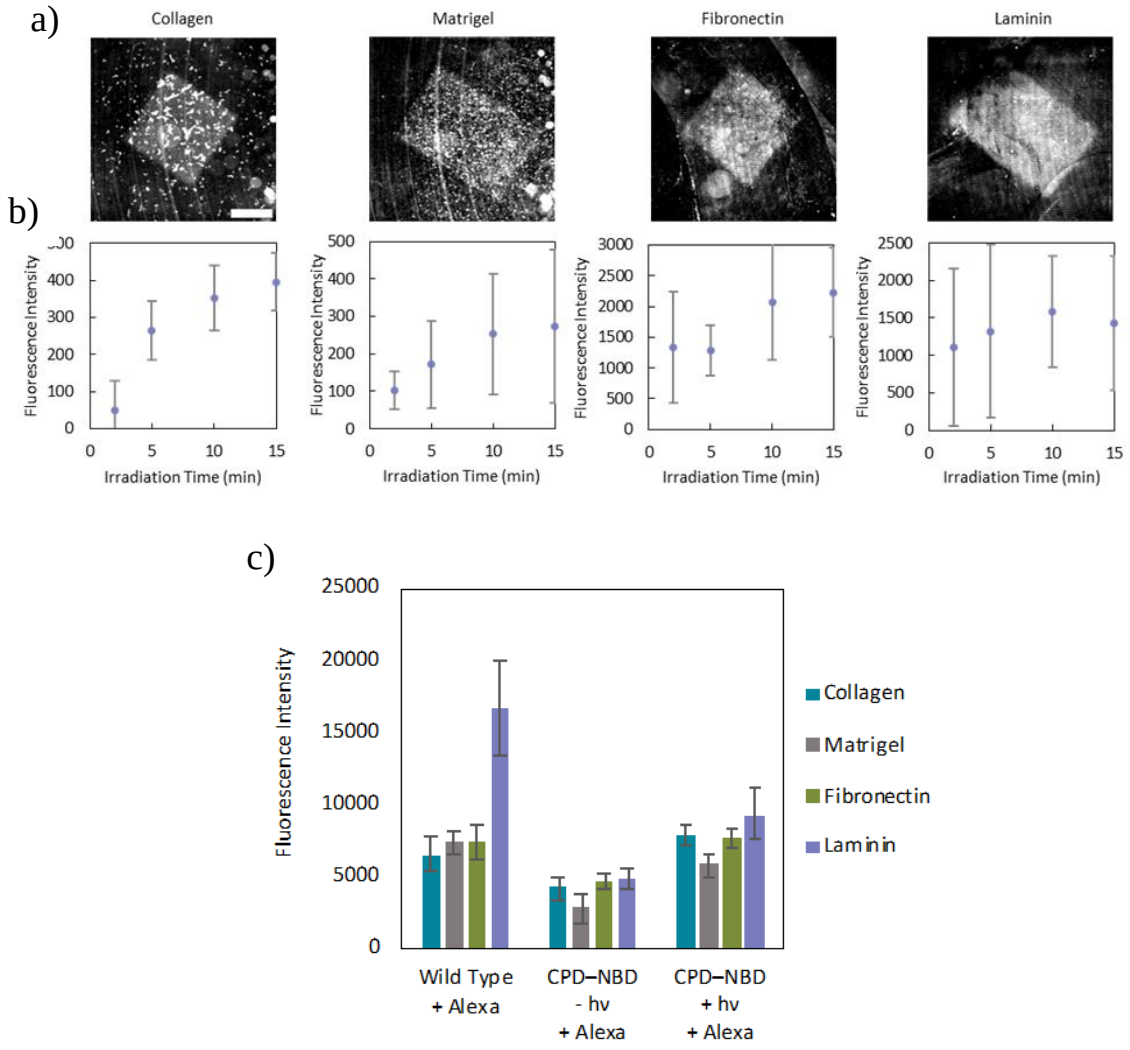

Figure S3.1. a) Representative images of patterned maleimide–Alexa Fluor 555 after irradiation (LED, 365 nm, 10 min, 6 mW/cm^2) in each protein-based matrix. b) Quantification of fluorescence as a function of irradiation time for each matrix. Scale bar = 100 µm. c) Fluorescence values of wild type surfaces treated with maleimide–Alexa reflecting cysteine–maleimide conjugation (Wild Type + Alexa) compared to CPD–NBD functionalized surfaces from **Figure 3.2** of nonirradiated background (CPD–NBD – *hv* + Alexa) and "100% Power" irradiated patterns (CPD–NBD + *hv* + Alexa). All fluorescence values are corrected to nontreated wild type surface fluorescence.

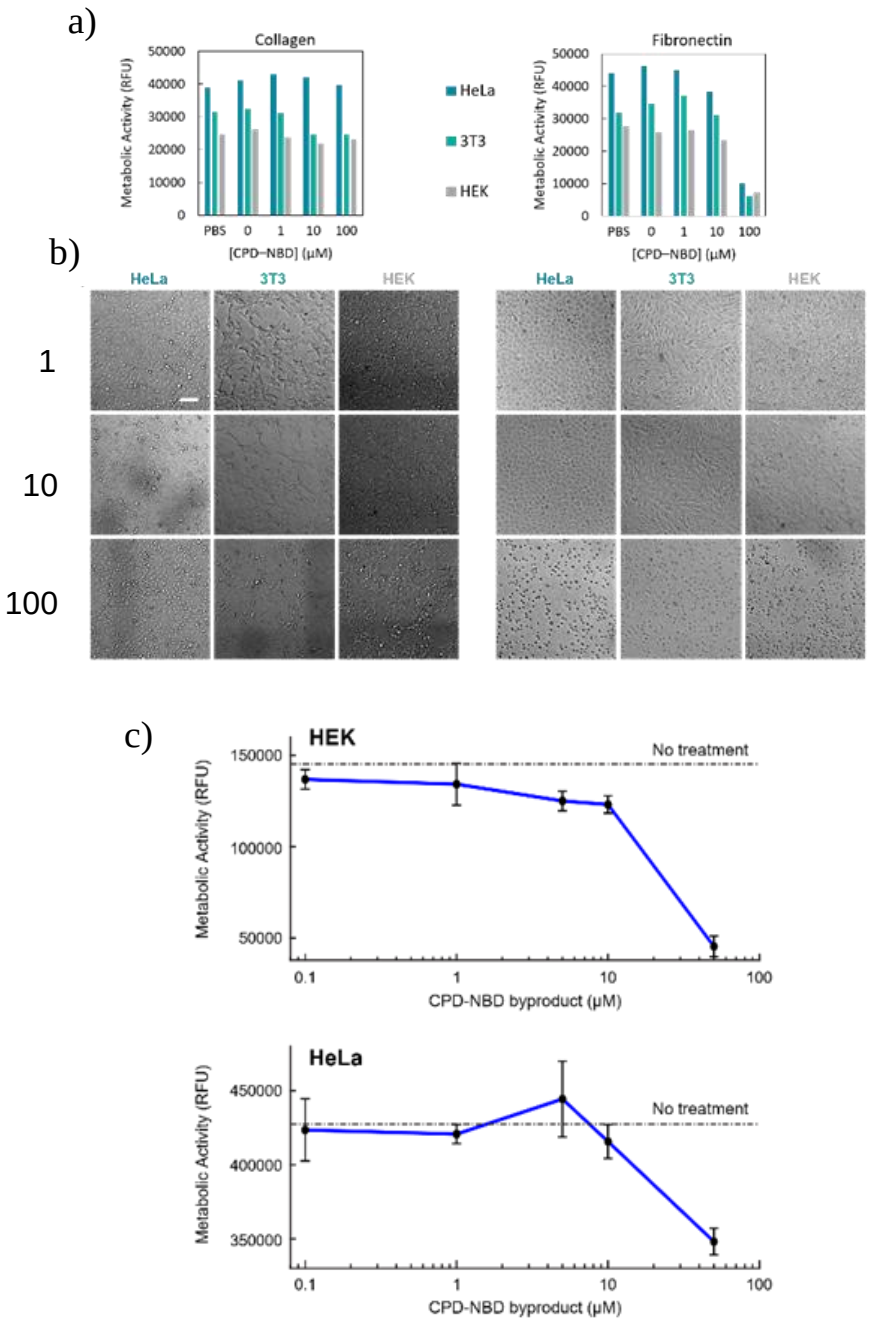

Figure S3.2. a) Plots of metabolic activity of HeLa, 3T3 and HEK cells cultured in PBS or on CPD–NBD functionalized surfaces (0–100 μM). b) Representative images of cell morphologies of HeLa, 3T3 and HEK cells on each surface. c) Metabolic activity of HEK and HeLa cells after 24 hours of culture in media supplemented with irradiated CPD-NBD at indicated concentrations. n=4 for each condition.

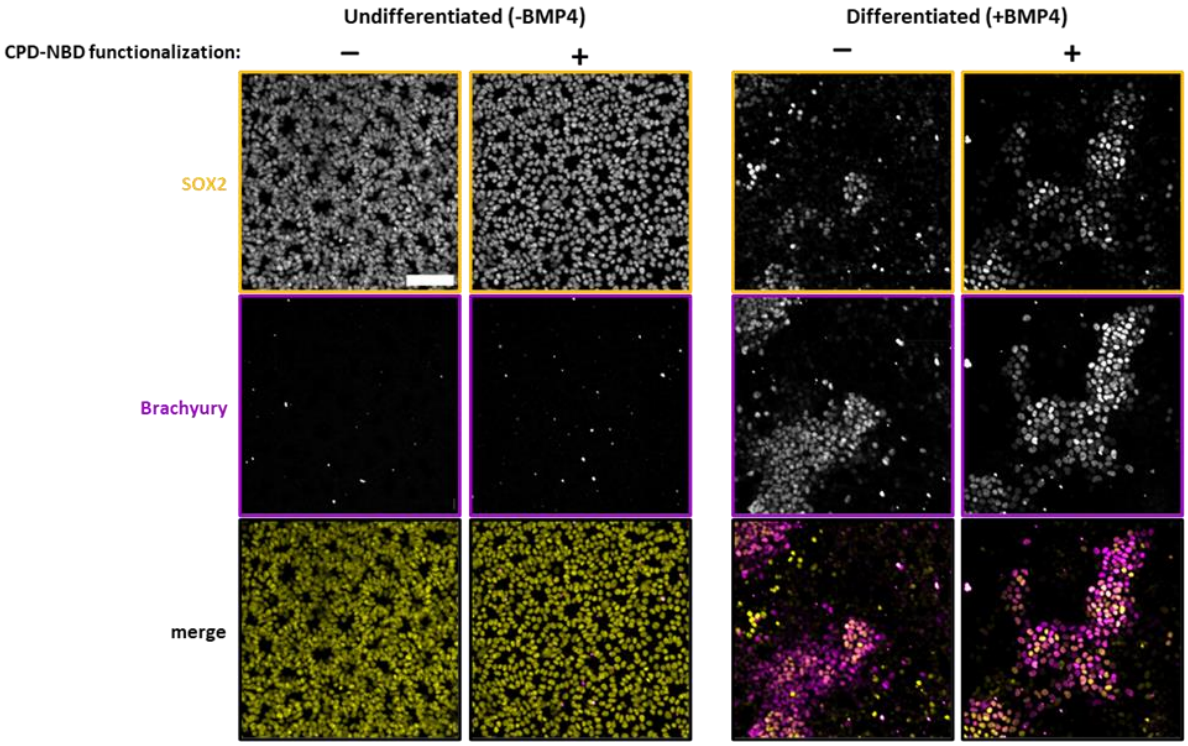

Figure S3.3. Differentiation of hESCs on CPD-NBD functionalized laminin and non-functionalized laminin. SOX2 and Brachyury markers indicate cells grown on CPD-NBD treated surfaces undergo mesodermal differentiation (BMP4-indcued) similar to those grown on non-treated surfaces. Scale bar = 100 µm.

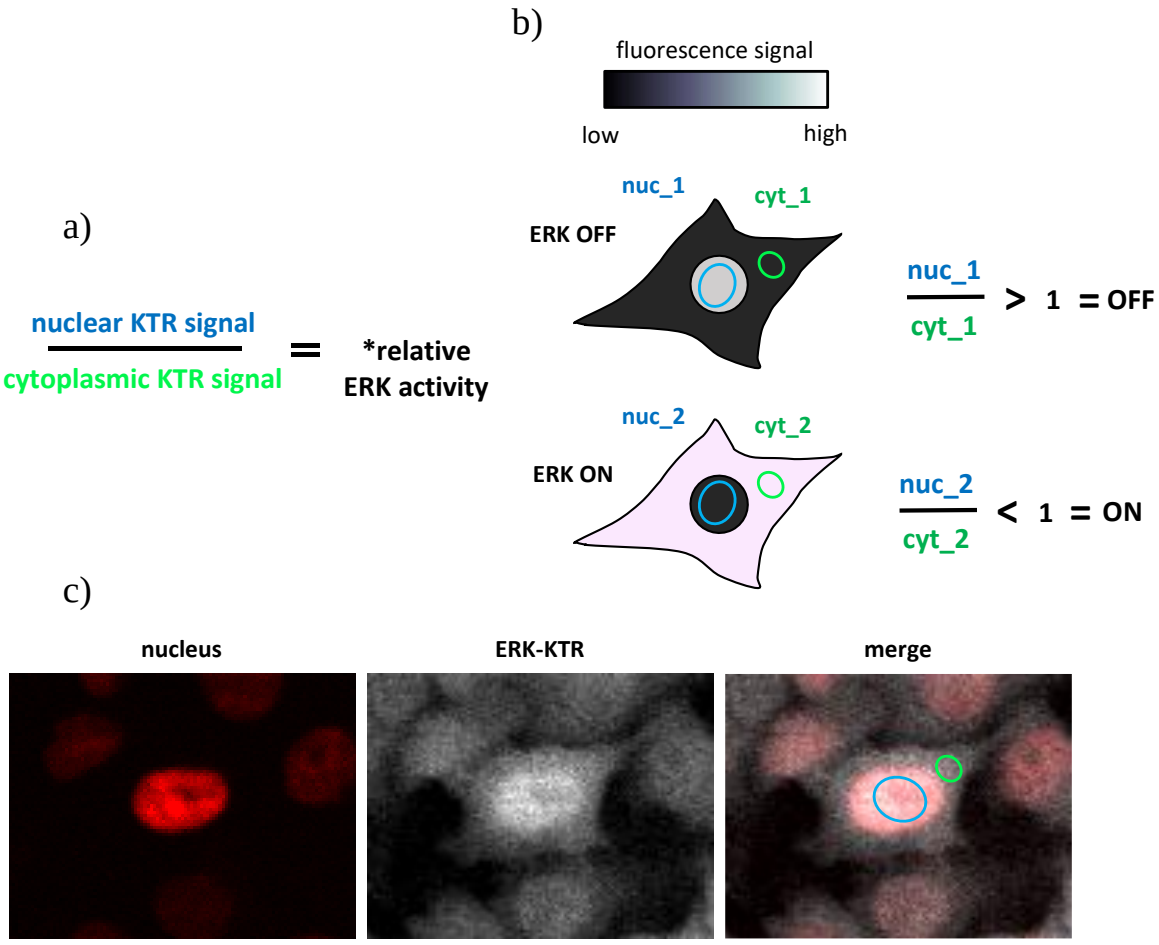

Figure S3.4. a) ERK activity is measured as the ratio of nuclear KTR to cytoplasmic KTR. * Relative activity is inversely related to this ratio, such that higher nuclear KTR signal represents ERK in the OFF state. b) Diagram of KTR localization while ERK is in the OFF state (*top*) and the ON state (*bottom*). Each cell is analyzed with a nuclear and cytoplasmic ROI at each timepoint. c) Representative image of fluorescent tag used to identify the nucleus (*left*), ERK-KTR (*middle*), and merged image with ROIs.

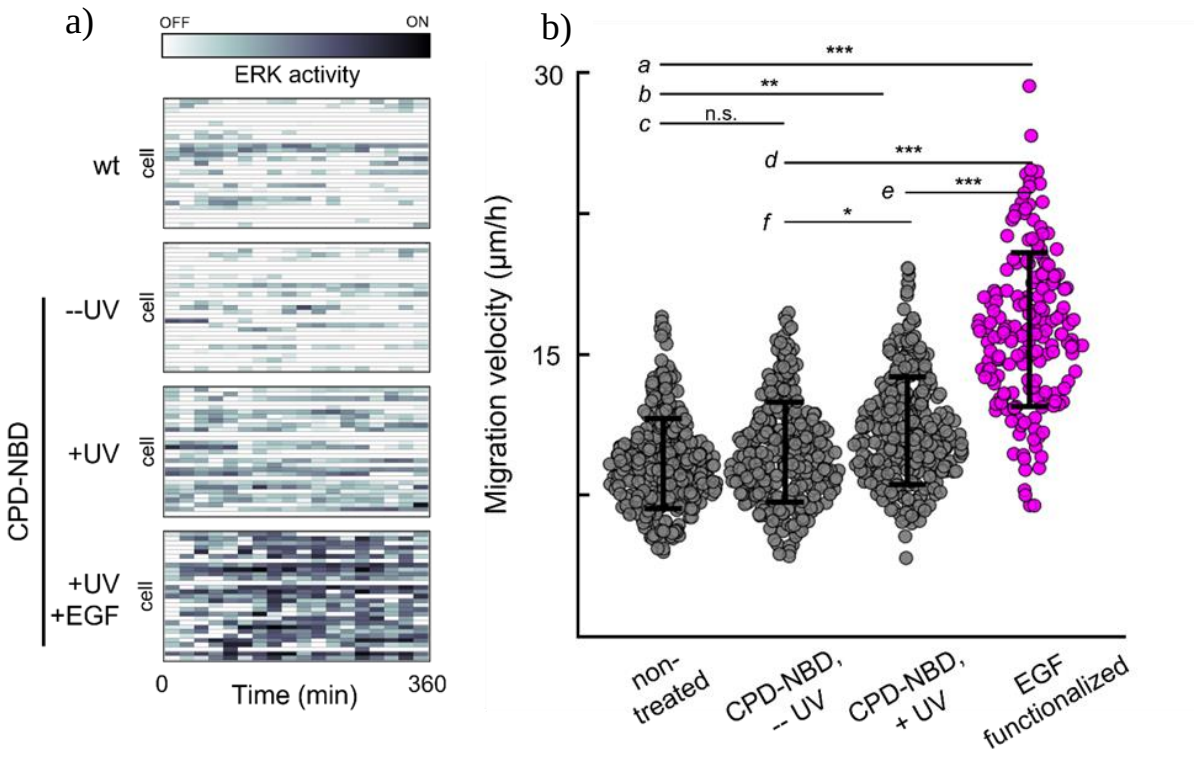

Figure S3.5. a) HeLa cell ERK activity and b) migration velocity on indicated surfaces. From Figure 4d, with additional control for deprotected CPD-NBD fibronectin (CPD-NBD, +UV). n.s. = p > 0.001. * = p<1e-5. ** = p<1e-10. *** = p<1e-50.

CHAPTER 4: Synthetic Wnt Signaling: Novel Proteins for Controlling the Wnt Pathway and Uses in Tissue Engineering

4.1 – *Introduction*

The Wnt/β-catenin signaling pathway is highly conserved across metazoan lineages and plays key roles in cellular proliferation, differentiation, and disease progression[2]. Canonical Wnt signaling is initiated when a Wnt ligand binds co-receptors Frizzled (Fz) and Low-density lipoprotein receptor-related proteins 6 (LRP6) on the cell surface, leading to glycogen synthase kinase 3 (GSK3) inhibition and subsequent intracellular accumulation of the central transcriptional effector, β-catenin, to drive expression of Wnt-regulated genes[3]. This process is tightly regulated during embryonic development and within fully formed organisms, however the large number of co-receptors (10 members of the Fz family) and Wnt ligands (19 members of Wnt family) has made sub-type specific signaling outcomes difficult to elucidate while the highly-modified and lipidated nature of Wnt ligands yields further technical hurdles for their ex vivo production[4–7].

Wnt's role as a fundamental mediator of cell proliferation and differentiation makes it unsurprising that the pathway is a target of numerous therapeutics[8,9]. Overactivation is associated with several cancers[10], Alzheimer's disease[11], and type II diabetes[12] while deficiencies hinder regenerative capacities and underly diseases such as osteoporosis[13], vitiligo[14], and neurodegeneration[11]. Indeed, augmenting Wnt signaling in various disease and injury models improves the regenerative capacities of bone[8,15], intestinal [16], and dermal tissues [17] and improves post-ischemia renal function[18]. Thus, there is undoubtedly growing therapeutic interest in Wnt's regenerative capabilities and developing modular approaches to activate the pathway.

Given Wnt's importance for cellular homeostasis and embryonic development, synthetic approaches for modulating Wnt activity have been developed to circumvent activating the pathway with natural ligands. The most common of these is the small molecule CHIR99021 (CHIR), that promotes the accumulation of β-catenin through inhibition of GSK3[19,20]. GSK3 interactions, however, are promiscuous and influence pathways like insulin signaling[21], AKT[22], and hedgehog[23], which drives non-specific outcomes. Genetically encoded approaches offer dynamic control over pathway activation through light or chemically-induced receptor dimerization, but their widespread use is limited by the need to create stably-modified cell lines[24,25]. More recently, synthetic ligands comprised of Fz- and LRP6- binding domains have proven to be viable Wnt agonists and demonstrate improved solubility and manufacturing capabilities compared to the heavily lipidated natural Wnt ligands[15,26–29].Additionally, the modular design of these synthetic Wnts allows them to be targeted to specific receptor sub-types and control receptor valency, thus offering ways to study how receptor sub-types influence tissue development[27,28,30]. Furthermore, synthetic ligands have demonstrated regenerative potential by prolonging the lifespan of in vitro organoids. While such synthetic ligands are a promising step for utilizing the regenerative capacity of Wnt signaling, receptor engagement is still dependent on post-translationally modified domains thus limiting their production to eukaryotic systems.

Here we present a novel synthetic Wnt ligand (Wnt Barbell) that can be purified at high concentrations from simple bacterial expression systems. The bivalent molecule potently stimulates the canonical Wnt pathway by inducing proximity of Fz and LRP6 and is subject to regulation by the natural Wnt modulators Dickkopf-related protein 1 (Dkk1) and R-spondin (Rspo1). We demonstrate that The Barbell induces mesoderm in human stem cell populations

and can be used to further derive cardiac tissue and enhance osteogenic differentiation of mesenchymal stem cells. Overall, this work adds a novel molecule to the toolbox of synthetic Wnt modulators and holds promise for use in engineering Wnt signaling for regenerative purposes.

4.2 – *Results*

4.2.1 Wnt Barbell Design

Akin to other synthetic Wnts, we reasoned that inducing receptor proximity with a bivalent molecule targeting the extracellular domains (ECDs) of Fz and LRP6 would mimic the function of endogenous Wnt ligands to activate signaling (**Figure 4.1 a**). Furthermore, we wanted to make the Barbell amenable to bacterial expression to facilitate production and increase yield in comparison to eukaryotic expression systems. Thus we chose to construct the Wnt Barbell with an LRP6-specific nanobody (D07)[31] and a Frizzled cysteine-rich domain (Fz-CRD) synthetic binder Designed Repeat Protein Binder Fz-7/8 (DRPB-7/8))[32] separated by a 10 amino acid GS linker (**Figure 4.1 b, Figure S4.1)**.

The Wnt antagonist Dkk1 is commonly utilized as an LRP6-binder in synthetic Wnts[28], however glycosylation sites on Dkk-1 hinder its proper expression in bacteria [33] and require lower-yield eukaryotic expression systems. Alternatively, the compact and stable nature of nanobodies allows them to be easily purified from simple bacterial expression systems. D07 shares a binding site with the C-terminus of Dkk1 (Dkk1_C) on the PE3 domain of LRP6 and binds the receptor with two-fold the affinity (D07-30nM, Dkk1_C-67nM)[31,34].

DRPB-7/8 is a Fz-targeted DARPin (Designed Ankyrin Repeat Protein) that is amenable to bacterial expression. It's high specificity and affinity toward the Fz-CRD has been

effectively utilized in the construction of previous synthetic Wnts as a fusion with Dkk1_C[28,32]. As expected, bacterial expression (100mL) of the Barbell resulted in high levels of soluble protein that could be routinely purified for future use (**Figure S4.2 a**).

4.2.2 Barbell is Potent Activator of Wnt Pathway

The heterofunctional design of the Barbell suggests it will simultaneously interact with LRP6 and Fz to drive heterodimerization, however we wanted to experimentally verify that Barbells form a Fz:Barbell:LRP6 complex. Mass photometry readings of the individual species (LRP6, Barbell, or Fz) show clear peaks corresponding to each protein's respective molecular weight (**Figure 4.1 c – *black, grey, red***). The Fz-CRD appeared to exist as a dimer (~90kDa), however this aligns with previously reported structural studies for the Fz-CRD[35,36]. Nonetheless, when the species were observed in the same solution, a new high-molecular weight peak was observed, suggesting that a the Wnt Barbell mediated the formation of a complex containing LRP6, Barbell, and Fz-CRD (**Figure 4.1 c – *blue*)**. Following confirmation that Barbells induce proximity between LRP6 and Fz, we wanted to test their ability to activate Wnt signaling. We used a HEK293T cell line expressing endogenously tagged β-catenin (tdmRuby3) and a translational reporter under the control of seven TCF/LEF sites (miRFP) (HEK:bCat_miRFP-TF) to monitor nuclear β-catenin accumulation and translational activity across a broad range of Barbell concentrations.

After 24 hours of treatment the Barbell induced beta-catenin accumulation and translation of beta-catenin-regulated genes, as noted by elevated levels of nuclear beta-catenin and miRFP (**Figure 4.1 d,e, Figure S4.2 d**). These characteristic Wnt responses were observed

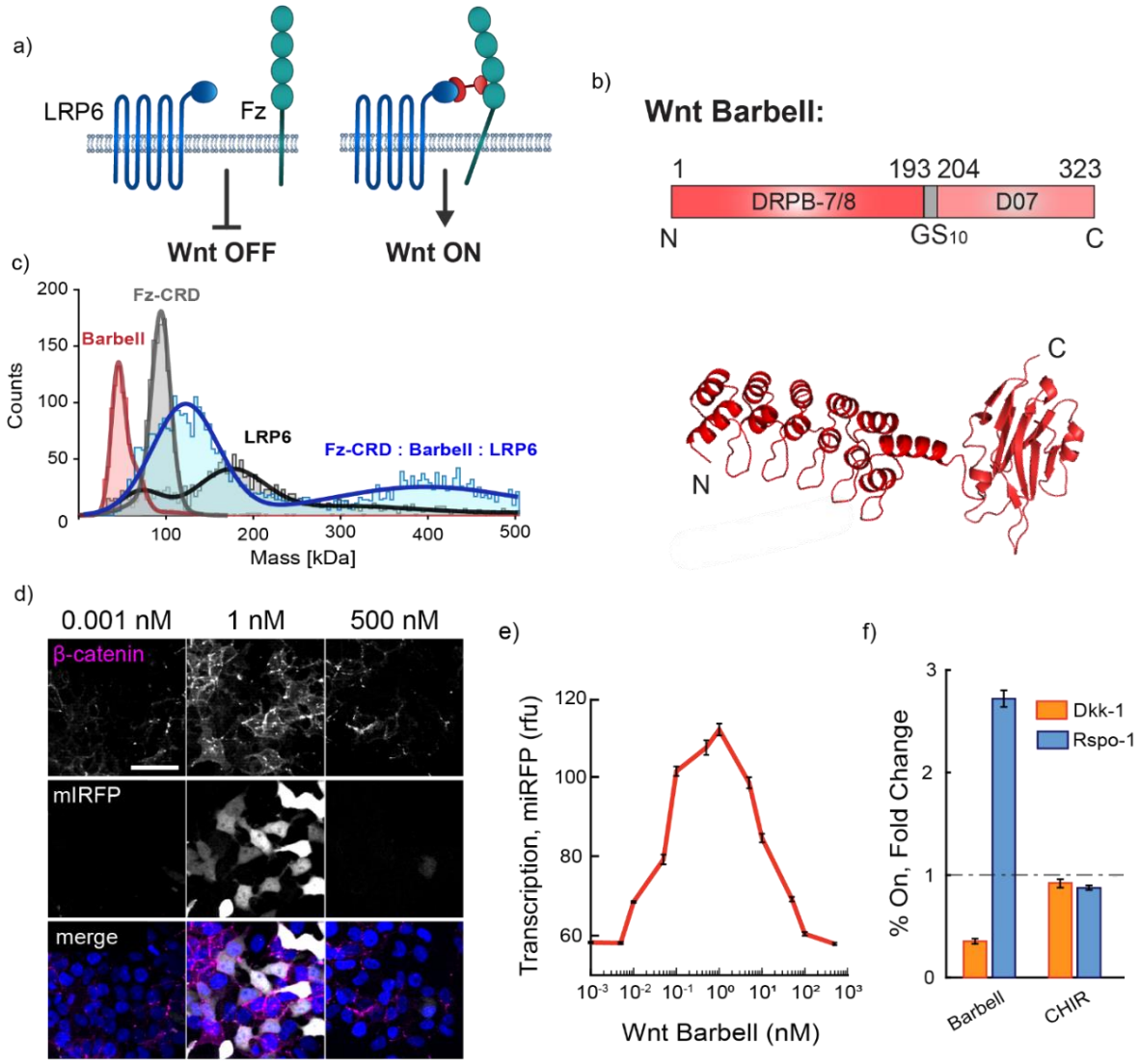

Figure 4.1 a) Simplified diagram of Wnt pathway activation. b) Wnt Barbell fusion protein (*top*) and structure of Wnt Barbell generated from RoseTTAFold. c) Mass distribution for Wnt Barbell (red), Fz-CRD (grey), LRP6 (black), and Fz-CRD:Barbell:LRP6 binding complex (blue). d) Representative images of β-catenin and mIRFP accumulation following 24 hours of Barbell treatment at indicated concentrations. Scale bar = 100µm. e) Quantification of translational activity (miRFP) across all tested Barbell concentrations. f) Changes in Barbell- (1 nM) and CHIR- (10 µM) induced Wnt activity in the presence of Dkk-1 or Rspo-1. Responses are normalized to unmodified response level for the respective agonist (-Dkk-1, -Rspo-1).

over a wide concentration of treatments and were completely abrogated in co-treatments of non-fused DRPB-7/8 and D07 (**Figure S4.2 e**).

Given that the Barbell initiates signaling at the receptor-level, unlike small molecules with intracellular targets [19], we reasoned that Barbell-induced signaling would be regulated by naturally secreted Wnt modulators. We tested the Barbell's activity (1nM) in the presence of Dkk1 (100ng/mL) and Rspo-1 (10nM), which interact with extracellular domains of LRP6 to negatively and positively regulate Wnt signaling, respectively[34,37]. As expected, Dkk1 attenuated signaling induced by the Barbell affect CHIR-induced signaling (10 μM). Likewise, Wnt signaling was strongly potentiated in the presence of the Barbell with Rspo-1 but not CHIR with Rspo-1 (**Figure 4.1 f**).

4.2.3 Barbell Induces Mesoderm Fate in Human Stem Cells

Wnt signaling is essential for mesoderm formation during early embryonic development and serves as a precursor for the formation of specific cell types and tissues [38], thus we chose to test the Barbell's ability to induce mesoderm in human embryonic stem cells (hESC). Mesoderm commitment is marked by the upregulation of mesoderm-specific transcription factors, such as brachyury (BRA), and the downregulation of neural-specific markers, like SRY-Box transcription factor 2 (SOX2) [39,40]. Immunofluorescence staining following a 48-hour differentiation with the Barbell revealed a pronounced increase in BRA expression at intermediate concentrations (0.1-10 nM). In alignment with our observations in HEK293T cells, we noted a decrease in the Wnt response at elevated concentrations, as BRA expression steadily declined with treatments above 10 nM (**Figure 4.2 a,b – *top*)**. Interestingly, Barbell treatments that induced peak BRA expression had little effect on SOX2 levels,

however saturating Barbell concentrations (>10 nM) increased SOX2 expression (**Figure 4.2 a,b – *middle***). This likely reflects the antagonistic relationship between BRA and SOX2 and may suggest the emergence of ectoderm fate through Wnt downregulation, however additional genetic markers are needed to confirm this [40,41]. As our primary focus is understanding the Barbell's effectiveness at inducing mesoderm, we calculated the BRA-toSOX2 ratio of individual cells and discovered that a 1nM treatment is the strongest inducer of mesoderm (**Figure 4.2 a,b - *bottom***). Indeed, this complements our observations in HEK293T cells and highlights the Barbell's Wnt agonism across cell types.

To corroborate the immunofluorescence data, we monitored the levels of several genetic markers using qPCR. Barbell treatments (1nM) upregulated mesoderm markers *TBXT, EOMES, GSC, MIXL1,* and *HAND1* while also downregulating pluripotency markers *OCT4, SOX2,* and *NANOG* to a similar degree as CHIR (**Figure 4.2 c**).

The changes in cellular fate markers strongly suggest that the Barbell drives mesoderm differentiation, however we wanted to further demonstrate that Barbell-differentiated mesoderm undergoes the epithelial-to-mesenchymal transition (EMT) that is characteristic of gastrulation[42]. We plated hESCs on 500µm patterns and measured cellular outgrowth over 3 days of treatment as a proxy for EMT. By day 2, outgrowth spiked to 800-1000µm in both Barbell- and CHIR- treated colonies and receded by day 3 (**Figure 4.2 d**). Overall, Barbell-induced EMT mimics that of CHIR in both magnitude and time and confirms that The Barbell induces both the molecular markers and tissue-level phenotypes associated with Wnt-mediated mesoderm differentiation.

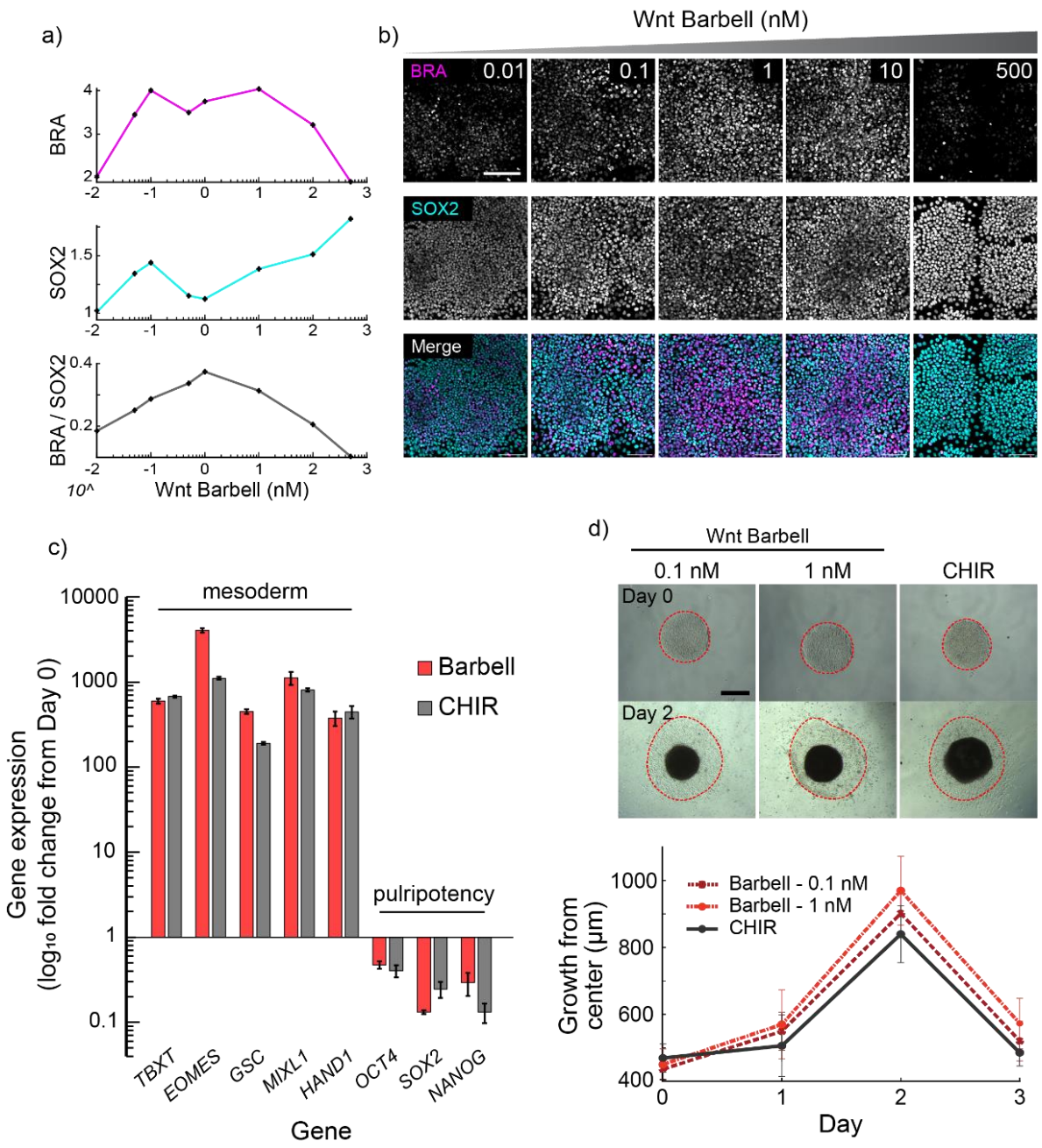

Figure 4.2 a) Immunofluorescence quantification of BRA and SOX2 expression following a 2-day differentiation with Wnt Barbell at indicated concentrations. Values are normalized to undifferentiated control (*top, middle rows*). Single cell ratios of BRA-to-SOX2 (*bottom row*). b) Representative images of BRA and SOX2 expression after 2-day differentiation. Scale bar = 100µm. c) qPCR results for mesoderm and pluripotency genetic markers. hESCs were differentiated to mesoderm using Wnt Barbell (*red, 1 nM*) or CHIR (*grey, 6 µM*) as the Wnt agonist. d) Representative images of hESC colonies during EMT. Red lines represent edge of cellular outgrowth. Scale bar = 500µm (*top*). Quantification of EMT outgrowth over 3 days of mesoderm differentiation using Wnt Barbell (*red, dark red*) or CHIR (*black*).

4.2.4 Barbell Supports Tissue-Specific Stem Cell Differentiations

The Wnt pathway is an attractive target for regenerative tissue therapies, and our demonstration of mesoderm induction from hESC populations solidifies the Barbell as a novel Wnt modulator for human stem cells. Wnt agonism has been shown to increase bone regrowth in vivo and promote the progression of mesenchymal stem cells toward osteogenic lineages through the stabilization of β-catenin[15,43]. Therefore, we reasoned that the Wnt Barbell will increase β-catenin levels in human mesenchymal stem cells (hMSCs) during osteogenic differentiations and lead to increased expression of osteo-specific markers compared to non-supplemented differentiation conditions (induction media). We supplemented osteogenic induction media (L-ascorbic acid, β-glycerophosphate, dexamethasone) (IM) with CHIR (1μM) or Barbell (1nM) and allowed hMSCs to differentiate for 14 days (**Figure 4.3 a**). Following the 14-day differentiation, Alizarin red staining showed no qualitative difference in mineral deposition across induction conditions, however all inductions conditions clearly induced mineral deposition compared to the basal media (BM) control (**Figure 4.3 b**). Closer inspection revealed that cellular β-catenin levels were upregulated in osteocytes differentiated with Barbell- or CHIR-supplemented media (**Figure 4.3 c**), and qPCR confirmed the upregulation of osteo-specific markers *ALP, Col1a1, RUNX2,* and *Osteocalcin* in these conditions (**Figure 4.3 d**). Taken together, this suggests Barbell-induced Wnt agonism may be a potential mechanism to increase efficiency of hMSC osteogenic differentiations.

Cardiomyocytes (CMs) can be derived from hESCs given the appropriate temporal activation of Wnt signaling, thus we were curious if our Barbell-derived mesoderm could be further specified into functional CMs. We plated hESCs on 500μm patterns and followed an

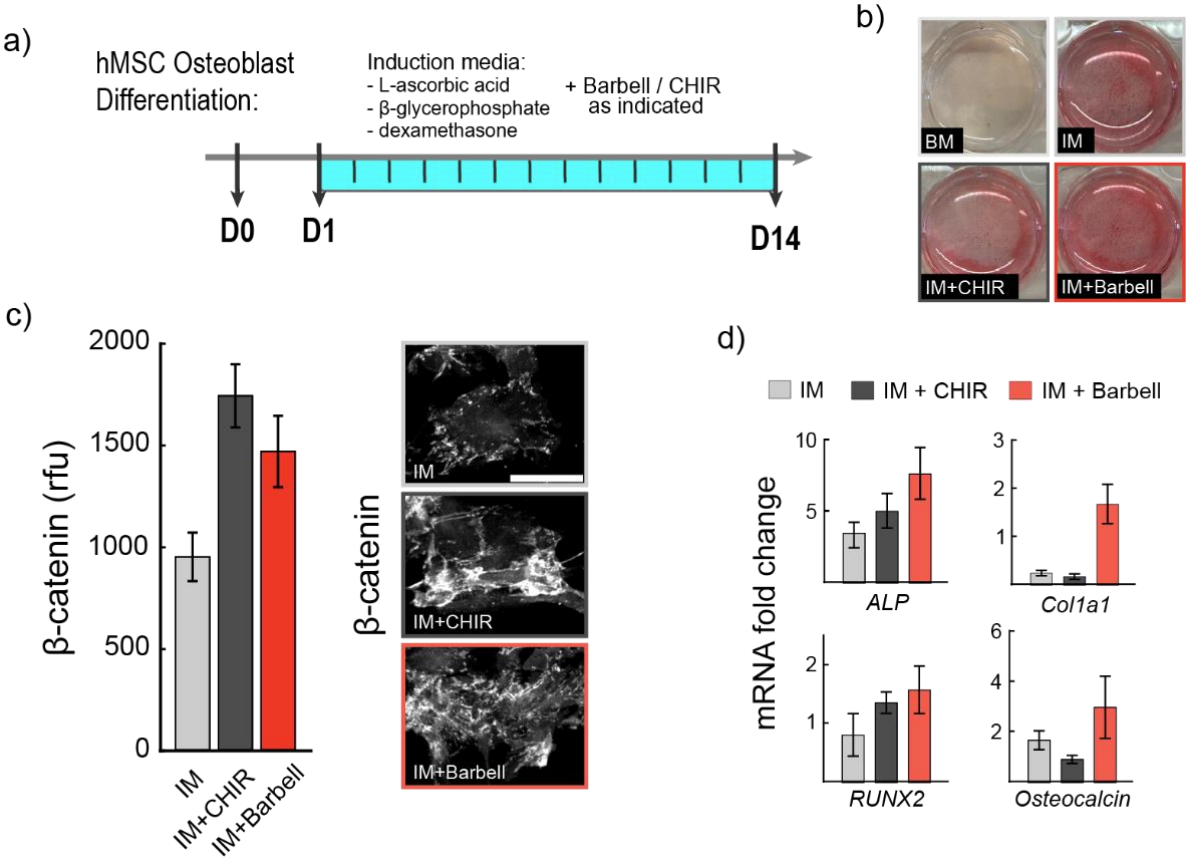

Figure 4.3 a) Differentiation protocol to generate hMSC-derived osteocytes. b) Calcium mineral deposition (Alizarin red stain) after 14 days of differentiation in indicated media condition. c) Cellular β-catenin levels on Day 14. d) qPCR results for osteo-specific markers *ALP*, *Col1a1*, *RUNX2*, *and Osteocalcin* on Day 14. Expression levels are normalized to Day 0 values.

established CM differentiation protocol, using 1 nM Wnt Barbell in place of the recommended Wnt agonist CHIR (**Figure 4.4 a**)[44]. By day 8, Barbell-differentiated colonies had robust expression of the cardiac-specific transcription factor Nkx2.5 and its localization at colony edges mimicked that of the CHIR control (**Figure 4.4 b**). Nkx2.5 expression remained elevated through day 15 at which point we used qPCR to confirm the expression of additional cardiac-specific markers. Indeed, Barbell-treated colonies strongly expressed several structural and regulatory genes associated with myocardium development, including *SERCA*, cardiac troponin T (*cTNT*), myosin heavy chains 6 and 7 (*MyH6/7*), and myosin light chain 2 (*MyL2*) (**Figure 4.4 c**).

We also noted several CM patterns spontaneously contracting, a hallmark of CM differentiation. To better understand the calcium handling of our Barbell-derived cardiac tissue we tracked the calcium kinetics of day 15 CMs using Rhod-4AM. The calcium transient frequency and shape of Barbell-derived CMs closely resembled that of the CHIR-derived tissue(**Figure 4.4 d**). Furthermore, the calcium transient time-to-peak and decay times (50% and 90%) were similar for both differentiation conditions (**Figure S4.3**), confirming Barbell-mediated differentiation is sufficient to produce functional embryonic stem cell-derived cardiac tissue.

Specific hallmarks of stem cell-derived CM maturation are still incompletely established[45], although the emergence of sarcomere banding is generally regarded as a shift toward maturity and observed roughly a month after the start of the differentiation process[46]. To confirm that Barbell-differentiated cardiac tissue demonstrates the ultrastructural organization indicative of myocyte maturation we compared the expression and localization of troponin I1 (TNNI1) of Barbell- and CHIR-derived CM patterns on Day 30 using an induced

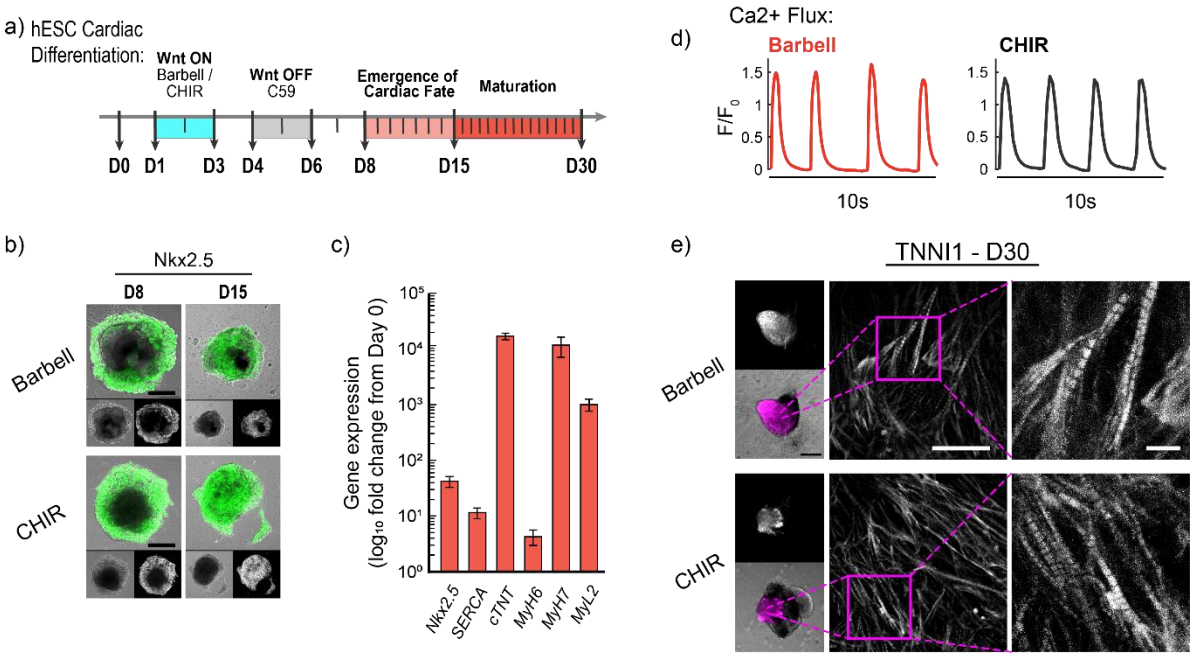

Figure 4.4 a) hESC cardiac differentiation protocol adapted from *Lian et al. 2012*. b) Expression of cardiac-specific transcription factor NKX2.5 at days 8 and 15 of differentiation. Scale bar = 250µm. c) qPCR results of cardiac-specific structural genes and transcription factors. Values are normalized to Day 0 expression levels and represented as fold change from Day 0. d) Calcium flux over 10 seconds in Barbell- and CHIR-derived cardiomyocyte patterns. e) TNNI1 expression in cardiac micropatterns at day 30 (*left*). Scale bar = 250µm. 100X images of TNNI1 alignment (*middle*) and zoomed representation of sarcomere banding (*right*). Scale bars = 20µm and 5µm.

pluripotent stem cell (iPSC) line with endogenously labeled TNNI1 (Allen cell line AICS-0037). We were pleased to not only see strong TNNI1expression in Barbell-treated colonies (**Figure 4.4 e - *left***), but also pronounced banding when imaged at high magnifications (**Figure 4.4 e - *right***). Thus, we can confidently conclude that CM differentiation with the Wnt Barbell results in cardiac tissue matching the established genetic, structural, and functional aspects of stem cell-derived cardiomyocytes.

4.3 – *Discussion*

The Wnt/β-catenin pathway is a pivotal regulator of cellular proliferation, stem cell differentiation, and tissue homeostasis, making it an attractive target for therapeutic regulation and tissue regeneration. Here we present a novel synthetic Wnt ligand, the Wnt Barbell, that functions by heterodimerizing Wnt coreceptors LRP6 and Fz for precisely controlled Wnt signaling. We use the Barbell to differentiate mesoderm from both embryonic and induced stem cells, and further highlight its broad applications for tissue engineering by improving osteoblast differentiations from hMSCs and deriving functional CMs from hESC and iPSC populations.

The inimitable biochemical nature of Wnt ligands[4,6], along with Wnt's crucial role in development and disease[10,20], has fueled a growing interest in synthetic approaches to precisely and specifically modulate Wnt signaling. The most widely used is a small molecule inhibitor of GSK-3 (CHIR), however several signaling cascades converge on GSK-3 so its inhibition influences numerous parallel pathways[47]. To more closely recapitulate natural pathway activation, groups have utilized bi-specific synthetic protein ligands that induce proximity of LRP6 and Fz on the cell surface to initiate signaling. The modular design of these synthetic

proteins has allowed researchers to address outstanding questions related to the role of Fz pleiotropy in tissue development and stoichiometric requirements of LRP6/Fz complexes to stimulate signaling[48]. Interestingly, the stoichiometric requirements for signaling vary across synthetic Wnt versions, such that bivalent heterodimerization may[28,29] or may not[27,30] be sufficient for signal induction, with other examples suggesting signal strength increases with increased valency[26]. While these inconsistencies are likely a result of geometric constraints within ligand-induced LRP6/Fz complexes, the growing family of synthetic Wnt agonists nonetheless offers an attractive approach for precisely modulating Wnt signaling due to their ease of production, superior stability, and modular nature.

Our Wnt Barbell leverages a bi-valent design composed of two compact and highly-specific binders of LRP6 and Fz, D07 and DRPB-7/8, allowing for the Wnt Barbell to be the first synthetic Wnt to be produced from bacterial expression systems. We demonstrate that Wnt activity can be tuned with Barbell concentration and that Barbell-induced signaling is subject to receptor-level regulation, unlike small molecule agonists with intracellular targets. When applied to human embryonic stem cells, the Barbell upregulates canonical mesoderm markers and induces EMT. While the majority of the mesoderm-indicative genes showed similar levels of upregulation in both Barbell and CHIR treatments, eomesodermin (*EOMES*) was expressed roughly 4x stronger in Barbell-derived mesoderm than its CHIR-derived counterpart (**Figure 4.2 c**). Controlled expression of *EOMES* revealed it induces Wnt signaling to form a self-sustaining signaling network during cardiac mesoderm induction that is essential for cardiac specification[49]. While the specific relationship between *EOMES* and Wnt signaling falls outside of the scope of this paper, the observed differences in expression level are likely an outcome of the different mechanisms used to activate the Wnt pathway. Indeed, we are

pursuing this observation by gathering a more complete representation of cellular responses to CHIR- and Barbell-induced Wnt signaling with bulk RNA-sequencing of mesoderm and cardiac tissues. Nonetheless, when used as a Wnt agonist in established differentiation protocols, the Barbell generates functional stem cell-derived cardiomyocytes and improves the efficiency of osteocyte differentiations. Moreover, the strong Wnt response elicited by the Barbell, in conjunction with our demonstrated applications of tissue-specific differentiations, supports the narrative that LRP6/Fz heterodimerization is sufficient for Wnt responses at the cellular and tissue levels.

In conclusion we present a novel Wnt agonist that can be easily produced from basic expression systems and serve as a potent and tunable Wnt pathway stimulant across cellular contexts. The Barbell acts as a simplified and streamlined addition to the expanding toolkit for synthetic Wnt modulation and tissue engineering. We envision the Wnt Barbell, and its future iterations, will be useful in further dissecting the regulatory role of Wnt signaling in stem cell biology and developing Wnt-based therapeutics.

4.4 – *Ongoing & Future Directions*

The Wnt Barbell is the first reported synthetic Wnt ligand to be produced in bacterial systems. Bacterial expression of recombinant proteins is far simpler, cheaper, and quicker than expression in eukaryotic systems, thus the Wnt Barbell is highly amenable to design alterations to enhance our understanding and control of the Wnt pathway. While the tissue-specific uses highlighted in Chapter 4.1-4.3 expand upon the number of approaches for synthetically controlling the Wnt pathway and demonstrate applications for Barbell-induced Wnt signaling, the Barbell can be further envisioned as a tailorable platform for engineering Wnt signaling.

The following sections highlight initial progress on novel “arms” of the Barbell platform. These sections explore how disordered domains affect the signaling capabilities of the Barbell and the design of a light-inducible Wnt Barbell.

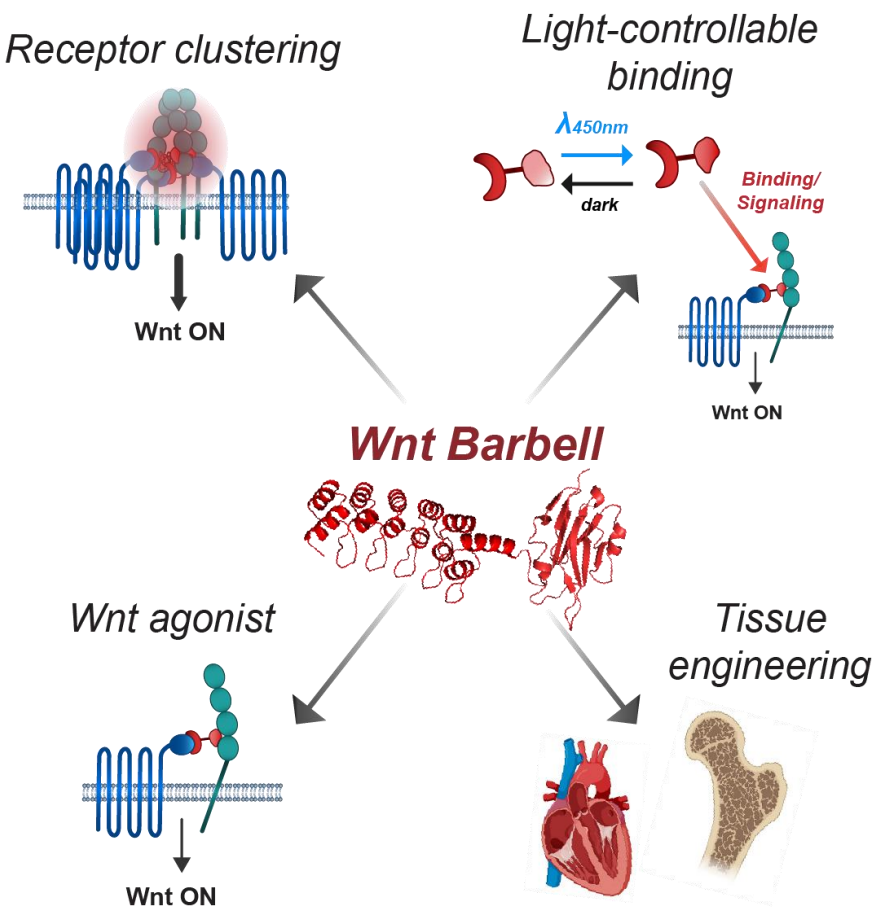

Figure 4.5 The Wnt Barbell's ability to stimulate Wnt activity across cell types, amenability to design perturbations, and simple expression system makes it an attractive platform for studying receptor-level Wnt signaling and engineering novel approaches for Wnt activation. Thus far, this chapter has confirmed the Barbell sufficiently activates Wnt signaling in a variety of cell types and can be used in tissue-specific differentiation protocols (*bottom*). Ongoing work is exploring how the addition low-complexity, condensate-forming domains to the Barbell influence Wnt pathway activity (*top right*) and engineering light-inducible binding of the Barbell to its target receptors (*top right*).

4.4.1 Disordered Domains Alter Signaling Potency

Our heterodimeric Barbell (GS Barbell) potently activated Wnt signaling across cell types, however an increase in receptor valency has been associated with an increase in signal potency for certain reported synthetic Wnt ligands [26,27,30], and the progression of heterodimeric signalosomes to higher-order oligomers has been proposed as a natural mechanism for Wnt signal potentiation[50]. While the exact relationship between receptor (LRP6/Fz) multimerization and signaling capability is incompletely understood, we were curious how altering the biophysical properties of the Wnt Barbell to promote receptor oligomerization, as opposed to heterodimerization, would change the Wnt response. Fused in sarcoma (FUS) domains are highly disordered sequences that undergo phase separation to form liquid-like droplets at physiological salt and pH conditions[51], thus the addition of FUS domains to the Wnt Barbell should drive higher-order receptor multimerization and further potentiate Wnt activity (**Figure 4.6 a**).

To make FUS Barbells, increasing lengths of the low complexity FUS domain (52, 114, and 214 amino acids) were added in place of the GS linker or at the C-terminus of the protein (**Figure 4.6 b**) and purified from the soluble fraction of bacterial lysates (**Figure S4.4 a**). As in Section 4.2.2, we treated HEK:bCat_miRFP-TF cells with FUS Barbells to track their Wnt activity. Following 24 hours of treatment, the miRFP translational reporter revealed stark differences in Wnt responses across different FUS Barbells. All FUS Barbells, *excluding* FUS-52, appeared to stimulate Wnt signaling over a wider concentration range than the GS Barbell, although the potency of the response was dependent on the location of FUS within the Barbell. Barbells with a FUS linker between D07 and DRPB-7/8 had significantly decreased signaling potency than those with the binding domains separated by the far shorter GS linker. However,

moving the FUS domain to the C-terminus of the construct (C-FUS) resulted in the highest Wnt activity, which occurred at a 10-fold higher concentration than that of the GS Barbell (**Figure 4.6 c,d**).

We believed the increased receptor proximity induced by Barbells with the short GS linker resulted in the higher Wnt activity, and that additional oligomerization driven by the FUS domain of the C-FUS Barbell further potentiated the signal. To observe the increased signalosome size, we treated cells with 10 nM GS or C-FUS Barbells for 15 minutes and stained for Frizzled-5 and Frizzled-7. Unfortunately, Fz appeared to be mostly internalized at this timepoint and the resolution of our microscope did not allow for the quantification of internalized puncta. Thus, we are unable to conclude that C-FUS Barbells elicit their potentiated Wnt response through receptor oligomerization (**Figure S4.4 b)**.

However, the staining did show Frizzled-5 on the membrane in CHIR and control (DMEM media only) conditions, although this seemed to represent only a small fraction of the total Fz (**Figure S4.4 b – *pink arrows*).** There was no noticeable membrane-bound Fz in either Barbell condition, suggesting that Barbell-induced signalosomes had already been internalized. Rapid internalization of Wnt signalosomes (10-120 minutes) is widely observed and believed to be a mechanism for positive and negative regulation of signal strenght[52,53]. We also noted the presence of large endosome-like structures (several hundred to 3000 nm in diameter) in Wnt-stimulated conditions (**Figure S4.4 b – *green arrows***); endosomes are believed to play a crucial role in Wnt signal maintenance by sequestering GSK3 to promote stabilization of β-catenin[52,54,55]. Interestingly, there were far more endosome-like structures in Barbell conditions (GS and C-FUS) than CHIR, possibly highlighting a mechanistic difference between receptor-level- and small molecule-based approaches for Wnt stimulation.

Indeed, ongoing work is focused on understanding differences in how heterodimer-inducing (GS Barbell) and oligomer-inducing (FUS) Barbells interact with receptors on the cell surface and how those interactions contribute to the Wnt response. Professor Rick Baker, at UNC Chapel Hill, is using mass photometry to understand how different Barbells influence signalosome stoichiometry. Surrena Pecchia (Wilson lab member) is using a proximity labeling approach to uncover the role of signalosome stoichiometry in dictating protein-protein interactions at both the receptor- and cytoplasmic- levels of Wnt signaling. Furthermore, immediate work is being done to visualize GS Barbell- and C-FUS Barbell- induced signalosomes using high-resolution microscopy.

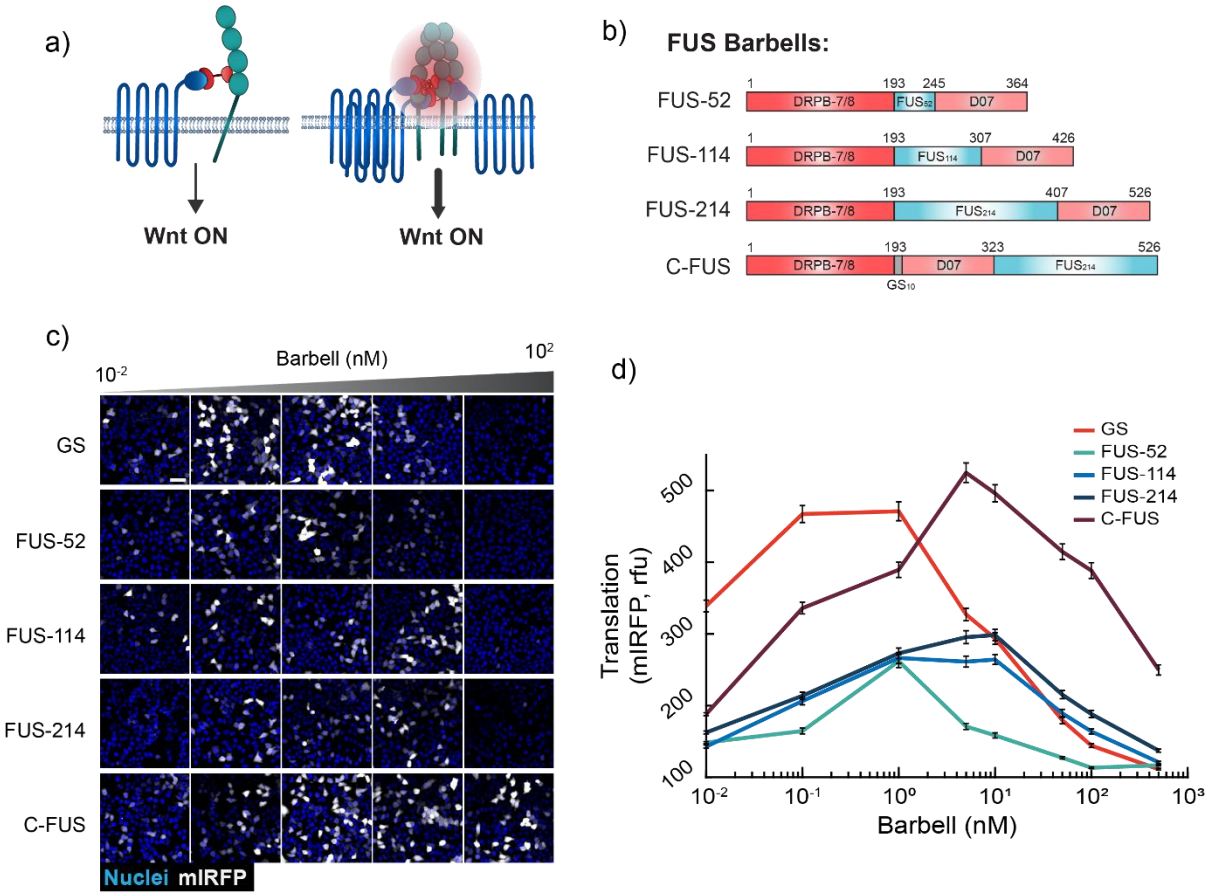

Figure 4.6 a) Schematic demonstrating hypothesis that receptor oligomerization further potentiates Wnt signaling. b) FUS Barbells. c) Representative images of Wnt translational response resulting from treatment with FUS Barbells. Scale bar = 50 µm. d) Quantification of translational response, shown as average mIRFP signal for *all* cells.

4.4.2 Light-responsive Barbell

Gradients and temporal pulses of Wnt activity across developing tissues result in concentration-dependent Wnt responses that induce differential gene expression to shape tissue patterns[56]. Optogenetic approaches for controlling Wnt activity, that allow for precise spatiotemporal pathway activation, have shed light on the role Wnt dynamics play in orchestrating these critical developmental processes[57,58], however the utilization of optogenetic control is traditionally limited to genetically modified cell types. We reasoned that a Wnt Barbell capable of reversibly binding LRP6 and Fz in a light-dependent fashion would allow for spatiotemporally defined Wnt signaling without genetically altering the cell type in use.

Previously published works demonstrated that nanobody binding can be light-controlled through the insertion of a photoswitchable light-oxygen-voltage (LOV) domain in solvent exposed loops[59]. LOV domains undergo conformational changes upon illumination, thus they are capable of allosterically altering complementarity-determining regions (CDRs) of nanobodies in a light-dependent fashion. We reasoned that a similar approach could be applied to the D07 nanobody, that serves as the LRP6 binder in the Wnt Barbell, to achieve light-dependent Wnt signaling.

To generate light-responsive Barbells (LOV Barbell) we used the published structure of D07 to identify surface-exposed loops as candidates for LOV-insertion[31]. G16, V65, and A76 were identified as potential insertion sides due to their location within the flexible surface-exposed loops flanking the β sheets of the nanobody's frame (**Figure 4.7 a,b)**. HEK:bCat_miRFP-TF cells were treated with purified LOV Barbells and illuminated (40s:20s ON:OFF, 450nm) or kept in the dark for 24 hours before measuring translational activity. The G16 and A76 insertions resulted in no Wnt response, irrespective of illumination conditions,

implying that the inserted LOV domain severely disrupted D07's interaction with LRP6. LOV insertion at V65 showed a slight increase in Wnt activity when illuminated, suggesting the LOV conformational change slightly increased the affinity of LOV-inserted D07 toward LRP6 (**Figure 4.7 c**).

Since LOV domains undergo their respective conformational changes on the order of seconds[60], the 40s:20s ON:OFF pulse used to screen the insertion sites may not have been optimal for persistent D07-LRP6 binding. An illumination screen using the V65-LOV Barbell revealed constant light induces the largest dynamic range of dark-to-light Wnt activity (**Figure 4.7 d**). Rspo-1, shown earlier to potentiate Barbell-mediated Wnt activity (**Figure 4.1 f**), expanded the dynamic range of the system by significantly increasing Wnt activity when illuminated, however also increased dark-state Wnt activity (**Figure 4.7 e**). This is likely a result of Rspo-1's stabilizing effect on surface-localized LRP6[61], nonetheless illumination resulted in a 9% increase in Wnt responsive cells.

Taken together, these experiments suggest LOV Barbells may be a promising approach for dynamic control of Wnt activity in genetically unmodified cell types. Further optimization of the LOV Barbells should be targeted at expanding the dynamic range of their responsiveness, either by improving lit-state activity or decreasing dark-state activity in the presence of Rspo-1. *Zhu et al, 2023* improved to dynamic range of a LOV-modified transcription factor by flanking the insertion with short (2-4 amino acid) to mediate conformational changes[62], indeed this approach may also prove effective in our D07 nanobody.

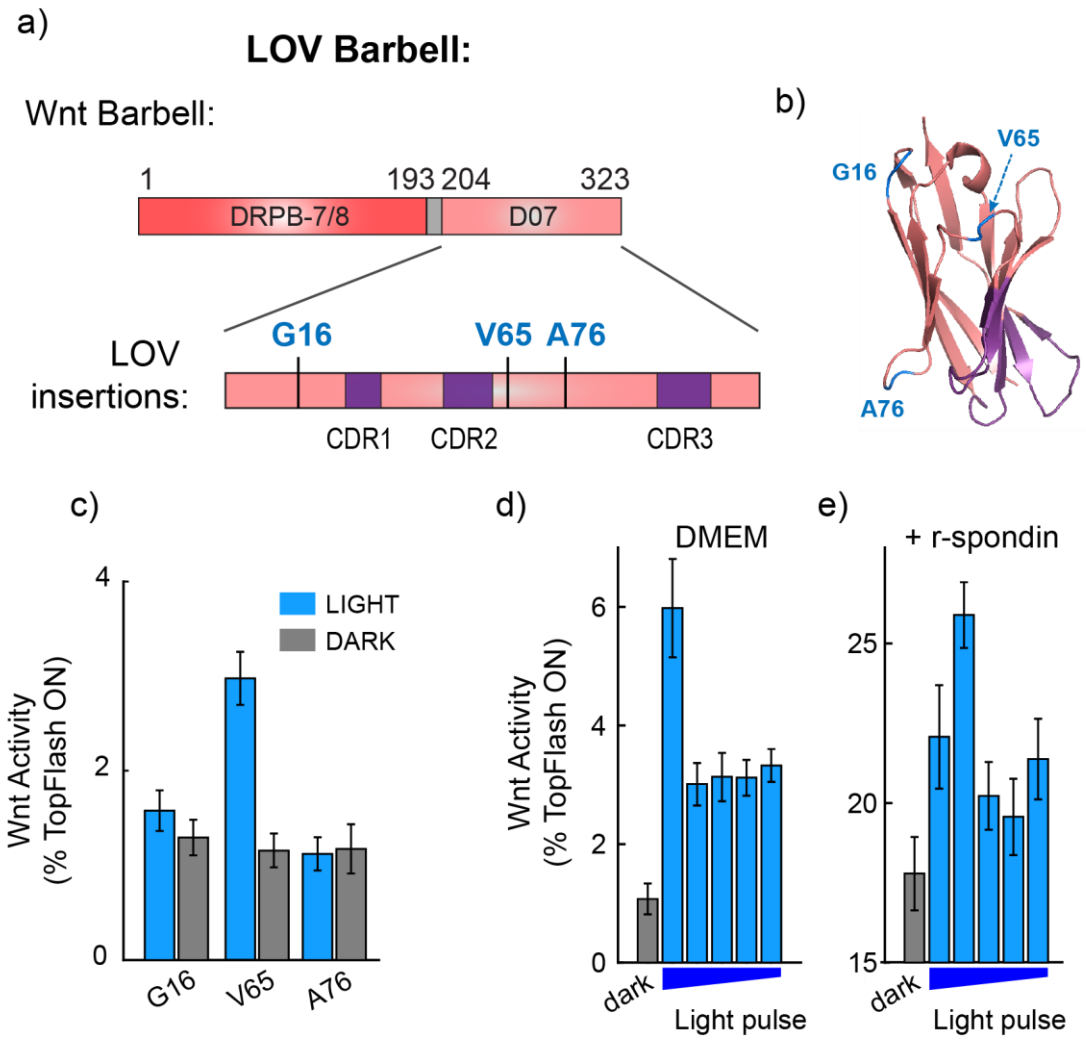

Figure 4.7 a) Location of LOV insertion sites within D07 and the Wnt Barbell. b) Structural representation of LOV insertion sites in surface-exposed loops of D07. c) Wnt activity of LOV Barbells following 24 hours of incubation in dark or light conditions. d) Effect of increasing illumination pulses on V65-LOV Barbell in normal media conditions and e) Rspo-1 supplemented conditions (10nM). Pulses (seconds, ON:OFF): constant, 50:10, 40:20, 30:30, 20:40.

4.5 – *Materials & Methods*

Plasmid construction, protein expression, and purification: All constructs for purification were cloned into a pBAD expression vector, containing a C-terminal HIS tag separated by a GGSGG linker, with Gibson Assembly. Sequences for D07 and DRPB-7/8 were obtained from published works[31,32] and purchased as gBlocks (Integrated DNA Technologies). Positively sequenced expression vectors were transformed into T7 Express E. coli (NEB) and stored as glycerol stocks for expressions. Amino acid sequences can be found in **Table S4.1**.

Proteins were expressed in 100mL cultures of Terrific Broth (TB, IBI Scientific IB49140) for 4-6 hours of induction. Briefly, overnight cultures grown in TB (+Amp) were used to inoculate 100mL of media to OD_{600} 0.01, and grown at 37°C while shaking. At OD_{600} 0.2-0.4, cultures were induced with 3.33mM arabinose and grown at room temperature for 4-6 hours while shaking. After expression, cultures were pelleted and stored at -80°C until purification.

To purify proteins, frozen pellets were thawed and resuspended in Base Buffer (12.5mM Tris-Cl, 300mM NaCl, 2.5mM imidazole, 1mM MgOAc, 0.05% Tween-20, pH 8.1. **500mM NaCl was used for FUS-containing constructs) supplemented with 0.5mg/mL lysozyme (Sigma, L6876) and protease inhibitor cocktail (Sigma, P8849) and incubated for 30 minutes on ice. Solutions were then sonicated (15 seconds ON : 45 second OFF) for a total of 3 minutes and clarified by centrifuging (7000g, 30 minutes). Ni-IMAC resin (Thermo, A50584) was added to the soluble fraction and collected resin was washed 3 times (Base Buffer + 25mM imidazole) before eluting proteins (Base Buffer + 250mM imidazole). Elutions were concentrated with Pierce Concentrators (Thermo, 88513), diluted to 10µM with Base Buffer (+ 5% glycerol), aliquoted, and frozen for future use.

Mass photometry: All measurements were taken on a Refeyn One Mass Photometer with AcquireMP software and analyzed using DiscoverMP software (all from Refeyn Ltd, Oxford, UK) according to previously established protocols. Briefly, imaging coverslips were bath sonicated in 50% isopropanol for 15 minutes and subsequently in ultra-pure H_2O for 5 minutes. Coverslips were dried using a stream of filtered air and imaging wells were made by applying adhesive four-well gaskets (Thor Labs). Prior to imaging, 10 μL of binding buffer was added to the imaging well to determine the imaging plane using an internal autofocusing system. 10 μL of sample was added to the imaging buffer, resulting in a final volume of 20 μL and a sample concentration between 5-40 nM. Dilution factors were determined empirically for each sample to ensure that landing rates and total signal were within manufacturers specifications. Measurements were acquired for 1 minute at a frame rate of 100 fps. All samples were in a buffer containing 20 mM HEPES, pH 7.6, 100 mM NaCl, 1 mM DTT. For runs containing binding partners, proteins were mixed at a 1:1 molar ratio and allowed to equilibrate for at least 30 minutes at room temperature before data collection.

HEK cell culture: Human 293T cells were cultured at 37°C and 5% CO_2 in Dulbecco's Modified Eagle Medium supplemented with 10% fetal bovine serum (Atlas Biologicals, F-0500-D) and 1% penicillin-streptomycin. The HEK:bCat_miRFP-TF cell line was generated from a modified version Addgene plasmid #12456[63]. Details on its construction can be found in *Lach et al. 2022*[64]. To test Barbell-induced responses, cells were plated on glass culture plates (Cellvis #P96-1.5H-N) coated with bovine fibronectin (Sigma #F1141) and allowed to adhere overnight. The following day, cells were treated with Barbell-supplemented media, at indicated concentrations, and cultured for 24 hours before monitoring responses.

For experiments using Dkk1 (R&D Systems, #BT54391CF) and Rspo-1 (PeproTech, #120-38), Barbell-supplemented media was additionally supplemented with 100ng/mL of Dkk1 or 10nM Rspo-1. Responses were monitored after 24 hours.

Protein structure schematics: Protein structures for the D07-LRP6 and DRPB-Fz-CRD interactions were found on RCSB PDB (6NDZ and 6H16). The structure for the Wnt Barbell was generated using RoseTTAfold. The D07 and DRPB domains of the Wnt Barbell were aligned with their corresponding structures in the respective PDB files using the 'Align' function in Pymol.

Micropatterning: For all micropatterning experiments PDMS stamps with circular 0.5 mm diameter features were used and fabricated according to *Karzbrun et. al. 2021*[65]. Micropattern formation was carried out by first incubating the PDMS stamps with 1% hESC qualified Matrigel® (Corning) in DMEM/F12, (Gibco) overnight at 4°C. Followed by stamping the PDMS stamps onto 12-well #1.5 plastic like glass cell culture plates (Cellvis) using a costume made stamp holder.

Mesoderm and cardiomyocyte differentiation: For mesoderm and cardiac differentiations, approximately 0.3×10^6 H9 NKX2.5–eGFP, H9 Wild Type, or IPSC TNNT1-eGFP cells were seeded per well of a micropatterned well in 0.5 ml mTeSR plus medium containing 10 µM Y-27632 (StemCell technologies) on D-2 (mesoderm differentiation for immunofluorescence was done on non-patterned Matrigel treated surfaces of a 96-well plate [Cellvis #P96-1.5H-N]). Medium was exchanged on D-1 with mTeSR plus + P/S. Differentiation of cells was

induced on D0 using either CHIR99021 at 6 µM or Wnt Barbell at 10, 1 or 0.1 nM in 2 ml RPMI + B27-insulin + P/S. After 48 h (D2) the experiment was either stopped and further analyzed for mesoderm differentiation or continued for cardiac differentiation. If continued the medium was exchanged by 2 ml RPMI + B27-insulin + P/S. On D3, C59 was added at 2 µM in 2 ml RPMI + B27-insulin + P/S. for 48 h. On D5, the medium was exchanged by 2 ml RPMI + B27-insulin + P/S. From D7 onwards, cells were kept in 2 ml RPMI + B27+insulin + P/S per well and the media was exchanged every other day.

Immunofluorescence: Cells were fixed with PFA (4%, 25 minutes at 4°C) and permeabilized with glacial ethanol for 90 seconds, then blocked with 3% BSA in PBST for 45 minutes at room temperature. Primary antibody incubations were done overnight at 4°C in PBST+ 3% BSA. Primary antibodies: Rabbit α-SOX2 (Cell Signaling Technology, #3579). Goat α-Brachyury (R&D Systems, #AF2085) Secondary incubations (PBST+ 3% BSA, +DAPI) were done for 30 minutes at room temperature and thoroughly rinsed before imaging. Secondary antibodies: Alexa Fluor 633 α-goat (Invitrogen, #A21070). Alexa Fluor 488 α-rabbit (Invitrogen, #A21206).

EMT quantification: For the EMT analysis Nkx2.5 cells (~0.3 × 10^6/12xWell) were seeded on 0.5 mm circular micropatterns in 12x12-wells #1.5 plastic like glass cell culture plate (Cellvis) and cultured as described previously. At D0 of differentiation 10 representative micropatterns per condition were selected and imaged daily using olympus ax70 microscope equipped with an Infinity2 camera at 4x magnification. Images were further analyzed using a custom Matlab script (EMT_analyzer_v4, R2022b) which can be found on Github

(https://github.com/TerDiv4/WNT-Barbell-Paper). Three biological replicates with 10 technical replicates per condition were used for the full analysis.

Calcium imaging: For calcium imaging, the Rhod-4 Calcium Assay Kit (Abcam) was used. Rhod-4 dye-loading solution was prepared according to the manufacturer's instructions. Cell cultures were incubated in Rhod-4 dye-loading solution in RPMI + B27+insulin + P/S for 20min in standard environments consisting of 5% carbon dioxide at 37°C. Afterwards, the cell cultures were washed 3x5 min with RPMI + B27+insulin + P/S and incubated for 45 min. The calcium flux was imaged using a Zeiss Axio Observer 7 inverted microscope equipped with a high speed/resolution camera (Photometrics Prime 95b). Images were further measured in FIJI using hand drawn ROIs and analyzed with custom Matlab scripts.

High magnification TNNI1 imaging: High magnification fluorescence imaging of whole-mount immunostained samples and was carried out using Leica SP8 confocal microscope using 100x oil immersion objective.

RNA extraction and quantitative RT-PCR (qPCR): RNA extraction and purification was done with the RNeasy mini kit (Qiagen, #74104) according to manufacturer's instructions. Reverse transcription was performed with 300ng of RNA with the High Capacity RNA-to-cDNA kit (Invitrogen, #4388950) per manufacturer's instructions. Quantitative RT-PCR (qPCR) was performed using PowerUp™ SYBR™ Green Master Mix (Applied Biosystems). At least three biological replicates and two technical replicates per sample per gene were performed. Technical replicate cycle threshold (Ct) values were averaged and normalized to glycerol

phosphate dehydrogenase (GAPHD)(ΔCt). Primer sequences were obtained from PrimerBank[66] and can be found in **Table 4.2**.

Osteocyte differentiations: Human mesenchymal stem cells (hMSCs) isolated from adult bone marrow were purchased from Millipore Sigma (#SCC034) and expanded to passage 4 (P4) in low-glucose DMEM (Gibco, #11885092) supplemented with 20% FBS 9Sigma F2442) and 1% P/S (Gibco, #15140148). P4 hMSCs were seeded onto 0.1% gelatin-coated well plates on Day 0 at a density of $3x10^3$ cells/cm^2 and allowed to adhere for 24 hours in basal media. Osteogenic differentiation was induced on Day 1 using 50 µg/mL L-ascorbic acid, 10 mM β-glycerophosphate, and 0.1 µM Dexamethasone, in addition to 1 µM CHIR or 1 nM Barbell as indicated. Induction media was changed every other day for 14 days prior to fixation or RNA extraction.

Cells used for immunostaining were fixed in 4% PFA for 25 minutes at 4C, permeabilized with 0.1% Triton X-100 for 15 minutes, and then blocked with 3% BSA in PBST for 45 minutes at room temperature. Primary antibodies were incubated overnight at 4°C in PBST+ 3% BSA, then rinsed three times with PBS. Primary antibodies: (Beta-catenin Ab from your lab from the 5 uL Rabbit IgG aliquots). Secondary incubations (PBST+ 3% BSA, +DAPI) were performed for 60 minutes at room temperature and rinsed three times in PBS prior to imaging. Secondary antibodies: Alexa Fluor 647 α-rabbit (Invitrogen, # A27040). Cells used for Alizarin Red staining were rinsed three times with deionized water after fixation and incubated in staining solution (Millipore, A5533) for 30 minutes prior to imaging.

4.6 – *Acknowledgements & References*

The Wnt Barbell project has grown to have several exciting directions thanks to the interest and expertise from my colleagues, collaborators, and undergraduate students. First off, I would like to thank Markus Merk and Professor Sebastian Streichan for their enthusiasm about the Wnt Barbell project and their expertise in CM differentiations and CM biology. Markus' expertise was essential in characterizing mesoderm and CM differentiations. I would also like to thank Ian Tayler for his willingness to explore the Barbell's effect on osteogenic differentiations.

Furthermore, the endless hours contributed by undergraduate students Jose Nunez, Eric Hao, July Wu, and Kristy Le to all facets of the project were essential for its progress, and their collective curiosity led to many of the innovative Barbell designs (some of which are not included in this dissertation). Finally, I would like to thank Professor Rick Baker and the members of his lab at UNC Chapel Hill for their help in observing Barbell-receptor interactions with mass photometry.

1. Niehrs, C. The role of Xenopus developmental biology in unraveling Wnt signalling and antero-posterior axis formation. *Dev Biol* **482**, 1–6 (2022).
2. Rim, E. Y., Clevers, H. & Nusse, R. The Wnt Pathway: From Signaling Mechanisms to Synthetic Modulators. (2022) doi:10.1146/annurev-biochem-040320.
3. MacDonald, B. T. & He, X. Frizzled and LRP5/6 Receptors for Wnt/b-Catenin Signaling. *Cold Spring Harb Perspect Biol* (2012) doi:10.1101/cshperspect.a007880.
4. Yu, J. & Virshup, D. M. Functional regulation of Wnt protein through post-translational modifications. *Biochem Soc Trans* **50**, 1797–1808 (2022).

5. Kikuchi, A., Yamamoto, H., Sato, A. & Matsumoto, S. New Insights into the Mechanism of Wnt Signaling Pathway Activation. *Int Rev Cell Mol Biol* **291**, 21–71 (2011).

6. Mikels, A. J. & Nusse, R. Wnts as ligands: processing, secretion and reception. *Oncogene* 7461–7468 (2006) doi:10.1038/sj.onc.1210053.

7. Niehrs, C. The complex world of WNT receptor signalling. *Nature Publishing Group* **13**, 767 (2012).

8. Nelson, A. L. *et al.* Therapeutic approaches to activate the canonical Wnt pathway for bone regeneration. *J Tissue Eng Regen Med* 16 (2022) doi:10.1002/term.3349.

9. Jung, Y. S. & Park, J. Il. Wnt signaling in cancer: therapeutic targeting of Wnt signaling beyond β-catenin and the destruction complex. *Experimental & Molecular Medicine 2020 52:2* **52**, 183–191 (2020).

10. Clevers, H. & Nusse, R. Wnt/β-Catenin Signaling and Disease. *Cell* **149**, 1192–1205 (2012).

11. Jeong, W. & Jho, E. H. Regulation of the Low-Density Lipoprotein Receptor-Related Protein LRP6 and Its Association With Disease: Wnt/β-Catenin Signaling and Beyond. *Front Cell Dev Biol* **9**, 2559 (2021).

12. Zhao, H. *et al.* Wnt signaling in colorectal cancer: pathogenic role and therapeutic target. *Mol Cancer* **21**, 144 (2022).

13. Canalis, E. Wnt signalling in osteoporosis: mechanisms and novel therapeutic approaches. *Nature Reviews Endocrinology 2013 9:10* **9**, 575–583 (2013).

14. Lin, X., Meng, X. & Lin, J. The possible role of Wnt/β-catenin signalling in vitiligo treatment. *Journal of the European Academy of Dermatology and Venereology* **37**, 2208–2221 (2023).

15. Fowler, T. W. *et al.* Development of selective bispecific Wnt mimetics for bone loss and repair. *Nat Commun* (2021) doi:10.1038/s41467-021-23374-8.

16. Walter, R. J. *et al.* Wnt signaling is boosted during intestinal regeneration by a CD44-positive feedback loop. *Cell Death Dis* (2022) doi:10.1038/s41419-022-04607-0.

17. Whyte, J. L. *et al.* Augmenting Endogenous Wnt Signaling Improves Skin Wound Healing. *PLoS One* **8**, e76883 (2013).

18. Kuncewitch, M. *et al.* Wnt agonist decreases tissue damage and improves renal function after ischemia-reperfusion. *Shock* **43**, 268–275 (2015).

19. Law, S. M. & Zheng, J. J. Premise and peril of Wnt signaling activation through GSK-3b inhibition. *iScience* (2022) doi:10.1016/j.isci.

20. Bonnet, C., Brahmbhatt, A., Deng, S. X. & Zheng, J. J. Wnt signaling activation: targets and therapeutic opportunities for stem cell therapy and regenerative medicine. *RSC Chem Biol* **2**, 1144–1157 (2021).

21. Eldar-Finkelman, H. & Krebs, E. G. Phosphorylation of insulin receptor substrate 1 by glycogen synthase kinase 3 impairs insulin action. *Proc Natl Acad Sci U S A* **94**, 9660–9664 (1997).

22. Hermida, M. A., Dinesh Kumar, J. & Leslie, N. R. GSK3 and its interactions with the PI3K/AKT/mTOR signalling network. (2017) doi:10.1016/j.jbior.2017.06.003.

23. Trnski, D. *et al.* GSK3β and Gli3 play a role in activation of Hedgehog-Gli pathway in human colon cancer - Targeting GSK3β downregulates the signaling pathway and

reduces cell proliferation. *Biochim Biophys Acta Mol Basis Dis* **1852**, 2574–2584 (2015).

24. Bugaj, L. J., Choksi, A. T., Mesuda, C. K., Kane, R. S. & Schaffer, D. V. Optogenetic protein clustering and signaling activation in mammalian cells. *Nat Methods* **10**, 249–252 (2013).

25. Shahi, P. *et al.* Activation of Wnt signaling by chemically induced dimerization of LRP5 disrupts cellular homeostasis. *PLoS One* **7**, 30814 (2012).

26. Mukherjee, A. *et al.* One-pot synthesis of heterodimeric agonists that activate the canonical Wnt signaling pathway. *Chemical Communications* **56**, 3685–3688 (2020).

27. Tao, Y. *et al.* Tailored tetravalent antibodies potently and specifically activate wnt/frizzled pathways in cells, organoids and mice. *Elife* **8**, 1–16 (2019).

28. Miao, Y. *et al.* Next-Generation Surrogate Wnts Support Organoid Growth and Deconvolute Frizzled Pleiotropy In Vivo. *Cell Stem Cell* **27**, 840-851.e6 (2020).

29. Janda, C. Y. *et al.* Surrogate Wnt agonists that phenocopy canonical Wnt and β-catenin signalling. *Nature 2017 545:7653* **545**, 234–237 (2017).

30. Chen, H. *et al.* Development of Potent, Selective Surrogate WNT Molecules and Their Application in Defining Frizzled Requirements. *Cell Chem Biol* **27**, 598-609.e4 (2020).

31. Fenderico, N. *et al.* Anti-LRP5/6 VHHs promote differentiation of Wnt-hypersensitive intestinal stem cells. *Nat Commun* (2019) doi:10.1038/s41467-018-08172-z.

32. Dang, L. T. *et al.* Receptor subtype discrimination using extensive shape complementary designed interfaces. *Nat Struct Mol Biol* **26**, 407 (2019).

33. Chu, H. Y. *et al.* Dickkopf-1: A Promising Target for Cancer Immunotherapy. *Front Immunol* **12**, (2021).

34. Ahn, V. E. *et al.* Structural basis of Wnt signaling inhibition by Dickkopf binding to LRP5/6. *Dev Cell* **21**, 862–873 (2011).

35. Dann, C. E. *et al.* Insights into Wnt binding and signalling from the structures of two Frizzled cysteine-rich domains. *Nature 2001 412:6842* **412**, 86–90 (2001).

36. Hirai, H., Matoba, K., Mihara, E., Arimori, T. & Takagi, J. Crystal structure of a mammalian Wnt-frizzled complex. *Nat Struct Mol Biol* **26**, 372–379 (2019).

37. Ren, Q., Chen, J. & Liu, Y. LRP5 and LRP6 in Wnt Signaling: Similarity and Divergence. *Front Cell Dev Biol* **9**, 670960 (2021).

38. Kalluri, R. & Weinberg, R. A. The basics of epithelial-mesenchymal transition. *J Clin Invest* **119**, 1420–1428 (2009).

39. Romanos, M. *et al.* Cell-to-cell heterogeneity in sox2 and bra expression guides progenitor motility and destiny. *Elife* **10**, (2021).

40. Koch, F. *et al.* Antagonistic Activities of Sox2 and Brachyury Control the Fate Choice of Neuro-Mesodermal Progenitors. *Dev Cell* **42**, 514–526 (2017).

41. Osteil, P. *et al.* Dynamics of wnt activity on the acquisition of ectoderm potency in epiblast stem cells. *Development (Cambridge)* **146**, (2019).

42. Acloque, H., Adams, M. S., Fishwick, K., Bronner-Fraser, M. & Nieto, M. A. Epithelial-mesenchymal transitions: the importance of changing cell state in development and disease. *J Clin Invest* **119**, 1438 (2009).

43. Liu, X. *et al.* Wnt signaling in bone formation and its therapeutic potential for bone diseases. *Ther Adv Musculoskelet Dis* **5**, 13 (2013).

44. Lian, X. *et al.* Directed cardiomyocyte differentiation from human pluripotent stem cells by modulating Wnt/β-catenin signaling under fully defined conditions. *Nature Protocols 2013 8:1* **8**, 162–175 (2012).

45. Hong, Y. *et al.* Engineering the maturation of stem cell-derived cardiomyocytes. *Front Bioeng Biotechnol* **11**, (2023).

46. Lundy, S. D., Zhu, W. Z., Regnier, M. & Laflamme, M. A. Structural and Functional Maturation of Cardiomyocytes Derived from Human Pluripotent Stem Cells. *Stem Cells Dev* **22**, 1991 (2013).

47. Cormier, K. W., Larsen, B., Gingras, A. C. & Woodgett, J. R. Interactomes of Glycogen Synthase Kinase-3 Isoforms. *J Proteome Res* **22**, 977–989 (2023).

48. Tsutsumi, N. *et al.* Structure of human frizzled5 by fiducial-assisted cryo-em supports a heterodimeric mechanism of canonical wnt signaling. *Elife* **9**, 1–20 (2020).

49. Pfeiffer, M. J. *et al.* Cardiogenic programming of human pluripotent stem cells by dose-controlled activation of EOMES. *Nat Commun* **9**, (2018).

50. Gerlach, J. P. *et al.* TMEM59 potentiates Wnt signaling by promoting signalosome formation. *Proc Natl Acad Sci U S A* **115**, E3996–E4005 (2018).

51. Kato, M. & McKnight, S. L. The low-complexity domain of the FUS RNA binding protein self-assembles via the mutually exclusive use of two distinct cross-β cores. *Proc Natl Acad Sci U S A* **118**, e2114412118 (2021).

52. Colozza, G. & Koo, B. K. Wnt/β-catenin signaling: Structure, assembly and endocytosis of the signalosome. *Dev Growth Differ* **63**, 199–218 (2021).

53. Brunt, L. & Scholpp, · Steffen. The function of endocytosis in Wnt signaling. *Cell. Mol. Life Sci* **75**, 785–795 (2018).

54. Dobrowolski, R. & De Robertis, E. M. Endocytic control of growth factor signalling: multivesicular bodies as signalling organelles. *Nature Reviews Molecular Cell Biology 2011 13:1* **13**, 53–60 (2011).

55. Taelman, V. F. *et al.* Wnt Signaling Requires Sequestration of Glycogen Synthase Kinase 3 inside Multivesicular Endosomes. *Cell* **143**, 1136–1148 (2010).

56. Mehta, S., Hingole, S. & Chaudhary, V. The Emerging Mechanisms of Wnt Secretion and Signaling in Development. *Front Cell Dev Biol* **9**, 714746 (2021).

57. Krishnamurthy, V. V., Hwang, H., Fu, J., Yang, J. & Zhang, K. Optogenetic Control of the Canonical Wnt Signaling Pathway During Xenopus laevis Embryonic Development. *J Mol Biol* **433**, 167050 (2021).

58. Repina, N. A. *et al.* Optogenetic control of Wnt signaling models cell-intrinsic embryogenic patterning using 2D human pluripotent stem cell culture. *Development* **150**, (2023).

59. Gil, A. A. *et al.* Optogenetic control of protein binding using light-switchable nanobodies. *Nature Communications 2020 11:1* **11**, 1–12 (2020).

60. Nash, A. I. *et al.* Structural basis of photosensitivity in a bacterial light-oxygen-voltage/helix-turn-helix (LOV-HTH) DNA-binding protein. *Proceedings of the National Academy of Sciences* **108**, 9499–9454 (2011).

61. Binnerts, M. E. *et al.* R-Spondin1 regulates Wnt signaling by inhibiting internalization of LRP6. *Proc Natl Acad Sci U S A* **104**, 14700–14705 (2007).

62. Zhu, L., McNamara, H. M. & Toettcher, J. E. Light-switchable transcription factors obtained by direct screening in mammalian cells. *Nature Communications 2023 14:1* **14**, 1–16 (2023).

63. Veeman, M. T., Slusarski, D. C., Kaykas, A., Louie, S. H. & Moon, R. T. Zebrafish prickle, a modulator of noncanonical Wnt/Fz signaling, regulates gastrulation movements. *Curr Biol* **13**, 680–685 (2003).

64. Lach, R. S. *et al.* Nucleation of the destruction complex on the centrosome accelerates degradation of β-catenin and regulates Wnt signal transmission. *Proc Natl Acad Sci U S A* **119**, e2204688119 (2022).

65. Karzbrun, E. *et al.* Human neural tube morphogenesis in vitro by geometric constraints. *Nature* **599**, 268–272 (2021).

66. Wang, X., Spandidos, A., Wang, H. & Seed, B. PrimerBank: a PCR primer database for quantitative gene expression analysis, 2012 update. *Nucleic Acids Res* **40**, (2012).

4.7 – *Supplementary Information*

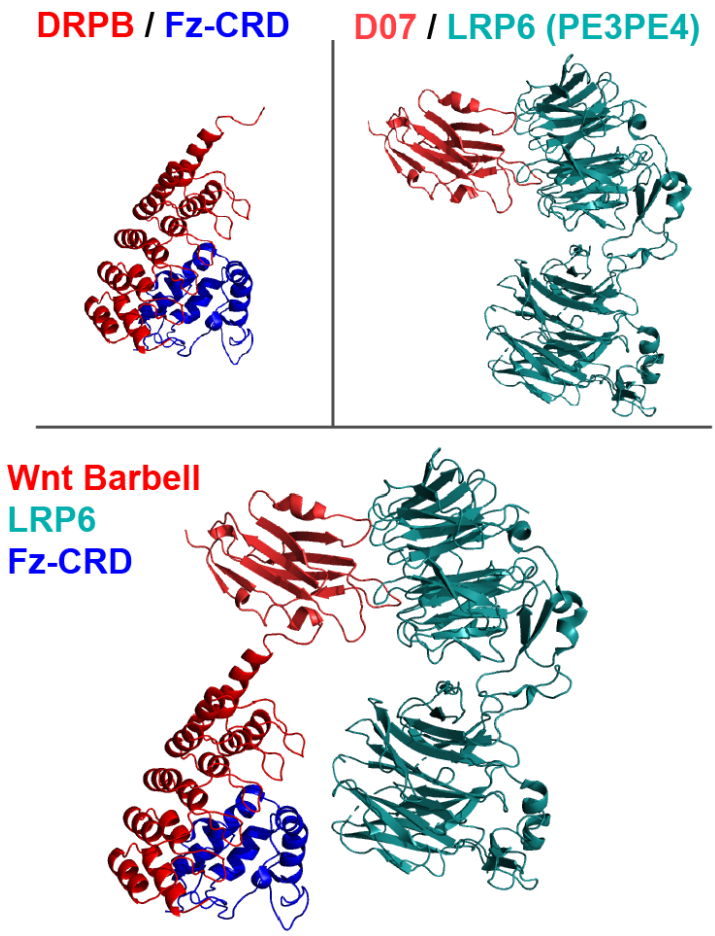

Figure S4.1 Binding complexes of DRPB:Fz-CRD (PDB_6NDZ, *top left*) and D07:LRP6 (PDB_6H16, *top right*). *Bottom*) Wnt Barbell in complex with Fz-CRD and LRP6. Wnt Barbell structure was predicted with RoseTTAFold. D07 and DRPB domains of the predicted Barbell structure were aligned with matching structures in respective PDB files.

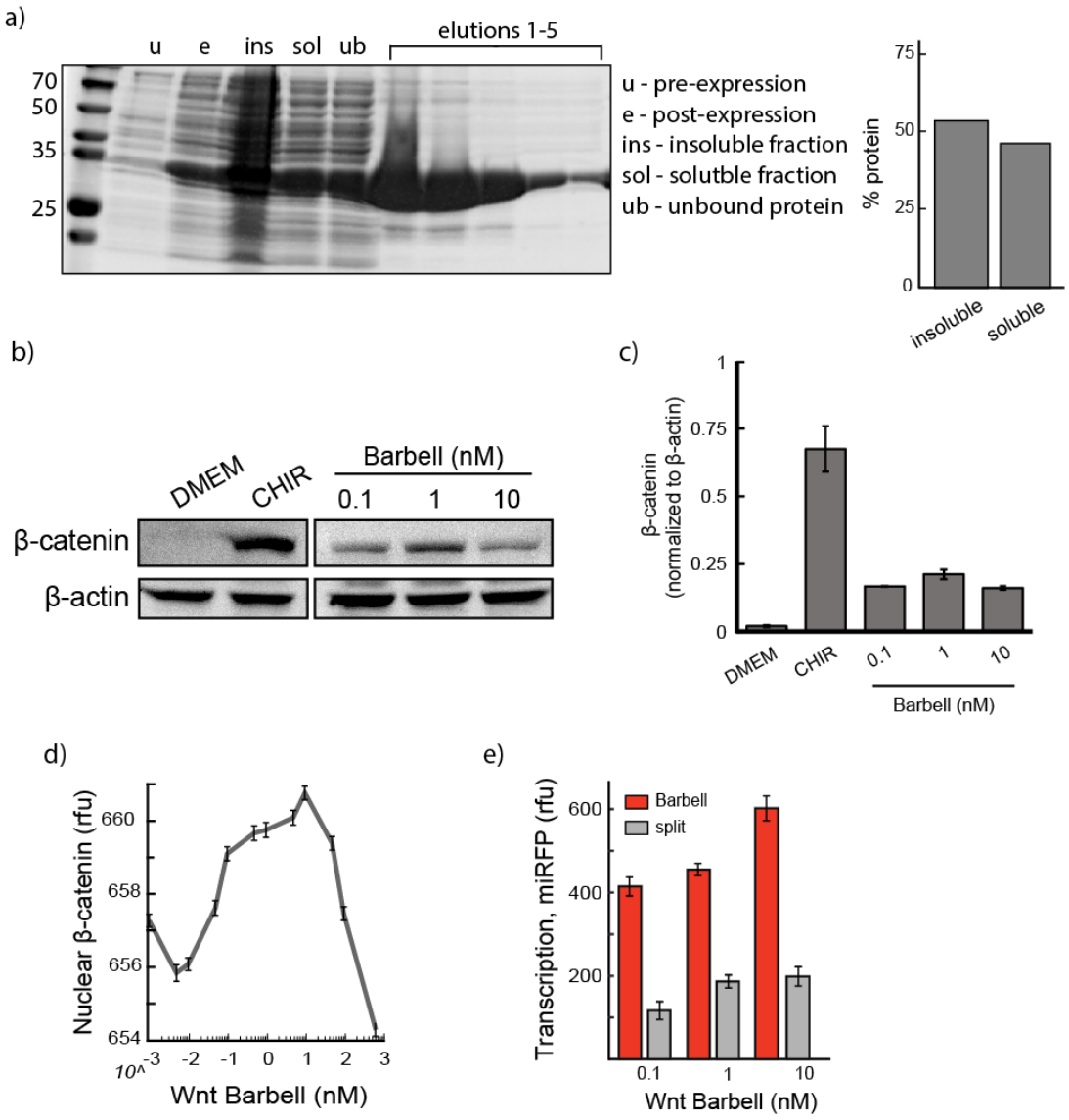

Figure S4.2 a) SDS-PAGE analysis of Wnt Barbell purification. Elutions 3-5 were saved for concentration and use in experiments. Bar chart on right depicts relative Barbell levels in insoluble and soluble fractions of bacterial lysate. b) Western blot showing β-catenin accumulation in wild type HEK293T cells after 24 hours of Barbell treatment. c) Quantification of β-catenin accumulation from Western blots (n=4). Levels are normalized to β-actin loading control. d) Fluorescence quantification of nuclear β-catenin after 24 hours of Barbell treatment (representative images in **Figure 4.1 d**). e) Wnt responses when treated with Barbell (*red*) or co-treatments of D07 and DRPB (*split*, not connected with GS linker).

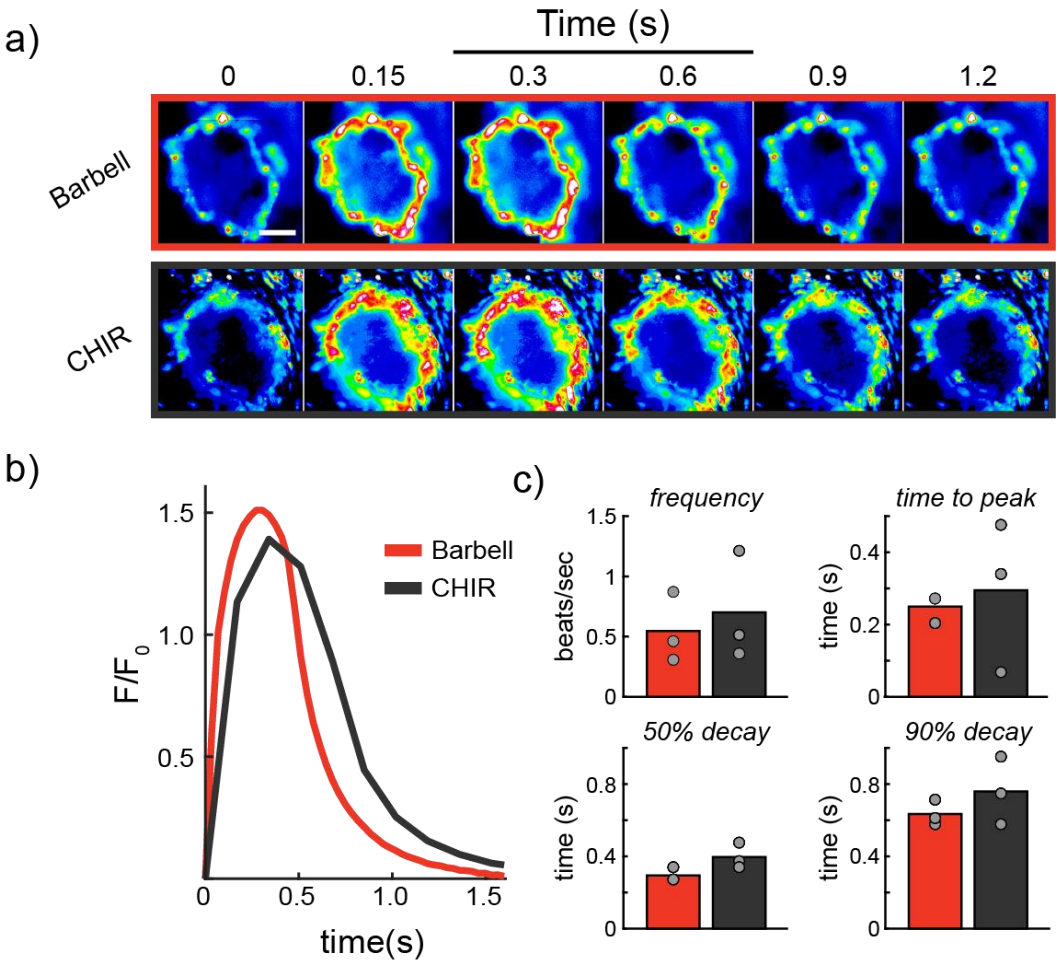

Figure S4.3 a) Representative images of calcium flux during a single beat. Scale bar = 100 µm. b) Zoomed-in representation (1.5 seconds) of a single pulse shown in **Figure 4.4 d**. c) Quantification of frequency, time to peak, 50% decay, and 90% decay for Barbell- and CHIR-derived CM patterns. n=3 for each condition.

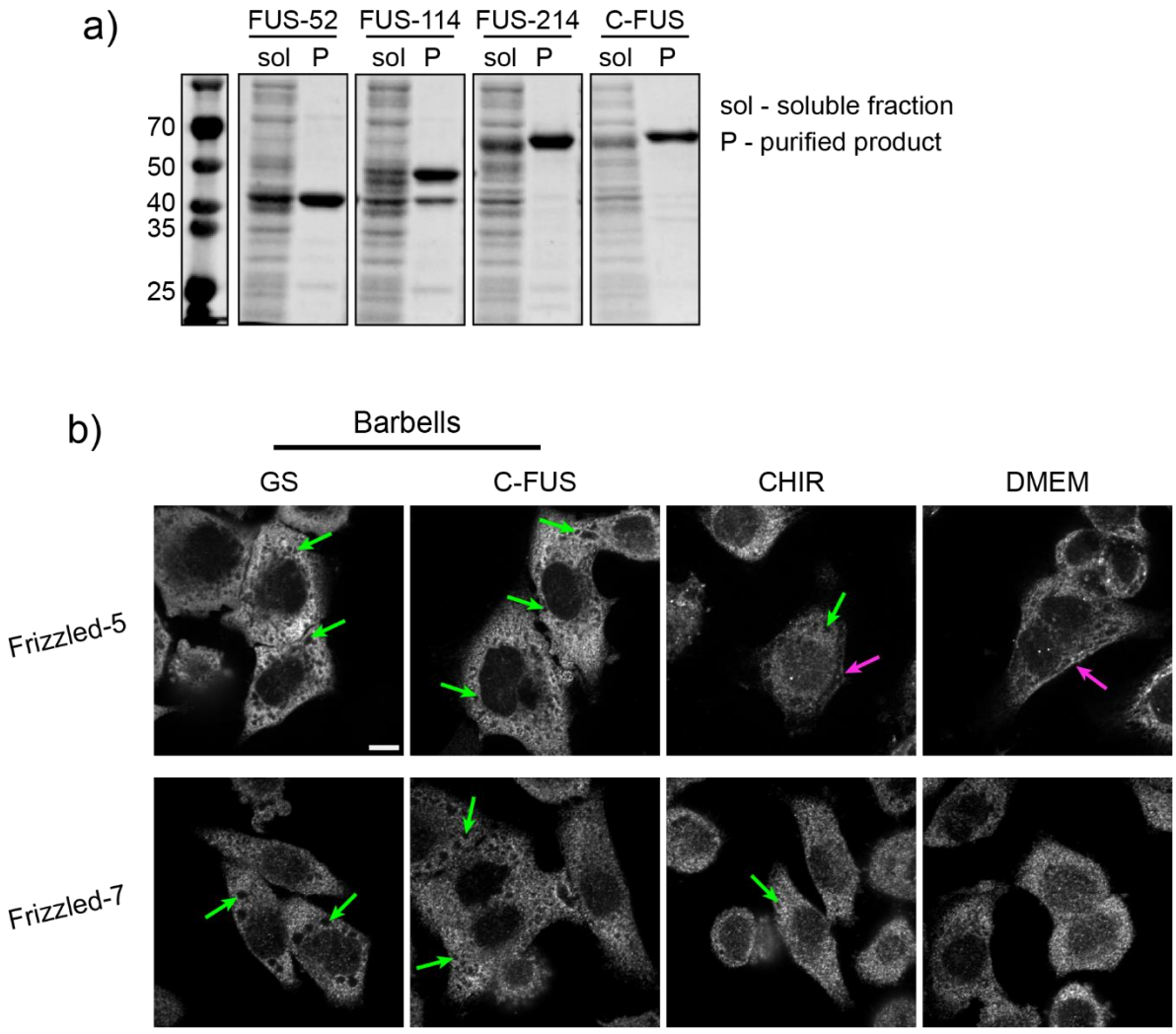

Figure S4.4 a) SDS-PAGE of FUS Barbell purifications. b) Immunofluorescence of Frizzled-5 (*top*) and Frizzled-7 (*bottom*) following 15 minutes of treatment. Green arrows represent endosome-like structures. Pink arrows represent membrane localization. Scale bar = 10 μm.

Table S4.1 – Amino Acid Sequences

Red – DRPB-7/8

Cyan – D07 nanobody

Magenta – FUS

Green – LOV domain

Construct	*Amino Acid Sequence*
Wnt Barbell	MSELGTRLIRAALDGNKDRVKDLIENGADVNASLMSGATPLHAAAMNGHKEVVKLLISKGADVNAQSVAGSTPLDAAAFSGHKEVVKLLISKGADVNAVNAAGLTPLHAAADNGHKEVVKLLISKGADVNAKADHGMTPLHFAAQRGHKEVVKLLISKGADLNTSAKDGATPLDMARESGNEEVVKLLEKQLEGSGSGGSGSGAEVQLQESGGGLVQAGGSLRLSCAASGRTFSIYTIGWFRQAPGKEREFVAEITWSGGSTYYADSVKGRFTISRDNAKNTVYLQMNSLKPEDTAVYYCAAITYTRGIYKYWGQGTQVTVSSGGSGGHHHHHH
DRPB	MGSSELGTRLIRAALDGNKDRVKDLIENGADVNASLMSGATPLHAAAMNGHKEVVKLLISKGADVNAQSVAGSTPLDAAAFSGHKEVVKLLISKGADVNAVNAAGLTPLHAAADNGHKEVVKLLISKGADVNAKADHGMTPLHFAAQRGHKEVVKLLISKGADLNTSAKDGATPLDMARESGNEEVVKLLEKQLEGGSGGHHHHHH
D07	AEVQLQESGGGLVQAGGSLRLSCAASGRTFSIYTIGWFRQAPGKEREFVAEITWSGGSTYYADSVKGRFTISRDNAKNTVYLQMNSLKPEDTAVYYCAAITYTRGIYKYWGQGTQVTVSSGGSGGHHHHHH
FUS_52 Barbell	MSELGTRLIRAALDGNKDRVKDLIENGADVNASLMSGATPLHAAAMNGHKEVVKLLISKGADVNAQSVAGSTPLDAAAFSGHKEVVKLLISKGADVNAVNAAGLTPLHAAADNGHKEVVKLLISKGADVNAKADHGMTPLHFAAQRGHKEVVKLLISKGADLNTSAKDGATPLDMARESGNEEVVKLLEKQLEASNDYTQQATQSYGAYPTQPGQGYSQQSSQPYGQQSYSGYSQSTDTSGYGQAEVQLQESGGGLVQAGGSLRLSCAASGRTFSIYTIGWFRQAPGKEREFVAEITW

	SGGSTYYADSVKGRFTISRDNAKNTVYLQMNSLKPEDTAVYYCAAITYTRG IYKYWGQGTQVTVSSGGSGGHHHHHH
FUS_114 Barbell	MSELGTRLIRAALDGNKDRVKDLIENGADVNASLMSGATPLHAAAMN GHKEVVKLLISKGADVNAQSVAGSTPLDAAAFSGHKEVVKLLISKGADVN AVNAAGLTPLHAAADNGHKEVVKLLISKGADVNAKADHGMTPLHFAAQR GHKEVVKLLISKGADLNTSAKDGATPLDMARESGNEEVVKLLEKQLEASN DYTQQATQSYGAYPTQPGQGYSQQSSQPYGQQSYSGYSQSTDTSGYGQSSY SSYGQSQNTGYGTQSTPQGYGSTGGYGSSQSSQSSYGQQSSYPGYGQQPAP SSTSGSYGAEVQLQESGGGLVQAGGSLRLSCAASGRTFSIYTIGWFRQAPGK EREFVAEITWSGGSTYYADSVKGRFTISRDNAKNTVYLQMNSLKPEDTAVY YCAAITYTRGIYKYWGQGTQVTVSSGGSGGHHHHHH
FUS_214 Barbell	MSELGTRLIRAALDGNKDRVKDLIENGADVNASLMSGATPLHAAAMN GHKEVVKLLISKGADVNAQSVAGSTPLDAAAFSGHKEVVKLLISKGADVN AVNAAGLTPLHAAADNGHKEVVKLLISKGADVNAKADHGMTPLHFAAQR GHKEVVKLLISKGADLNTSAKDGATPLDMARESGNEEVVKLLEKQLEASN DYTQQATQSYGAYPTQPGQGYSQQSSQPYGQQSYSGYSQSTDTSGYGQSSY SSYGQSQNTGYGTQSTPQGYGSTGGYGSSQSSQSSYGQQSSYPGYGQQPAP SSTSGSYGSSSQSSSYGQPQSGSYSQQPSYGGQQQSYGQQQSYNPPQGYGQ QNQYNSSSGGGGGGGGGNYGQDQSSMSSGGGSGGGYGNQDQSGGGGSG GYGQQDRGAEVQLQESGGGLVQAGGSLRLSCAASGRTFSIYTIGWFRQAPG KEREFVAEITWSGGSTYYADSVKGRFTISRDNAKNTVYLQMNSLKPEDTAV YYCAAITYTRGIYKYWGQGTQVTVSSGGSGGHHHHHH
C-FUS Barbell	MSELGTRLIRAALDGNKDRVKDLIENGADVNASLMSGATPLHAAAMN GHKEVVKLLISKGADVNAQSVAGSTPLDAAAFSGHKEVVKLLISKGADVN AVNAAGLTPLHAAADNGHKEVVKLLISKGADVNAKADHGMTPLHFAAQR GHKEVVKLLISKGADLNTSAKDGATPLDMARESGNEEVVKLLEKQLEGSGS GGSGSGAEVQLQESGGGLVQAGGSLRLSCAASGRTFSIYTIGWFRQAPGKE REFVAEITWSGGSTYYADSVKGRFTISRDNAKNTVYLQMNSLKPEDTAVYY

	CAAITYTRGIYKYWGQGTQVTVSSMASNDYTQQATQSYGAYPTQPGQGYS QQSSQPYGQQSYSGYSQSTDTSGYGQSSYSSYGQSQNTGYGTQSTPQGYGS TGGYGSSQSSQSSYGQQSSYPGYGQQPAPSSTSGSYGSSSQSSSYGQPQSGS YSQQPSYGGQQQSYGQQQSYNPPQGYGQQNQYNSSSGGGGGGGGGGNYG QDQSSMSSGGGSGGGYGNQDQSGGGGSGGYGQQDRGGGSGGHHHHHH
G16 LOV Barbell	MSELGTRLIRAALDGNKDRVKDLIENGADVNASLMSGATPLHAAAMN GHKEVVKLLISKGADVNAQSVAGSTPLDAAAFSGHKEVVKLLISKGADVN AVNAAGLTPLHAAADNGHKEVVKLLISKGADVNAKADHGMTPLHFAAQR GHKEVVKLLISKGADLNTSAKDGATPLDMARESGNEEVVKLLEKQLEGSGS GGSGSGAEVQLQESGGGLVQAGLERIEKNFVITDPRLPDNPIIFASDSFLQLT EYSREEILGRNCRFLQGPETDRATVRKIRDAIDNQTEVTVQLINYTKSGKKF WNLFHLQPMRDQKGDVQYFIGVQLDGTEHVRDAAEREGVMLIKKTAENID EAAGSLRLSCAASGRTFSIYTIGWFRQAPGKEREFVAEITWSGGSTYYADSV KGRFTISRDNAKNTVYLQMNSLKPEDTAVYYCAAITYTRGIYKYWGQGTQ VTVSSGGSGGHHHHHH
V65 LOV Barbell	MSELGTRLIRAALDGNKDRVKDLIENGADVNASLMSGATPLHAAAMN GHKEVVKLLISKGADVNAQSVAGSTPLDAAAFSGHKEVVKLLISKGADVN AVNAAGLTPLHAAADNGHKEVVKLLISKGADVNAKADHGMTPLHFAAQR GHKEVVKLLISKGADLNTSAKDGATPLDMARESGNEEVVKLLEKQLEGSGS GGSGSGAEVQLQESGGGLVQAGGSLRLSCAASGRTFSIYTIGWFRQAPGKE REFVAEITWSGGSTYYADSVLERIEKNFVITDPRLPDNPIIFASDSFLQLTEYS REEILGRNCRFLQGPETDRATVRKIRDAIDNQTEVTVQLINYTKSGKKFWNL FHLQPMRDQKGDVQYFIGVQLDGTEHVRDAAEREGVMLIKKTAENIDEAA KGRFTISRDNAKNTVYLQMNSLKPEDTAVYYCAAITYTRGIYKYWGQGTQ VTVSSGGSGGHHHHHH
A76 LOV Barbell	MSELGTRLIRAALDGNKDRVKDLIENGADVNASLMSGATPLHAAAMN GHKEVVKLLISKGADVNAQSVAGSTPLDAAAFSGHKEVVKLLISKGADVN AVNAAGLTPLHAAADNGHKEVVKLLISKGADVNAKADHGMTPLHFAAQR

	GHKEVVKLLISKGADLNTSAKDGATPLDMARESGNEEVVKLLEKQLEGSGS GGSGSGAEVQLQESGGGLVQAGGSLRLSCAASGRTFSIYTIGWFRQAPGKE REFVAEITWSGGSTYYADSVKGRFTISRDLERIEKNFVITDPRLPDNPIIFASD SFLQLTEYSREEILGRNCRFLQGPETDRATVRKIRDAIDNQTEVTVQLINYTK SGKKFWNLFHLQPMRDQKGDVQYFIGVQLDGTEHVRDAAEREGVMLIKKT AENIDEAAKNTVYLQMNSLKPEDTAVYYCAAITYTRGIYKYWGQGTQVTV SSGGSGGHHHHHH

Table S4.2 – qPCR primers

Gene		***Sequence (5'-> 3')***
TBXT(T)	*F*	GTGTCCCAGACGTTCTCAGTC
	R	GGGAGACGCATAGCCTTGT
EOMES	*F*	GTGCCCACGTCTACCTGTG
	R	CCTGCCCTGTTTCGTAATGAT
SNAI2	*F*	CGAACTGGACACACATACAGTG
	R	CTGAGGATCTCTGGTTGTGGT
SNAI1	*F*	TCGGAAGCCTAACTACAGCGA
	R	AGATGAGCATTGGCAGCGAG
GSC	*F*	AACGCGGAGAAGTGGAACAAG
	R	CTGTCCGAGTCCAAATCGC
HAND1	*F*	GAGAGCATTAACAGCGCATTCG
	R	CGCAGAGTCTTGATCTTGGAGAG
MIXL1	*F*	GGCGTCAGAGTGGGAAATCC
	R	GGCAGGCAGTTCACATCTACC
OCT4	*F*	GGGAGATTGATAACTGGTGTGTT
	R	GTGTATATCCCAGGGTGATCCTC
SOX2	*F*	TACAGCATGTCCTACTCGCAG
	R	GAGGAAGAGGTAACCACAGGG
NANOG	*F*	CCCCAGCCTTTACTCTTCCTA
	R	CCAGGTTGAATTGTTCCAGGTC
Nkx2.5	*F*	GTCTCCTCTGACTCCAACAGCG
	R	ACCACCCTGTTGCTGTAGCCAA
SERCA	*F*	GGACTTTGAAGGCGTGGATTGTG
	R	CTCAGCAAGGACTGGTTTTCGG
cTNT	*F*	AAGAGGCAGACTGAGCGGGAAA
	R	AGATGCTCTGCCACAGCTCCTT
MyH6	*F*	GGAAGACAAGGTCAACAGCCTG
	R	TCCAGTTTCCGCTTTGCTCGCT

MyH7	*F*	GGAGTTCACACGCCTCAAAGAG
	R	TCCTCAGCATCTGCCAGGTTGT
MyL2	*F*	TACGTTCGGGAAATGCTGAC
	R	TTCTCCGTGGGTGATGATG
RUNX2	*F*	GACCAGTCTTACCCCTCCTAC
	R	CTGCCTGGCTCTTCTTACTGA
ALP	*F*	ACTCCCACTTCATCTGGAAC
	R	CCTGTTCAGCTCGTACTGCA
Col1a1	*F*	GAGAGGAAGGAAAGCGAGGAG
	R	GGGACCAGCAACACCATCT
Osteocalcin	*F*	TGACGAGTTGGCTGACCA
	R	AGGGTGCCTGGAGAGGAG
GAPDH	*F*	GTCTCCTCTGACTTCAACAGCG
	R	ACCACCCTGTTGCTGTAGCCAA

CHAPTER 5: Concluding Remarks

The work presented in this dissertation underscores a paradigm shift in molecular tool development, placing an emphasis on strategies that operate externally to transmit cellular signals that can be precisely controlled in both space and time. The developments focused on establishing innovative, yet approachable, methods to shape the extracellular space as a way to control cellular fates.

Synthetic molecular systems that enable temporal or spatial control over cellular processes have been pivotal in understanding the importance of dynamic cues in shaping fates at both the cellular- and tissue- levels. These approaches, however, typically require complex chemistries or genetic perturbations, which often present significant limitations and challenges to their widespread utilization. Moreover, intracellularly facing approaches, like small-molecules and genetic modifications, suffer from off-target effects, interfere with or bypass natural cellular processes, or require intricate delivery systems, all of which ultimately restrict their utility in certain contexts. By circumventing these issues and initiating cues extracellularly, the strategies discussed herein offer an elegant solution to the inherent limitations.

Chapter 2 covers a novel approach for enabling dynamic mechanical changes in natural hydrogels. Previous mechanical studies were either limited to unidirectional mechanical changes or accomplished using networks of synthetic polymers that require thorough modification to support cell growth. This work is the first reported instance of a hydrogel derived from native ECM components undergoing reversible mechanical changes. Chapter 3 continues to elaborate on ECM hydrogel engineering as a way to shape extracellular signals by using a photo-caged molecule to enable patterning of small molecules and morphogens on

several ECM-derived networks. The resulting functionalized surfaces offer arbitrary spatial control over cellular phenotypes. Finally, Chapter 4 addresses limitations in Wnt ligand biomanufacturing by covering the creation of a bacterially expressed synthetic Wnt (Wnt Barbell). The Wnt Barbell serves as a general Wnt agonist, aides in tissue-specific differentiations, and can be further engineered to tailor receptor valency and activate Wnt signaling in a light-dependent fashion.

In summary, the development and utilization of extracellular tools represents a cornerstone in the ever-evolving space of molecular technologies. Their non-invasive nature, coupled with their ability to precisely modulate cellular processes, holds immense promise for shaping the future of precision medicines and scientific advancement.